

UNCLASSIFIED

AD NUMBER

AD907560

NEW LIMITATION CHANGE

TO

**Approved for public release, distribution
unlimited**

FROM

**Distribution authorized to U.S. Gov't.
agencies only; Test and Evaluation; OCT
1972. Other requests shall be referred to
Rome Air Development Center, Griffiss AFB,
NY.**

AUTHORITY

RADC USAF ltr, 3 Mar 1979

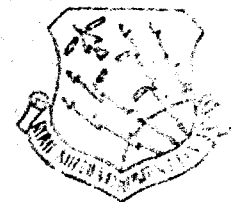
THIS PAGE IS UNCLASSIFIED

THIS REPORT HAS BEEN DELIMITED
AND CLEARED FOR PUBLIC RELEASE
UNDER DOD DIRECTIVE 5200.20 AND
NO RESTRICTIONS ARE IMPOSED UPON
ITS USE AND DISCLOSURE.

DISTRIBUTION STATEMENT A

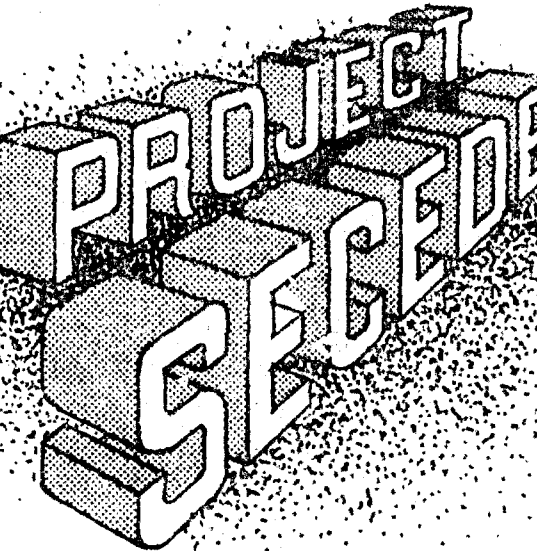
APPROVED FOR PUBLIC RELEASE;
DISTRIBUTION UNLIMITED.

RADC-TR-72-336, Volume I
Final Technical Report
October 1972



Prepared By
Rome Air Development Center
Air Force Systems Command
Griffiss Air Force Base, New York 13440

AD907560



ANALYSIS OF BARIUM CLOUDS

AVCO Everett Research Laboratory

Sponsored by
Defense Advanced Research Projects Agency
ARPA Order No. 1057

Distribution limited to U.S. Gov't agencies only;
test and evaluation; January 1973. Other requests
for this document must be referred to RADC (OCSE),
GAFB, NY 13441.

The views and conclusions contained in this document are those
of the authors and should not be interpreted as necessarily
representing the official policies, either expressed or implied,
of the Defense Advanced Research Projects Agency or the U. S.
Government.



ANALYSIS OF BARIUM CLOUDS

Dr. B. Kivel
Dr. L. M. Linson
Dr. G. M. Weyl

Contractor: AVCO Everett Research Laboratory
Contract Number: F30602-71-C-0067
Effective Date of Contract: 8 May 1970
Contract Expiration Date: 31 October 1972
Amount of Contract: \$358,000.00
Program Code Number: 1E20

Principal Investigators: Dr. Bennett Kivel
Phone: 617 389-3000, Ext. 417

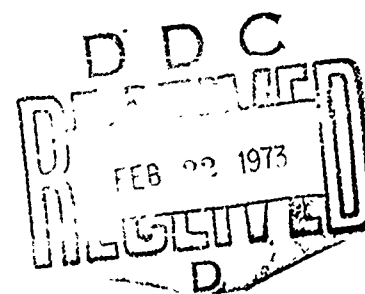
Dr. Lewis Linson
Phone: 617 389-3000, Ext. 612

Project Engineer: Vincent Coyne
Phone: 315 330-3107

Contract Engineer: Leonard Strauss
Phone: 315 330-3451

Distribution limited to U.S. Gov't agencies only;
test and evaluation; January 1973. Other requests
for this document must be referred to RADC (OCSE),
GAFB, NY 13441.

This research was supported by the
Defense Advanced Research Projects
Agency of the Department of Defense
and was monitored by Leonard Strauss,
RADC (OCSE), GAFB, NY 13441 under
Contract F30602-71-C-0067.

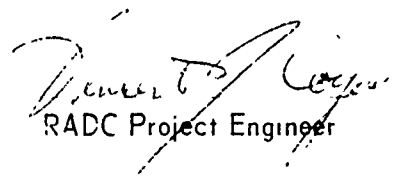


FOREWORD

This report is a Final Technical Report and is issued in two volumes. Volume I, which is unclassified, contains Chapters 1 through 5 prepared principally by L. M. Linson, B. Kivel, S. Powers, and L. F. Cianciolo. Volume II contains Chapters 1 and 2 prepared principally by G. M. Weyl and L. M. Linson and is classified.

PUBLICATION REVIEW

This technical report has been reviewed and is approved



Donald T. Kivel
RADC Project Engineer



Leonard Strauss
RADC Contract Engineer

ABSTRACT

Several aspects of the analysis of barium ion clouds are presented including ion cloud modeling, comparison of radar and optical data, and correlation of data with theory. A quantitative model has been developed from which various properties of barium ion clouds, primarily their size, time history of the peak electron concentration, and height-integrated conductivity can be estimated. These estimates are in excellent agreement with the observations of Secede ion clouds. The modeling of the radiation transport in the ion cloud has been confirmed by a Monte Carlo calculation. The optical analysis of Spruce at R + 14 min has been corrected for effects of cloud geometry and the results for ion density are found self-consistent and in agreement with radar measurements. A summary review is given of the values and limitations of photographic data. The current status of theoretical understanding of the dynamics of barium ion clouds is reviewed. Particular attention is given to their motion, deformation, and the properties of striations including onset time, scale size, and dissipation.

TABLE OF CONTENTS

<u>Chapter</u>		<u>Page</u>
VOLUME I		
1	QUANTITATIVE ION CLOUD MODELING	1
2	PARTIAL REDISTRIBUTION IN RADIATION TRANSPORT	41
3	SPRUCE CORRELATION	71
4	USE OF PHOTOGRAPHIC DATA FOR ESTIMATING ION DENSITY AND INVENTORY	93
5	THEORY OF ION CLOUD DYNAMICS AND MORPHOLOGY	109

PRECEDING PAGE BLANK NOT FILMED

LIST OF ILLUSTRATIONS

<u>Figure</u>		<u>Page</u>
CHAPTER 1		
1	The Neutral Diffusion Coefficient, the Parallel Ambipolar Diffusion Coefficient, and the Barium Neutral Collision Time as a Function of Altitude	4
2	The Ionization Time Constant as a Function of Altitude	6
3	The Equal Mass Radius as a Function of Altitude and Payload Under the Assumption that the Vapor Mass is Equal to 0.2 P	10
4	The Scale Size of the Ion Cloud Transverse to the Magnetic Field as a Function of Altitude and Payload as Given by Eq. (11)	12
5	The Upper Limit to the Peak Electron Density in the Ion Cloud as a Function of Altitude and Payload as Given by Eq. (13)	14
6	The Electron Content on a Magnetic Field Line as a Function of Altitude and Payload as Given by Eq. (14)	15
7	The Peak Electron Density at One Minute after Release as a Function of Altitude and Payload	17
8	The Time at Which Ambipolar Diffusion Parallel to the Magnetic Field Begins to Cause a Decrease as $t^{-1/2}$ in the Peak Electron Density of the Ion Cloud	18
9	The Gaussian Length Along the Magnetic Field for a Barium Ion Cloud in Diffusive Equilibrium	20
10	The Asymptotic Value of the Peak Electron Density as a Function of Altitude and Payload	21
11	The Time at Which the Peak Electron Density of the Barium Ion Cloud Ceases Decreasing as $t^{-1/2}$ as a Function of Altitude and Payload	22
12	The Time History of the Peak Electron Density for 48-kg Releases at Three Different Altitudes	25

<u>Figure</u>		<u>Page</u>
13	The Time History of the Peak Electron Density for Several Different Payloads at an Altitude of Around 190 to 200 km	26
14	The Height-Integrated Pedersen Conductivity for a Barium Ion Cloud as a Function of Altitude and Payload	32
CHAPTER 2		
1	Diffusion Solution in a Slab of Optical Depth $\tau = 2.3$	46
2	Spectral Line Profile as seen from the Illuminated Face (front) and the Opposite (back) for a Slab of Scatterers with a Gaussian Profile and an Optical Depth of 100 at the Line Center	49
3	Coefficients of Reflection and Transmission as a function of the Normalized Incident Energy	57
4	Coefficients of Diffuse Reflection and Transmission and Unscattered Transmission for a Slab as a function of the Optical Depth at the Line Center	59
5	The Reflected Spectrum for a Uniform Incident Spectrum as a function of the Final Energy of the Reflected Photons	63
6	The Angular Distribution of Reflected Light which is Incident Normal to the Face of the Slab with Optical Depth 100	65
CHAPTER 3		
1	Photograph from Tyndall of Spruce at R + 13.25 min	77
2	Photograph from C-6 Site of Spruce at R + 13.25 min	78
3	Ground Plot Locating Spruce at R + 13.25 min	80
4	Correlation of Cloud Intensity vs Ion Column Density Comparing Spectral and Slab Models	86
5	Data Correl. ion of Spruce at R + 14 min Giving Ion Column Density near Trailing Edge as a function of Relative Distance along the Earth's Magnetic Field	87
CHAPTER 4		
1	Correlation of Photographic Data from SECEDE I	102
2	Relation between Intensity and Ion Column Density	103

<u>Figure</u>		<u>Page</u>
3	Correlation of Data Obtained on Spruce at 14 min after Release	105
CHAPTER 5		
1	Event Titmouse at Three Stages of Development	111
2	Simultaneous Photographs of Event Spruce at R + 19 min Seen from Site C-6 on the Left and from Tyndall on the Right (Technology International Corporation)	115
3	Plasma Cloud-Ionosphere Model	118
4	Comparison of the Olive and Spruce Ion Cloud Thicknesses in the Direction of the Magnetic Field as Obtained by the Thomson Scatter Radar Shown by the Open Circles and the Solid Theoretical Curves Based on Ambipolar Diffusion Parallel to the Magnetic Field	128
5	Diffusive Equilibrium Electron-Concentration Distributions Along the Earth's Magnetic Field	130
6	Simple Two-Dimensional Model	132
7	The HELE-SHAW Cell (Physical Dynamics, Inc.)	135
8	Changes in the Ionospheric Current Flow Due to the Presence of a Highly Conducting Barium Ion Cloud, a) Height-Integrated Current Density Flowing Perpendicular to the Magnetic Field; This Same Pattern Results in the Cases of b) a One-Layered Ionosphere, c) a Two-Layered Ionosphere, and d) Local Plus Conjugate Ionosphere	139
9	Effect of Polarization Field Induced by the Ion Cloud	141
10	Coupling Neglecting the Influence of the Conjugate Ionosphere	144
11	Coupling Including the Influence of the Conjugate Ionosphere	147
12	Sketch of Magnetospheric Current Flows which Couple the Conjugate Ionosphere and the Barium Cloud	150
13	Deformations of Contours Resulting from Power Series Expansion of the Streamlines in Time, a) Zeroth Order Term; b) Zeroth Order Plus First Order Term	152
14	Deformations of Isodensity Contours for an Initially Circular Plasma Cloud with No Initial Perturbations (Bell Telephone Laboratories)	153

<u>Figure</u>		<u>Page</u>
15	Steepening Time According to Two Different Models; a) Broad Density Profile; b) Constant Density within a Cylinder	155
16	Narrowing of an Elongated Ion Cloud	157
17	Elongated Olive Cloud Stretched into a Thin Sheet (Technology International Corporation)	158
18	The Spruce Ion Cloud Showing Elongation in the Direction of the Neutral Wind and Narrowing in the Middle (Technology International Corporation)	160
19	Morphology of Nonlinear Striations Deduced from Photographs, Simulations, and Theory	162
20	Onset Time as a Function of U_0^{-1}	165
21	Onset Time (Normalized to $U_0 = 75$ m/s) Dependence on Altitude at Constant Payload	166
22	Normalized Onset Time as a Function of Cloud to Background Height-Integrated Pedersen Conductivity	168
23	Redwood Striations Viewed Directly up the Magnetic Field Line (Technology International Corporation)	170
24	Spruce Striations Viewed Directly up the Magnetic Field Line (Technology International Corporation)	171
25	Nutmeg Looking Directly up the Magnetic Field Line (Technology International Corporation)	172
26	Striation Development in the HELE-SHAW Cell (Physical Dynamics, Incorporated)	174
27	Bifurcation for a Typical Sheet (Physical Dynamics, Inc.)	175
28	Pinch-Off and Formation of Isolated Rods (Physical Dynamics, Inc.)	176
29	Deformation of Isodensity Contours for an Initially Circular Plasma Cloud with a 5% Initial Perturbation Showing a Simulation of Bifurcation (Bell Telephone Laboratories)	178
30	Spruce from C-6 at R + 22:25 (Technology International Corp.)	179
31	Spruce from C-6 at R + 22:59 (Technology International Corp.)	180

<u>Figure</u>		<u>Page</u>
32	Spruce from C-6 at R + 24:05 (Technology International Corp.)	181
33	Spruce from C-6 at R + 26:22 (Technology International Corp.)	182
34	Spruce from C-6 at R + 27:08 (Technology International Corp.)	183
35	Linear Wave Spectrum	186
36	Schematic of a Dissipation Mechanism for Rods	190
37	Rod and Sheet Lifetime	192

TECHNICAL SUMMARY

VOLUME I

Chapter 1 describes a quantitative model from which the properties of ion clouds can be estimated. Of particular importance are the ion cloud size perpendicular to the magnetic field, the peak electron content on magnetic field lines, the time history of the peak electron concentration, and the height-integrated Pedersen conductivity of the ion cloud. These properties are given as a function of the altitude of release (140 km to 300 km) and chemical payload weight in the range 0.1 kg to 400 kg and are found to be in excellent agreement with observations of Secede ion clouds. The effects of the neutral wind, the ambient electric field, the ionospheric conductivity, the latitude of release, and the time of day and year are also discussed. The results of this modeling are useful for future test planning.

Chapter 2 reports on a radiation transport study that confirms the optical modeling used in Chapter 3. Radiation diffusion in a slab of purely scattering atoms with only one transition is calculated using a Monte Carlo method. Partial redistribution because of the Doppler effect is included. The scattering is assumed to be isotropic and incoherent. Results are obtained for 1) the amount of diffuse reflection and transmission as a function of optical depth, and 2) the angular distribution and spectrum of the reflected component. The results are found to be similar to that

obtained from a differential equation for radiation diffusion without redistribution. The light reflected is characterized by an albedo close to one at the line center when the optical depth is large compared to one. The reflected intensity increases with the amount of scattering material corresponding to an increase in an effective line width. The total amount of diffusely transmitted radiation is insensitive to the amount of scattering material and has two spectral bands centered in the line wings where the optical depth is about two. The angular distribution of reflected radiation is Lambertian.

Chapter 3 contains a correlation of Spruce data. Optical analysis for event Spruce at R + 14 min has been improved to take account of the angles between the cloud face and the solar illumination direction and the lines of sight from Tyndall and Barin. The correction for the dependence of these angles leads to consistent ion densities and better agreement with the radar determined density. The peak ion column density perpendicular to the cloud face is determined to be $\sim 3 \times 10^{12} \text{ cm}^{-2}$. Comparison of the extent of the ion cloud as observed by the Thomson scatter radar measurement with the longer extent observed optically leads to an estimate of cloud width of about 2 km at a distance of about 5 km west of the trailing edge.

Chapter 4 reviews the use of photographic data for estimating ion density and ion inventory. Methods for analysis of optically thin and thick clouds are considered. An effective line width method is preferred for thick clouds in order not to underestimate ion column density by using the linear relation valid for optically thin clouds. In either case a semi-empirical theory is required because of the many unknowns. The unknowns are grouped as problems of 1) data reduction and 2) interpretation of

reduced data. Data reduction problems, which include film reciprocity, dependence of sensitivity on film temperature, and atmospheric transmission may be alleviated using known star intensities as standards.

Unknowns in interpretation include the solar spectral flux and radiation transport details. The good results of the data correlation in Spruce at $R + 14$ min lead to the conclusion that despite unknowns a semi-empirical analysis of photographic data can be used to measure barium cloud ion column density.

Chapter 5 consists of a review of our current understanding of barium ion cloud dynamics. It is found that the most important parameter that determines the behavior of ion clouds is the ratio of the height-integrated Pedersen conductivity of the ion cloud to that of the ambient ionosphere. A theoretical treatment of the motion of ion clouds shows that low conductivity clouds tend to move with the local $\vec{E} \times \vec{B}/B^2$ velocity while high conductivity clouds tend to move with the local neutral wind. Quantitative agreement between theory and observations is achieved by assuming that the conjugate ionosphere in the southern hemisphere is contributing to the ambient conductivity. A simple model is shown to explain several aspects of the deformations of ion clouds including their steepening on the backside, elongation in the direction of motion, and narrowing transverse to the direction of motion. The properties of striations including their onset time, scale size, and dissipation are treated. It is found that the normalized onset time is a minimum for clouds of intermediate conductivity. The simple two-dimensional model predicts the scale size of striations when the effects of the cloud polarization field, conductivity, and finite size are included as well as electron collisions. The dissipation of striations is controlled by a combination of diffusion and convection. Areas where more theoretical work is needed are also discussed.

CHAPTER 1
QUANTITATIVE ION CLOUD MODELING

1. QUANTITATIVE ION CLOUD MODELING

Lewis M. Linson

A. INTRODUCTION

We will present quantitatively the variation of ion-cloud properties such as size and density, as a function of the altitude of release (from 140 to 300 km), and payload in the range from 0.1 kg to 400 kg. Knowledge of these cloud properties over this range of parameters will be useful for future test planning and is necessary as an input for theoretical work that describes the dynamics and distortions of barium ion clouds. The plasma aspects of barium ion cloud behavior are described in Chapter 5. The model described below has been chosen to give optimum agreement with the best available optical and radar data. A correlation of the results of this modeling with the data obtained during the Secede I and II test series conducted at mid-latitudes will be discussed.

In the following three sections we will describe the ion cloud properties at early, intermediate, and late-times after release. Early-time behavior refers to less than a minute after release. Intermediate-time behavior, which is dominated by ambipolar diffusion parallel to the magnetic field, typically will last from one to 15 minutes after release. Long-time behavior typically occurs after some tens of minutes. In Section E we will also discuss the time variation of the electron density as obtained from the above modeling for several typical ion clouds. In Section F we compare the results of the modeling with optical and radar data. The height-integrated Pedersen conductivity of the ion cloud will also be presented as a function of altitude and payload. In Section G we will describe

the influence of several ambient parameters whose variation has not been included in the modeling. In particular, the effects of the neutral wind, the ambient electric field, the ionospheric conductivity, the latitude of the release, and the time of day and year will be discussed. We will also indicate the importance of the results of this modeling for determining the behavior of ion clouds as they are influenced by the ambient electric field. The limitations of the modeling will also be discussed.

B. EARLY-TIME BEHAVIOR

By the early-time behavior of the ion cloud we mean the time during which the ion cloud is formed by the photoionization of barium atoms. The deposition of barium ions from the barium vapor typically takes place in less than a minute. The single most important parameter that describes the early-time behavior is the collision time, τ , of barium with the ambient atmospheric constituents. The mobility, μ , of barium ions in nitrogen gas has been measured,¹ from which we may obtain the barium ion-nitrogen collision time,

$$\tau = \frac{m_{Ba}}{e} \mu = \frac{8.6 \times 10^9}{\bar{N}_n} \text{ seconds} \quad (1)$$

where m_{Ba} is the atomic mass of barium and e is the magnitude of the electron charge. The collision cross section has been assumed to vary inversely as the square root of the temperature, and \bar{N}_n is a weighted atmospheric concentration in cm^{-3} ,

$$\bar{N}_n = N_{N_2} + N_{O_2} + 0.8 N_O. \quad (2)$$

It has been assumed that the collision cross section for oxygen molecules and atoms is the same as it is for nitrogen molecules. The fact that the

lighter oxygen atoms are less efficient in stopping a heavier barium ion is expressed by the appropriate Langevin factor, $(1 + m_{Ba} m_{N_2})^{1/2} \times (1 + m_{Ba} m_O)^{-1/2} \sim 0.8$, where m_{N_2} and m_O are the masses of the nitrogen molecule and oxygen atom respectively. We also assume that barium atoms have the same collision cross section with air and hence τ given by Eq. (1) will represent the barium atom-neutral air collision time.

The CIRA 1965 atmospheric model 6 at 1800 hours has been used to obtain the neutral temperature, mass density, and N_2 , O_2 , and O densities as a function of altitude. The model 6 is appropriate for the solar flux conditions that existed during the second half of January 1971. We have assumed that the ion temperature, T_i , is the same as the neutral temperature, T_n , since the ions and neutrals are in close thermal contact. Our model for the altitude dependence of the electron-to-ion temperature ratio was influenced by the recent paper by Wand². We have taken the electron-to-ion temperature ratio, T_e/T_i , as varying linearly from one at 130 km to a value of 1.6 at 210 km and then decreasing linearly to 1.2 at 300 km. The barium-neutral and barium-ion ambipolar diffusion coefficients, D_n and D_{11} , respectively, are given by

$$D_n = \frac{k T_n}{m_{Ba}} \tau; D_{11} = D_n \left(1 + \frac{T_e}{T_n} \right) \quad (3)$$

and are shown in Fig. 1 along with the ion-neutral collision time, τ , as a function of altitude. k is Boltzmann's constant.

We also need to know the rate at which barium atoms are photoionized and oxidized by the ambient air. Haerendel of the Max-Planck Institute has consistently reported photoionization times of order 19 seconds while Best of AFCRL reports a time closer to 30 seconds. In our model

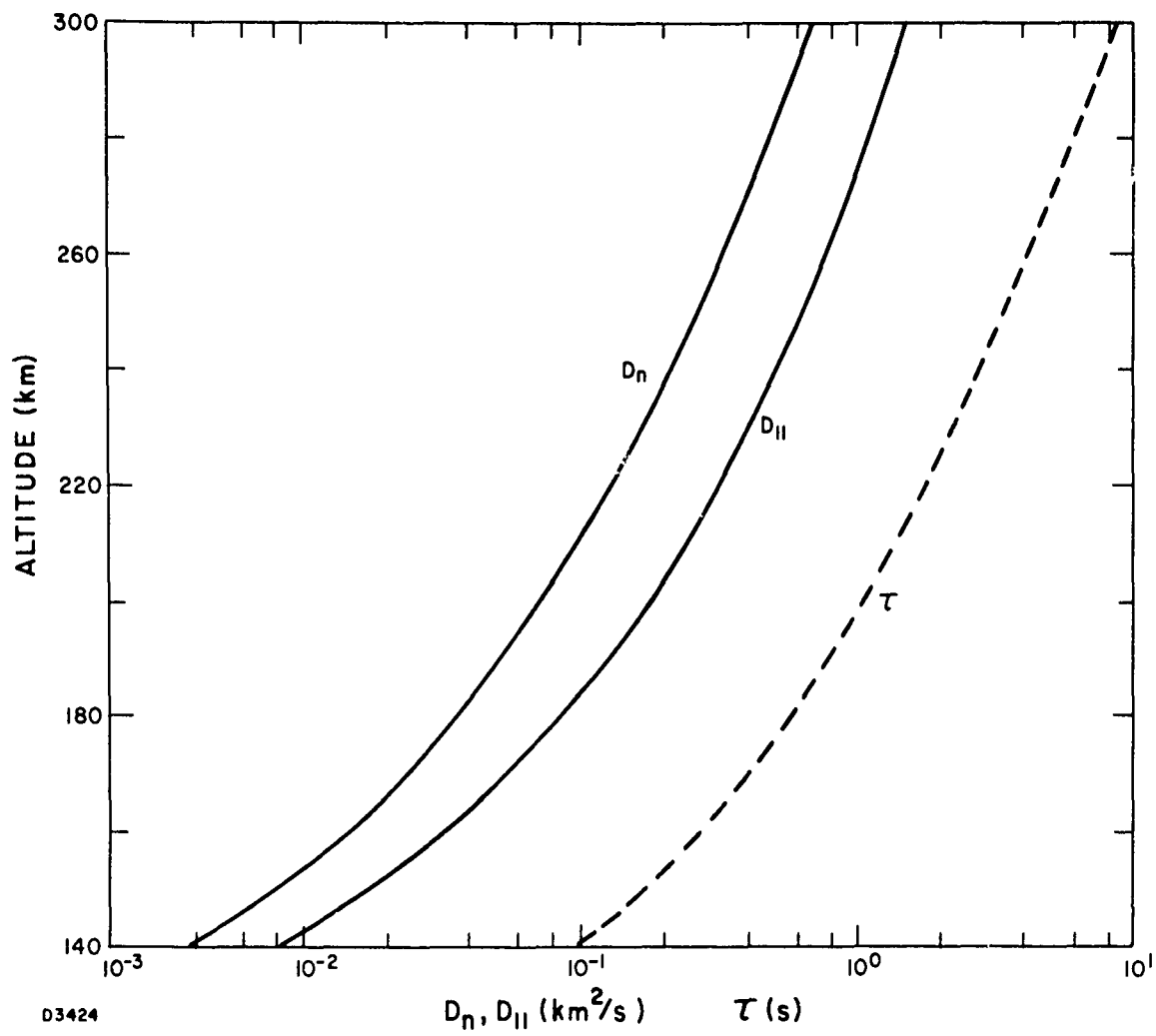


Fig. 1 The Neutral Diffusion Coefficient, the Parallel Ambipolar Diffusion Coefficient, and the Barium Neutral Collision Time as a Function of Altitude

we will choose 24 seconds as being within 20% of the correct value. We shall also take the oxidation rate constant of barium by atmospheric O₂ to be 7.5×10^{-11} cm³/sec. The fraction, f, of available barium atoms that are ionized is equal to the ratio of the photoionization rate to the total loss rate of barium atoms due to both photoionization and oxidation,

$$f = \frac{1}{1 + 1.8 \times 10^{-9} N_{O_2}}. \quad (4)$$

The time constant, t_i, is

$$t_i = 24 f = \frac{24}{1 + 1.8 \times 10^{-9} N_{O_2}} \text{ seconds} \quad (5)$$

and is shown as a function of altitude in Fig. 2.

We first give a qualitative description of how the ion cloud is formed before proceeding with a quantitative model that seems to fit the data very well. We shall be concerned here with the chemical mixture that was used during the Secede II test series. The barium thermite was based on the reaction of 2.5 moles of barium per mole of cupric oxide according to the formula.



In addition, 1.8% of the thermite weight was barium azide. As a result, roughly half of the chemical payload weight was available as excess barium, amounting to $\sim 10^{26}$ barium atoms per 48-kg barium release. Ground tests have shown that most of the gaseous-liquid two-phase flow is vented from the canister in a few tenths of a second. Optical data at high altitudes indicate that the exit velocity is typically of the order of 1 km/sec. Hence, a mixture of liquid Ba O, Cu, and Ba and their vapors rapidly expands

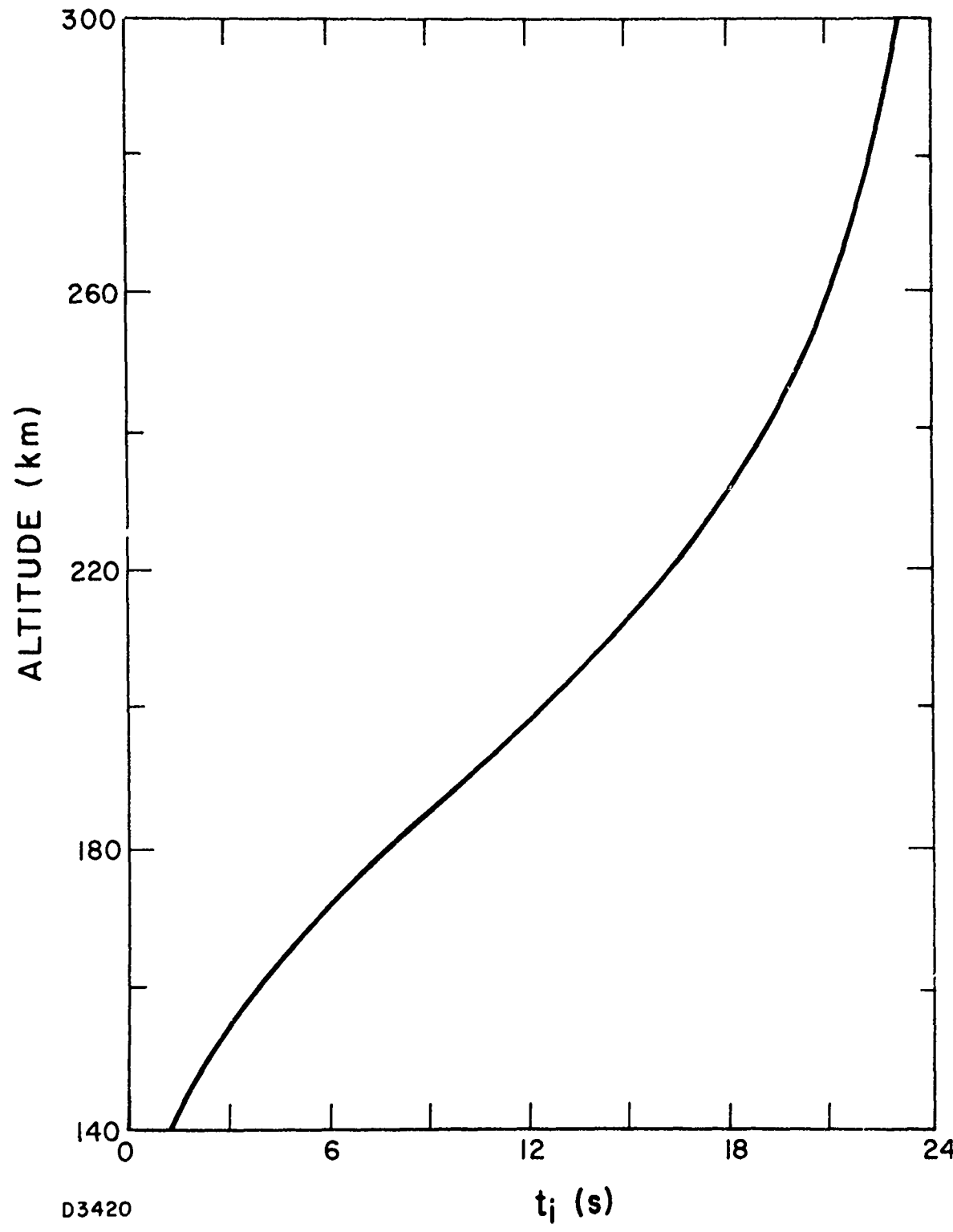


Fig. 2 The Ionization Time Constant as a Function of Altitude

until the gaseous products reach equilibrium with the ambient atmospheric density. Since barium is the most volatile product, most of the vapor should consist of barium atoms. Studies of the barium ejection process have led to the conclusion that most of the barium atoms that are produced are formed by evaporation from hot liquid barium droplets ejected from the canister. The cooled liquid droplets that do not vaporize form the particulate ring whose center of mass follows the rocket trajectory. After the rapid expansion by this barium vapor has ceased, the barium atoms begin diffusing through the ambient atmosphere. At the same time, solar radiation begins exciting ground-state barium atoms into metastable states. The barium atoms in the excited states are then lost by the competing processes of ionization and oxidation by molecular oxygen, with the time constant t_i given by Eq. (5). Once the ions have been created they are tied to the earth's magnetic field lines and can no longer diffuse perpendicular to the magnetic field. Hence the scale size of the ion cloud transverse to the magnetic field should bear some relation to the transverse scale size of the neutral cloud at early times. Also within a few time constants t_i , the barium atoms either become barium ions or have been oxidized to become BaO.

We shall be concerned here only with the dense ion cloud formed from the initial ionization of barium atoms. We shall not be concerned with the less dense ionization that is formed by the photodissociation of BaO and subsequent ionization of the barium atom. This second process takes place on a time scale at least two orders of magnitude slower than the primary process and gives rise to densities two orders of magnitude less than the peak densities of concern to us here.

Now let us discuss a quantitative model for the formation of the main ion cloud, the formation of which depends on the early-time behavior of the neutral vapor. Initially, the barium vapor at high density compared to the ambient can be taken to fill a sphere whose outer edge expands radially at 1 km/s, a much larger velocity than a barium atom thermal velocity at ambient temperature. At a later time, after the barium atoms have lost most of their directed, radial velocity and have expanded so that their concentration is small compared to the ambient concentration, the distribution of barium atoms can be taken to be a spherical gaussian expanding by diffusion through the ambient air at less than a thermal velocity. There exists no model that incorporates the physical processes responsible for the transition between this initial and later-time behavior. In order to develop a quantitative description of this transition, we shall adopt the following model. We shall assume that the initial mass of vapor uniformly fills a sphere of radius $R(t)$ and that the initial momentum of the vapor mass is shared with the mass of ambient air contained inside this radius. The assumption that the velocity within the sphere increases linearly with radius, r , from zero at the center to dR/dt at $r = R$ satisfies flux conservation. We define an equal mass radius, a_0 , as

$$a_0 = (3M/4\pi\rho)^{1/3} \quad (7)$$

where M is the mass of the vapor and ρ is the mass density of the ambient atmosphere. The equation expressing the conservation of momentum described above can be written

$$\left[1 + \left(\frac{R}{a_0} \right)^3 \right] \frac{dR}{dt} = 1 \text{ km/s} \quad (8)$$

giving the time behavior of the radius of the vapor bubble. When the dR/dt has decreased to a typical barium thermal velocity of 0.3 km/s, the vapor bubble has a radius $R = 1.27 a_0$ and it takes $1.92 a_0$ seconds to reach this radius. Until R reaches a_0 at $t = 1.25 a_0$ seconds, the barium vapor is denser than the surrounding atmosphere and will certainly be optically thick to the metastable exciting solar radiation. Hence, we shall assume that the formation of barium ions begins only $1.25 a_0$ seconds after release.

Equation (8) underestimates the radius of the neutral cloud as a function of time. A single barium atom traveling at 1 km/s will have a mean free path of τ km where τ is the collision time given in Eq. (1) and plotted in Fig. 1. A high-velocity barium atom will lose only $1/3$ of its velocity in a single collision with a typical air molecule which is five times lighter. Hence we might expect the mean velocity, V , of a cluster of barium atoms to behave exponentially with time as $\exp(-t/3\tau)$ during the $0.67 a_0$ seconds that the barium vapor is less dense than the surrounding air. Thus we assume that the radius of the neutral barium vapor is larger than $1.27 a_0$.

$$\int_0^{0.67 a_0} V(t) dt = 3\tau [1 - \exp(-0.67 a_0/3\tau)] \text{ km} \quad (9)$$

After $1.92 a_0$ seconds after release we assume that the neutral vapor continues to increase in size by ordinary diffusion giving rise to a typical gaussian radius (defined as the e-folding radius for the density) as a function of time of

$$a_n(t) = \left\{ \left[1.33 a_0 + 3\tau \left(1 - \exp \left[-0.67 a_0 / 3\tau \right] \right) \right]^2 + 4D_n(t - 1.92 a_0) \right\}^{1/2} \text{ km.} \quad (10)$$

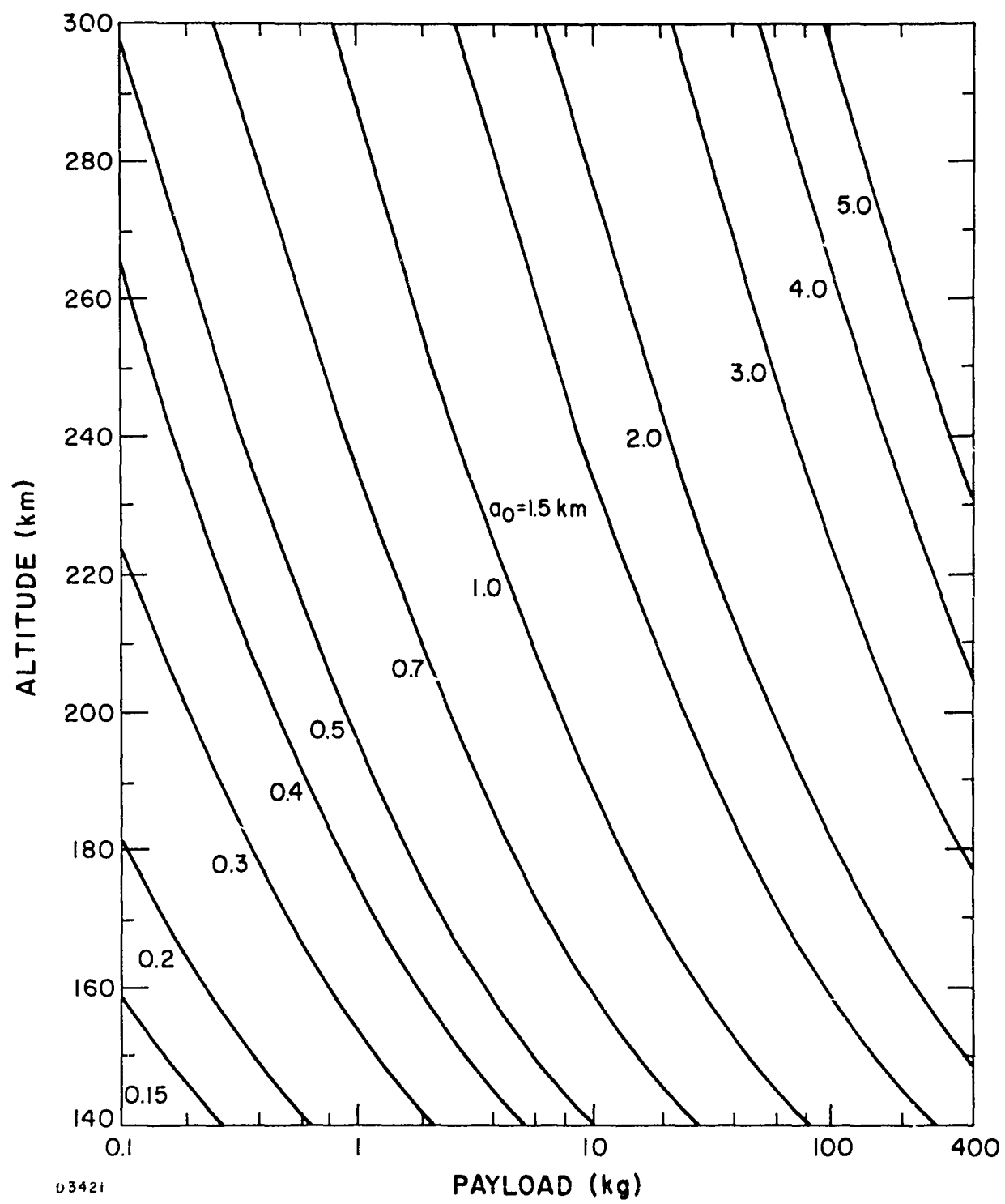


Fig. 3 The Equal Mass Radius as a Function of Altitude and Payload Under the Assumption that the Vapor Mass is Equal to 0.2 P

While the neutral cloud is expanding according to the model described above, ions are being formed and deposited on magnetic field lines. We assume that the scale size of the ion cloud transverse to the magnetic field is given by the gaussian radius of the neutral cloud at two ionization time constants after ionization is assumed to have begun, or

$$a_{\perp} = a_n(t_1) \quad (11)$$

where

$$t_1 = 2t_i + 1.25a_o \text{ seconds.} \quad (12)$$

For our model we have assumed that the mass of the vapor produced in the barium release is 1/5 of the total chemical payload weight. The equal mass radius defined by Eq. (7) sets the initial scale size for the neutral cloud and the initial time scale of the expansion and is shown in Fig. 3 as a function of altitude and payload. The ion cloud scale size transverse to the magnetic field given by Eqs. (10), (11), and (12) is shown in Fig. 4 as a function of altitude and payload.

We now assume that 6.25×10^{23} P barium atoms are produced where P is the chemical payload in kilograms. This number corresponds to a 30% vaporization efficiency for the barium release, which is considerably higher than has been obtained in laboratory tests but is not inconsistent with some estimates of the total ion inventory in large barium releases as we shall discuss below. The mass chosen above for the vapor corresponds to 40% more than the mass of the barium atoms alone. This

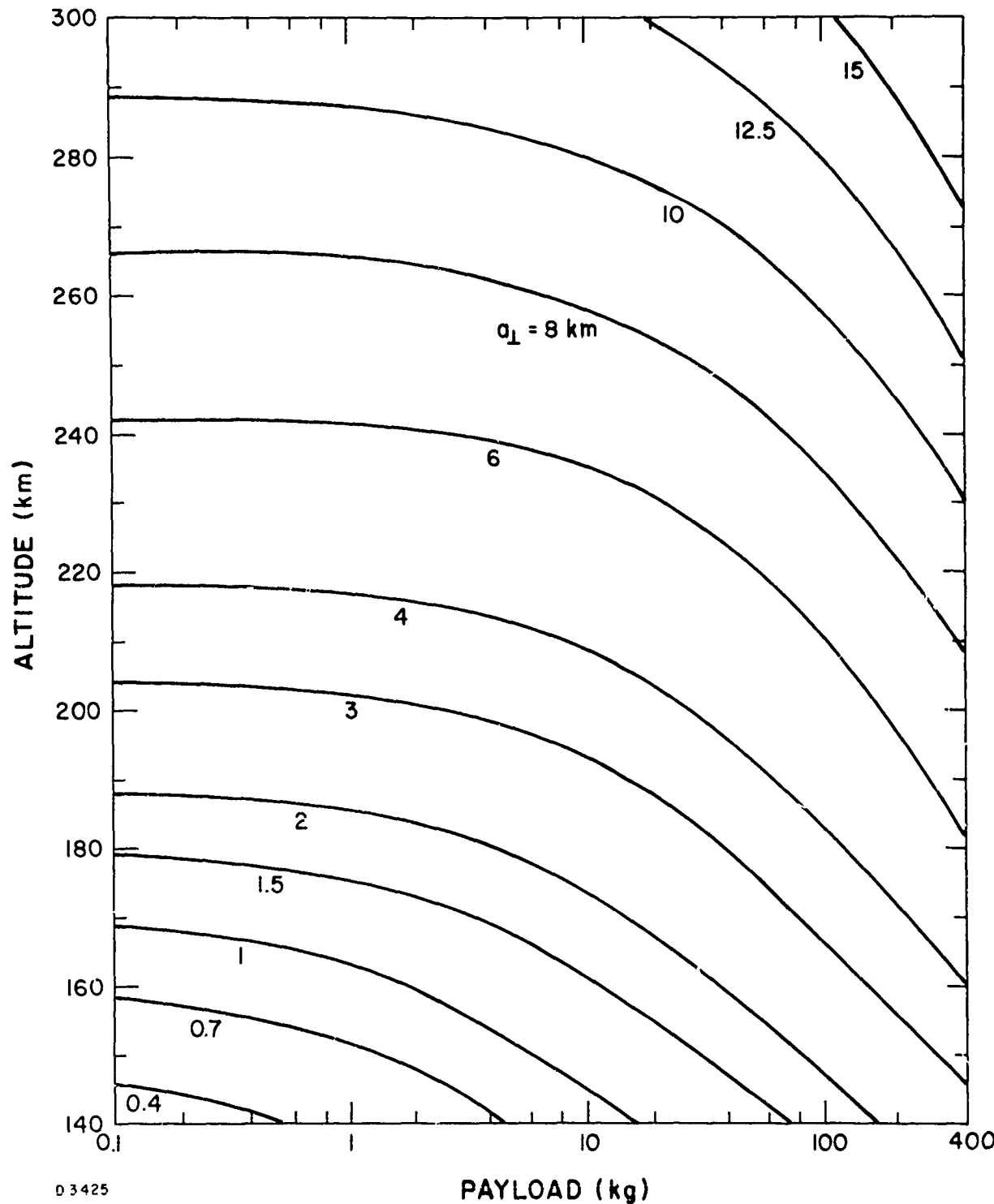


Fig. 4 The Scale Size of the Ion Cloud Transverse to the Magnetic Field as a Function of Altitude and Payload as Given by Eq. (11)

choice appears to lead to good agreement of the model with observations, although there is good reason to believe that the vapor consists almost entirely of barium atoms. Only the fraction f given by Eq. (4) of the barium atoms produced will form ions. An estimate of a peak electron density, n_p , can be made assuming that $f \times 6.25 \times 10^{23} \times P$ ions are distributed throughout a sphere of gaussian radius a_1 km:

$$n_p = \frac{f \times 6.25 \times 10^8 P}{\pi^{3/2} a_1^3} \text{ cm}^{-3}. \quad (13)$$

The value of n_p is shown as a function of altitude and payload in Fig. 5.

Since ions cannot diffuse across the magnetic field lines, the number of ions on each magnetic field line remains constant. Hence we can easily estimate the peak electron content deposited on a magnetic field line by integrating the gaussian distribution parallel to the magnetic field resulting in

$$N_L = \frac{f \times 6.25 \times 10^{13} P}{\pi a_1^2} \text{ cm}^{-2} \quad (14)$$

The maximum number of electrons on a field line given by Eq. (14) is shown as a function of altitude and payload in Fig. 6.

C. INTERMEDIATE TIME BEHAVIOR

In the preceding section we have developed a model that suggests that at $t - t_1$ s after release given by Eq. (12), the ion cloud is a sphere with a gaussian radius given by Eq. (11) and with a peak electron density given by Eq. (13). Subsequently, the electron density decays as the ionization spreads out parallel to the magnetic field by ambipolar diffusion. Hence the gaussian length parallel to the magnetic field is given by

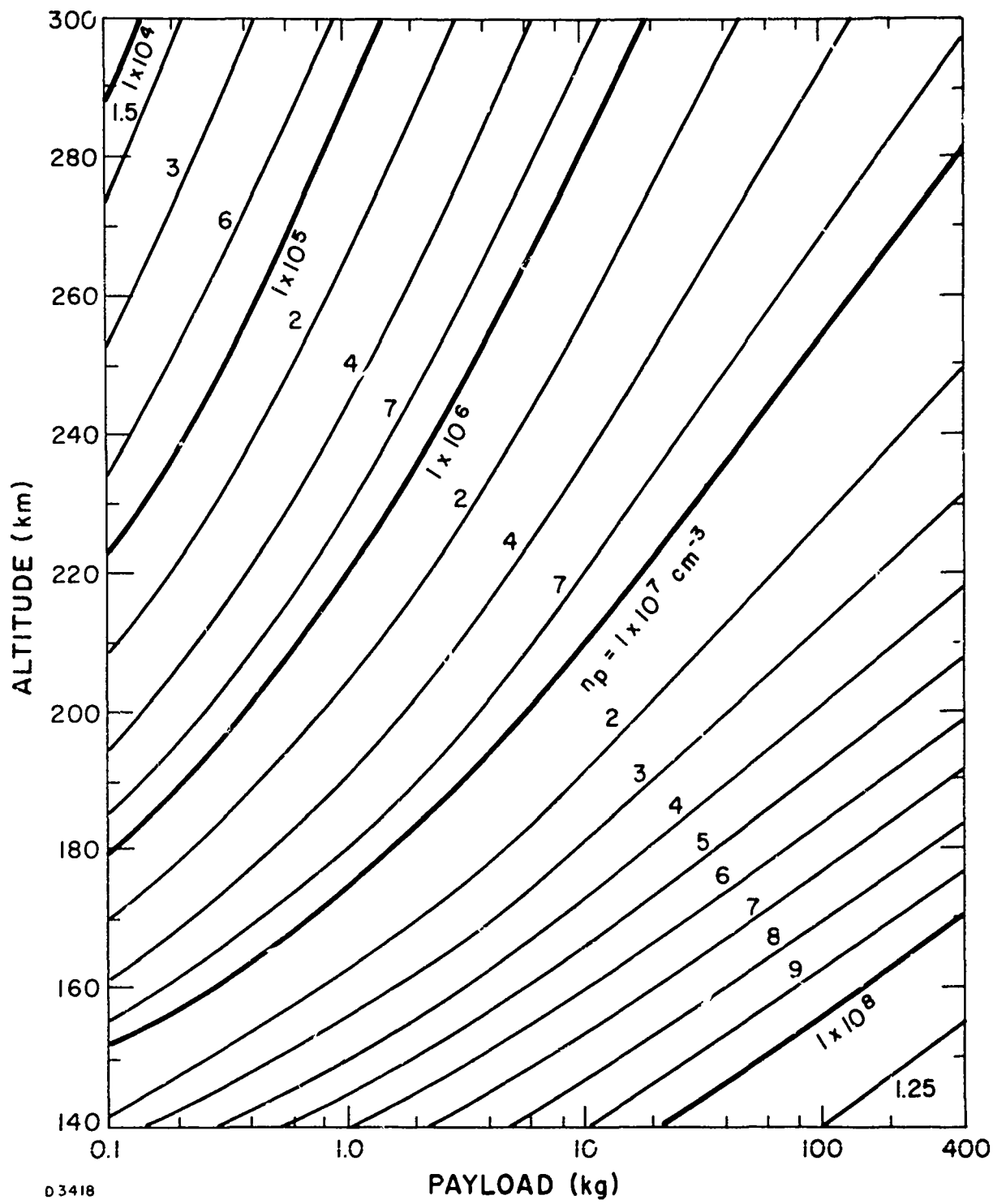


Fig. 5 The Upper Limit to the Peak Electron Density in the Ion Cloud as a Function of Altitude and Payload as Given by Eq. (13)

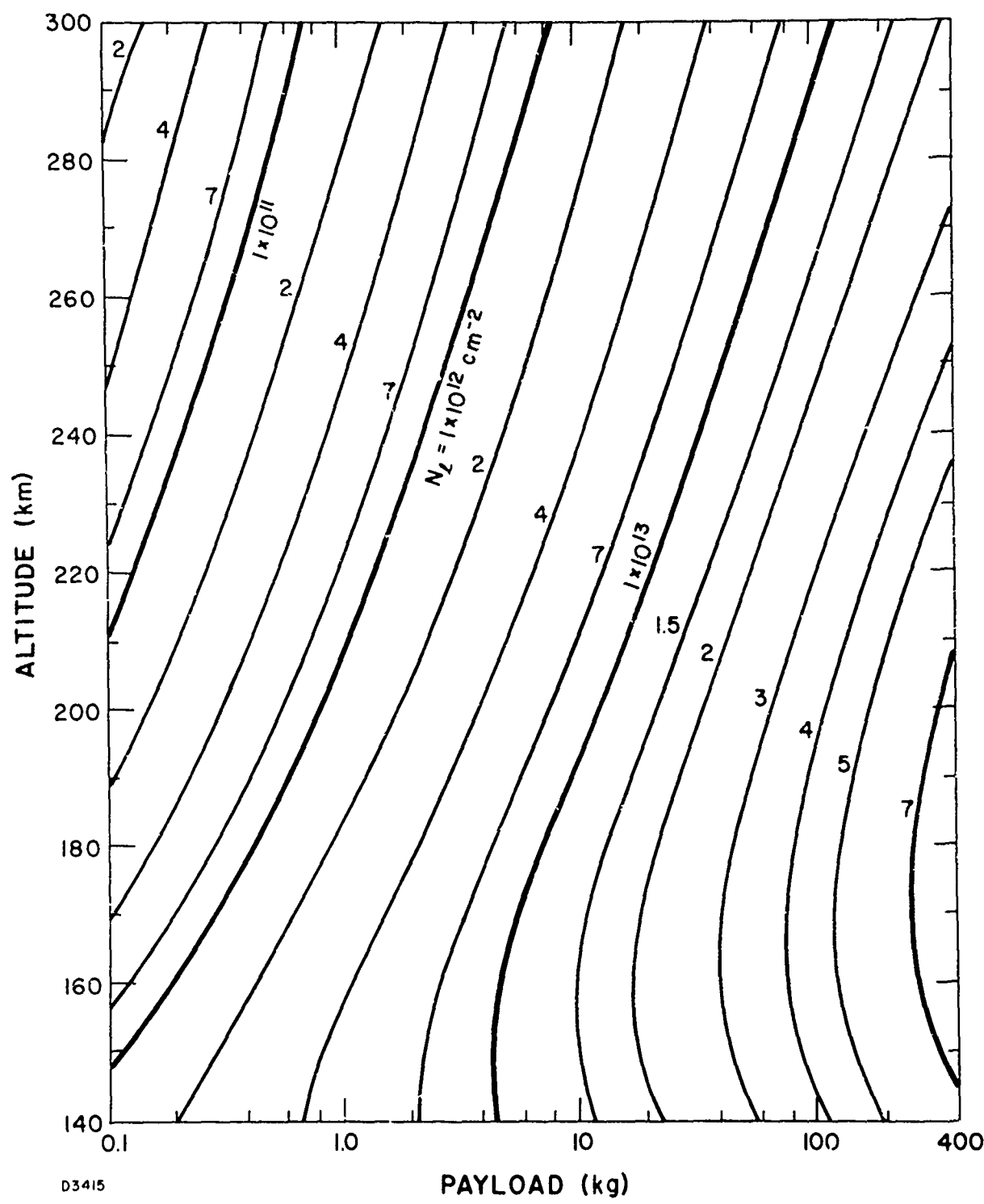


Fig. 6 The Electron Content on a Magnetic Field Line as a Function of Altitude and Payload as Given by Eq. (14)

$$\ell(t) = \left[a_{\perp}^2 + 4D_{\parallel}(t - t_1) \right]^{1/2} \text{ km.} \quad (15)$$

The electron density at one minute after release is then given by

$$n(60) = \frac{N_{\ell} \times 10^{-5}}{\sqrt{\pi} \ell(60)} \text{ cm}^{-3} \quad (16)$$

(ℓ is given in kilometers) and is shown as a function of altitude and payload in Fig. 7. The electron density begins to decrease approximately as $t^{-1/2}$ at times long compared to

$$t_2 = \frac{a_{\perp}^2}{4 D_{\parallel}} \quad (17)$$

which is shown as a function of altitude and payload in Fig. 8

D. LATE-TIME BEHAVIOR

The atmosphere was assumed to be of constant density in the previous section since the size of the ion cloud was small compared to a neutral density scale height. However, the large value of the ambipolar diffusion coefficient causes the ion cloud to grow to an appreciable fraction of the neutral atmosphere scale height in the direction parallel to the magnetic field. The distribution of ions parallel to the magnetic field will become distorted from a gaussian shape and assume a new quasi-equilibrium shape as obtained by Bannister and Davis³ and illustrated for the case of barium ion clouds by Pendyala⁴,

$$n(z) = n_{\max} \exp \left\{ -\frac{z}{H_i} - \frac{H_n}{H_i} \left[\exp \left(-\frac{z}{H_n} \right) - 1 \right] \right\} \quad (18)$$

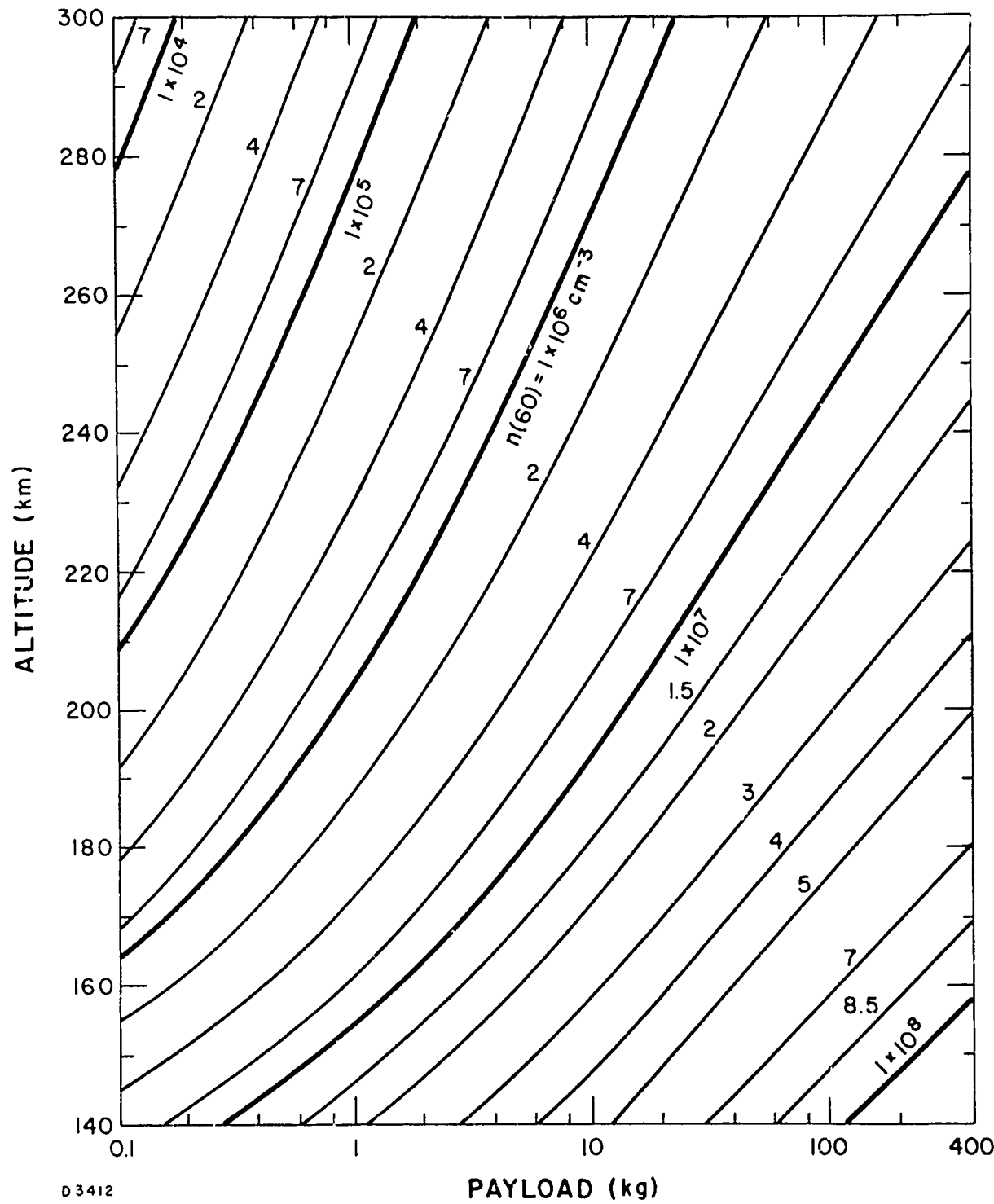


Fig. 7 The Peak Electron Density at One Minute after Release as a Function of Altitude and Payload

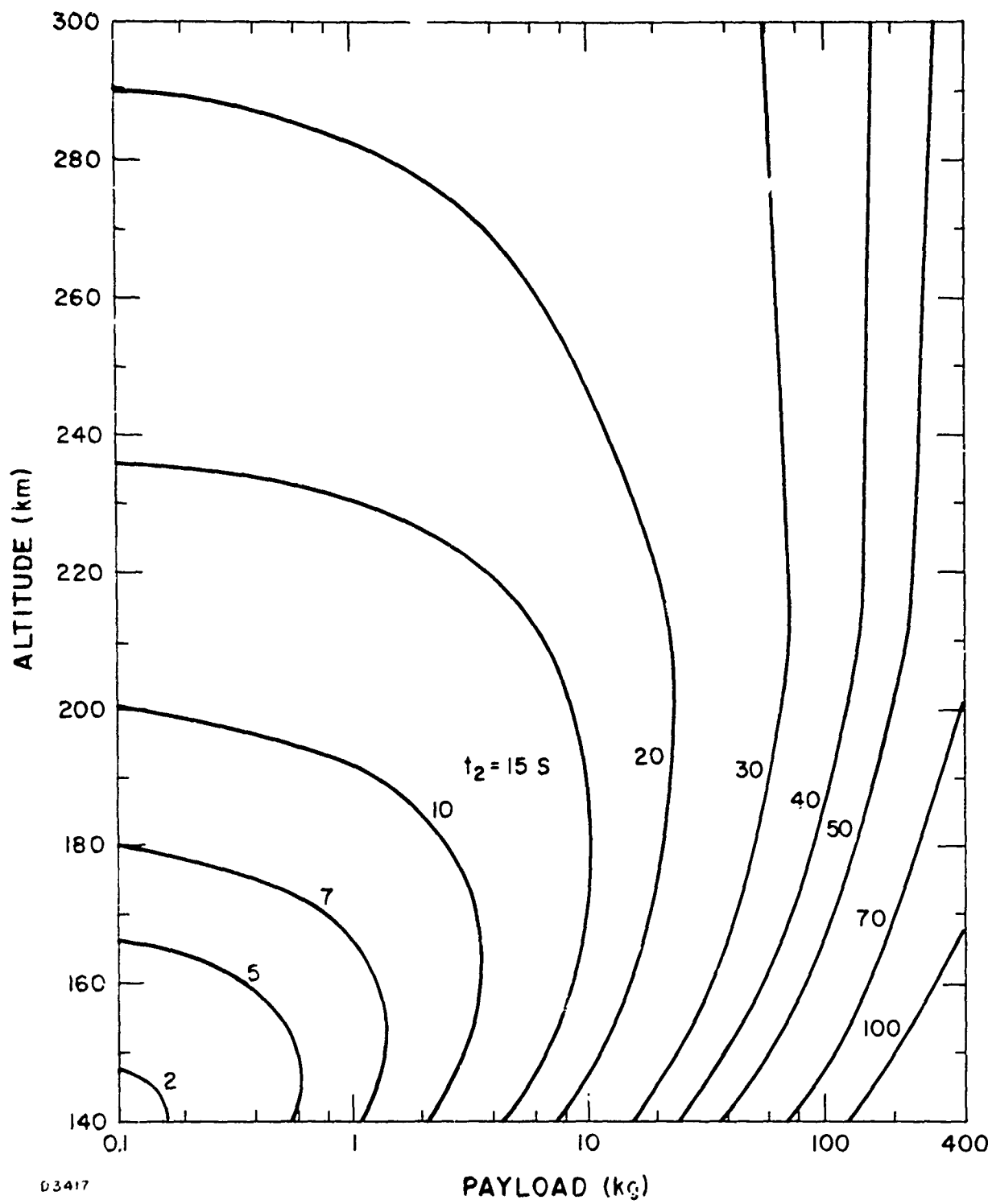


Fig. 8 The Time at Which Ambipolar Diffusion Parallel to the Magnetic Field Begins to Cause a Decrease as $t^{-1/2}$ in the Peak Electron Density of the Ion Cloud

where z is measured from the peak of the electron density and H_i is the barium-ion scale height, $D_{||}/g\tau$. On the topside at large positive z , the density varies as $\exp(-z/H_i)$ while near the peak the electron density has a gaussian shape

$$n(z) \sim n_{\max} \exp \left[-z^2/\ell_A^2 \right]; \quad z \ll H_n \quad (19)$$

with a gaussian length of

$$\ell_A = \sqrt{2H_i H_n}. \quad (20)$$

This gaussian length is shown as a function of altitude in Fig. 9.

The profile given by Eq. (18) is in quasi-equilibrium and indicates that the peak ion density eventually decreases to a constant value at a given height. This asymptotic value of the density in the ion cloud is given by

$$n_A = \frac{N_k \times 10^{-5}}{\sqrt{\pi} \ell_A} \quad (21)$$

and is shown as a function of altitude and payload in Fig. 10. Before this equilibrium distribution is reached, the peak electron density has been decreasing inversely as the gaussian scale length $\ell(t)$ given by Eq. (15) or roughly as $t^{-1/2}$. An estimate of the time, t_A , at which the electron density stops decreasing and approaches its asymptotic value given by Eq. (21) is made by setting $\ell(t_A)$ equal to $(H_i H_n)^{1/2}$ resulting in

$$t_A = t_1 + \frac{H_i H_n - a_1^2}{4 D_{||}} \quad (22)$$

which is shown as a function of altitude and payload in Fig. 11.

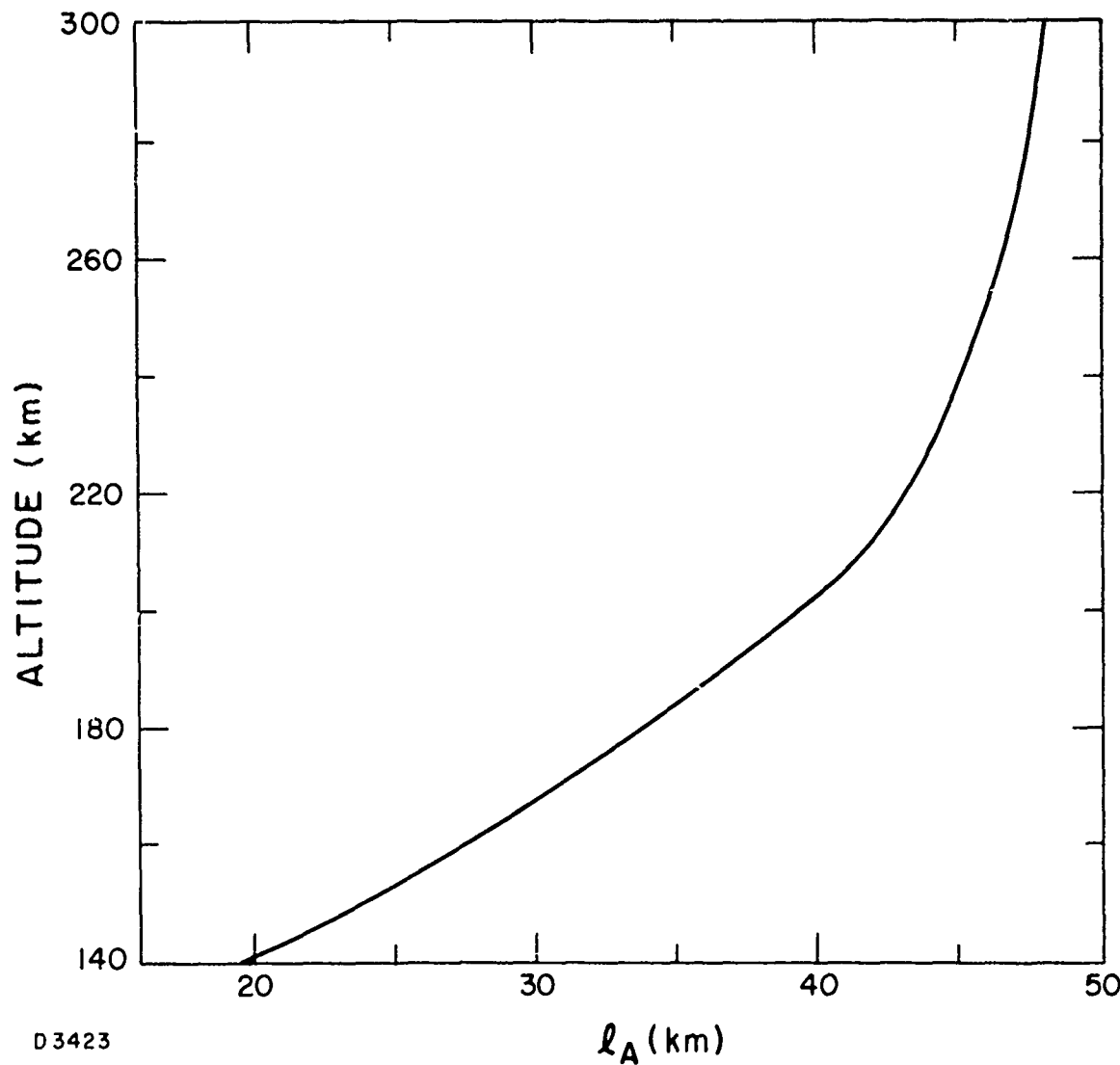


Fig. 9 The Gaussian Length Along the Magnetic Field for a Barium Ion Cloud in Diffusive Equilibrium

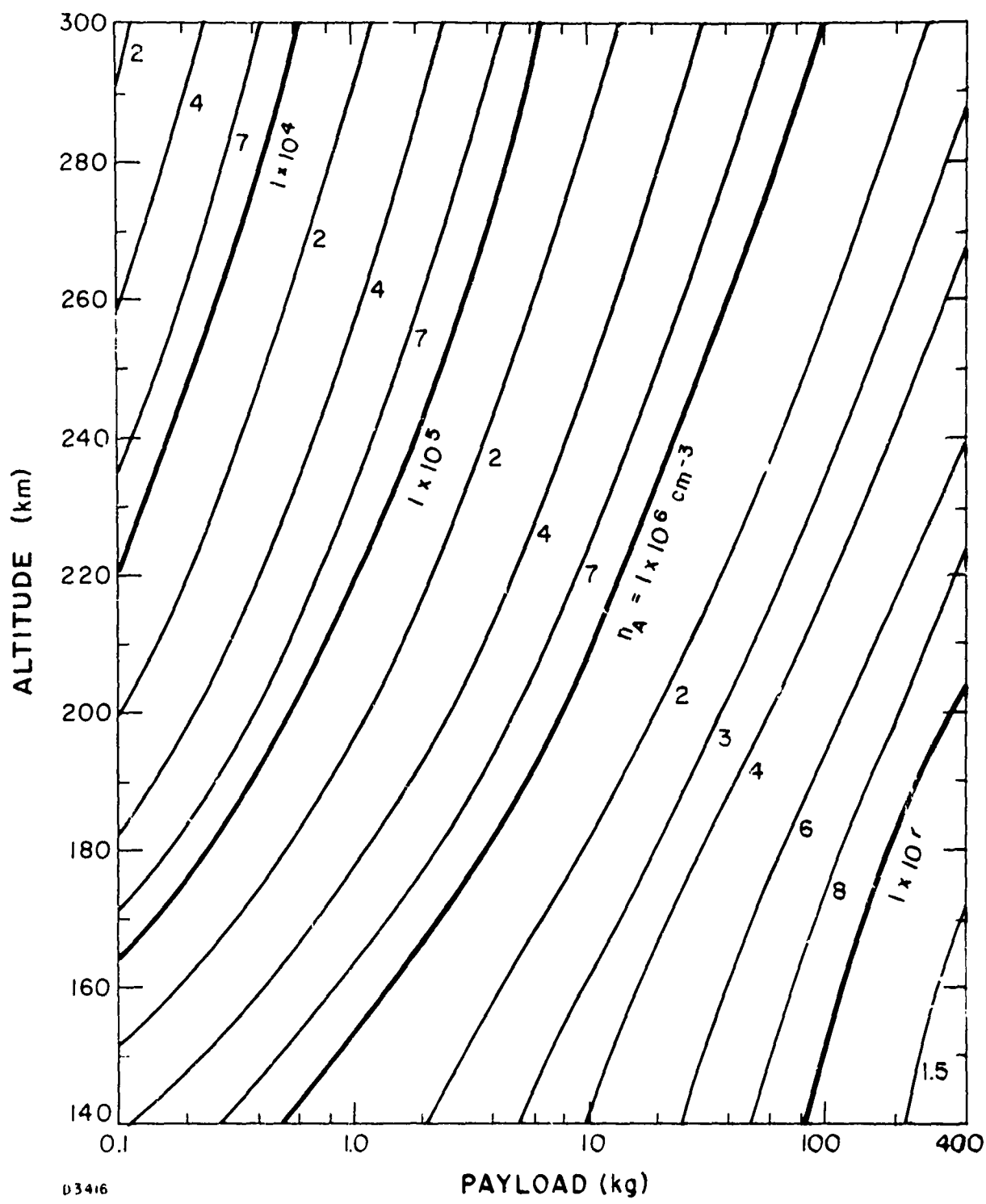


Fig. 10 The Asymptotic Value of the Peak Electron Density as a Function of Altitude and Payload

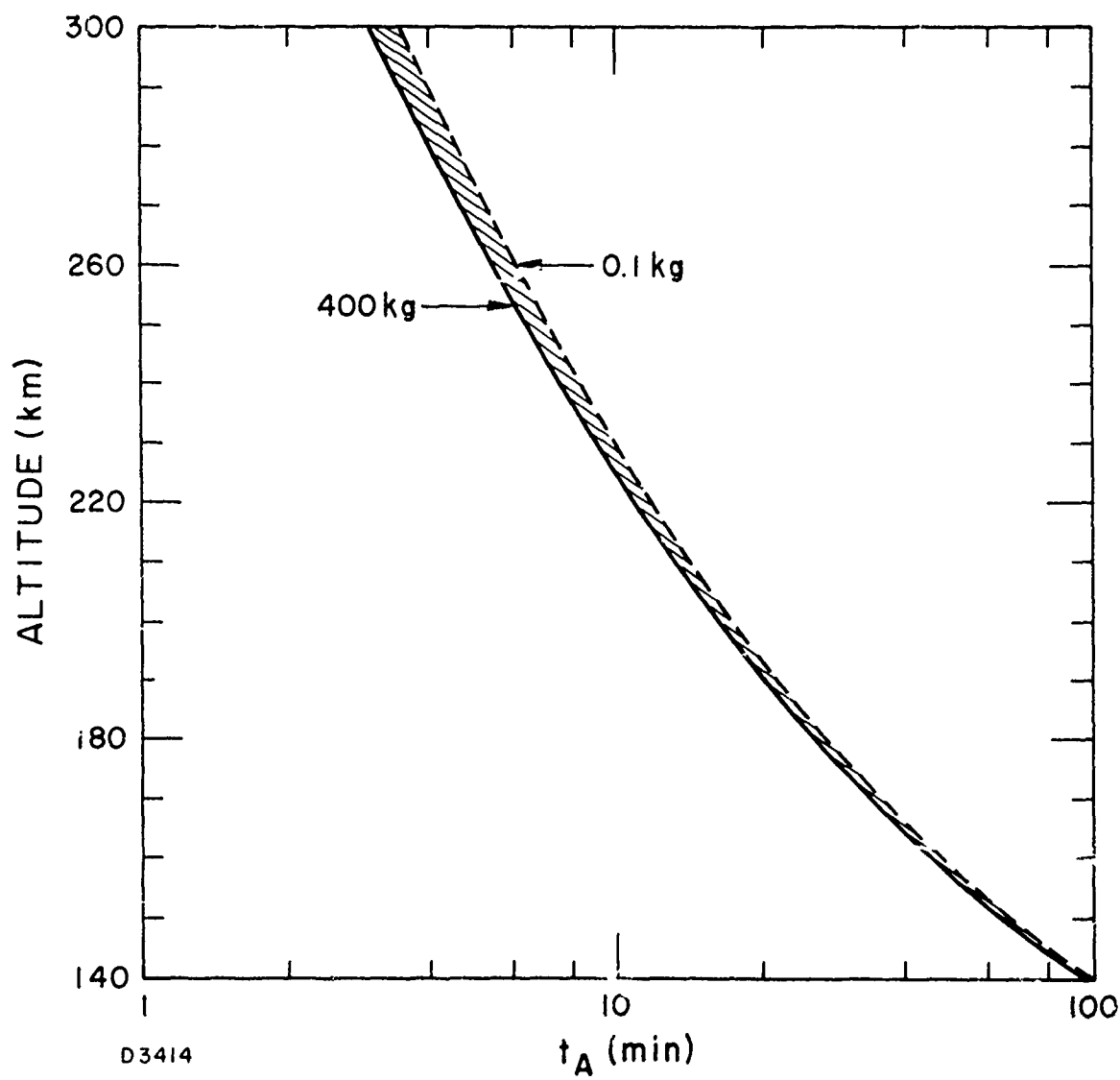


Fig. 11 The Time at Which the Peak Electron Density of the Barium Ion Cloud Ceases Decreasing as $t^{-1/2}$ as a Function of Altitude and Payload

In the previous discussion, it has been assumed that the ion cloud has remained at the altitude of release. In fact, barium-ion clouds have descended in altitude with typical vertical velocities of 20 m/s. This change in altitude can come about from a combination of factors. The principal causes are gravitational drag on the ions, components of the neutral wind, V_D or V_N , in the downward, or northward, directions, respectively, and a westward component of the electric field, E_w . These factors lead to a downward drift velocity of the ion cloud of

$$V_{ID} = (V_D + g\tau) (1 - \zeta \cos^2 \theta_d) + \zeta (V_N \sin \theta_d + \frac{E_w}{B}) \cos \theta_d \quad (23)$$

where θ_d is the dip angle of the magnetic field and $0 < \zeta < 1$ is the coupling parameter, which depends on the conductivity of the ion cloud as described in Chapter 5D. The resulting change in altitude has important effects on the time dependence of the peak electron density. The first effect is a decrease in the rate at which $\ell(t)$ increases due to smaller $D_{||}$ at lower altitudes. Thus the peak electron density can be expected to decrease more slowly than $t^{-1/2}$ if the downward drift of the ion cloud is of the order of $H_n/t_A \sim 4 g\tau$ [obtained by using Eq. (22)] or larger. This criterion becomes easier to satisfy at lower altitudes. The second effect is an increase in the asymptotic value of the peak electron density, n_A , since ℓ_A also decreases at lower altitudes.

We are now in a position to describe the time variation of the peak electron density in an ion cloud. We assume that the ions are continuously created with a time constant t_i given by Eq. (5) and deposited in a sphere of gaussian radius a_1 given by Eq. (11) for times less than t_1 given by Eq. (12). At times greater than t_1 , the electron density begins to decrease inversely

as the gaussian length $\ell(t)$ given by Eq. (15) increases. The electron density decreases until times t_A given by Eq. (21) at which time the density begins to approach its asymptotic value n_A given by Eq. (21). Thus we have

$$n(t) = \begin{cases} 0 & ; t < 1.25 a_0 \\ \frac{N_\ell}{\sqrt{\pi} a_1} \left[1 - \exp \left(-(t - 1.25 a_0)/t_i \right) \right] & ; 1.25 a_0 < t < t_1 \\ \frac{N_\ell}{\sqrt{\pi} \ell(t)} \left[1 - \exp \left(-(t - 1.25 a_0)/t_i \right) \right] & ; t_1 < t < t_A \\ n_A & ; t > 2 t_A \end{cases} \quad (24)$$

The time histories of the peak electron concentration obtained in this manner for several typical cases of interest are shown in Figs. 12 and 13. Figure 12 shows the time history for 48 kg payloads at altitudes of 150, 190 and 250 km., while Fig. 13 shows a comparison of several different payloads at around 190 km altitude. Note that the peak electron density given by expression (24) is typically approximately 10% less than the peak given by Eq. (13) due to the fact that all of the barium atoms have actually not been photoionized by $t = 2t_1$. It should be pointed out that it is possible for the peak electron density to increase slowly at late times due to a slow change in altitude. This possibility is indicated by the shaded widths of the lines at late-time corresponding to a 50-km descent in altitude for the high altitude releases. In general it has been observed that the location of the peak in the electron density does tend to decrease in altitude with time.

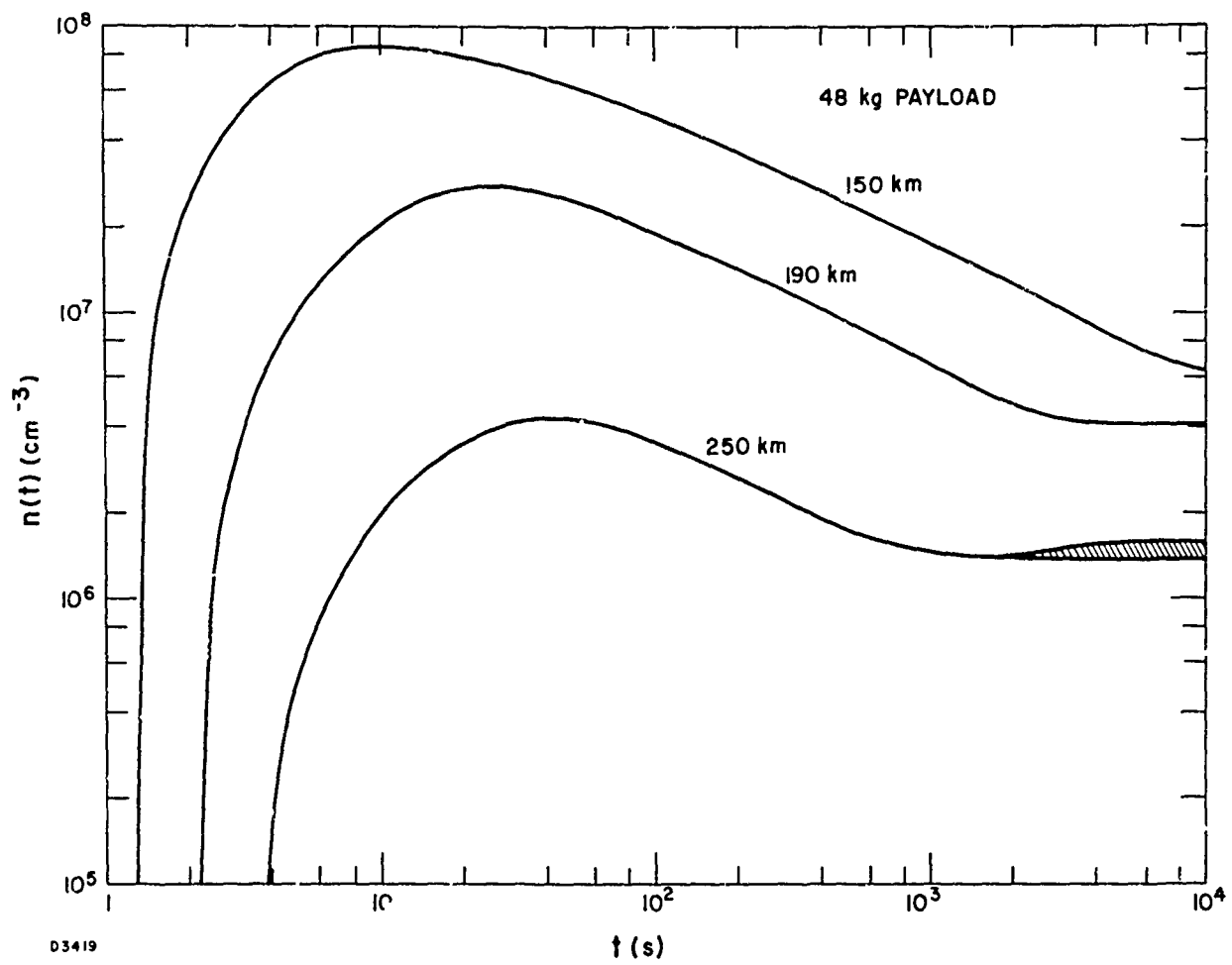


Fig. 12 The Time History of the Peak Electron Density for 48-kg Releases at Three Different Altitudes

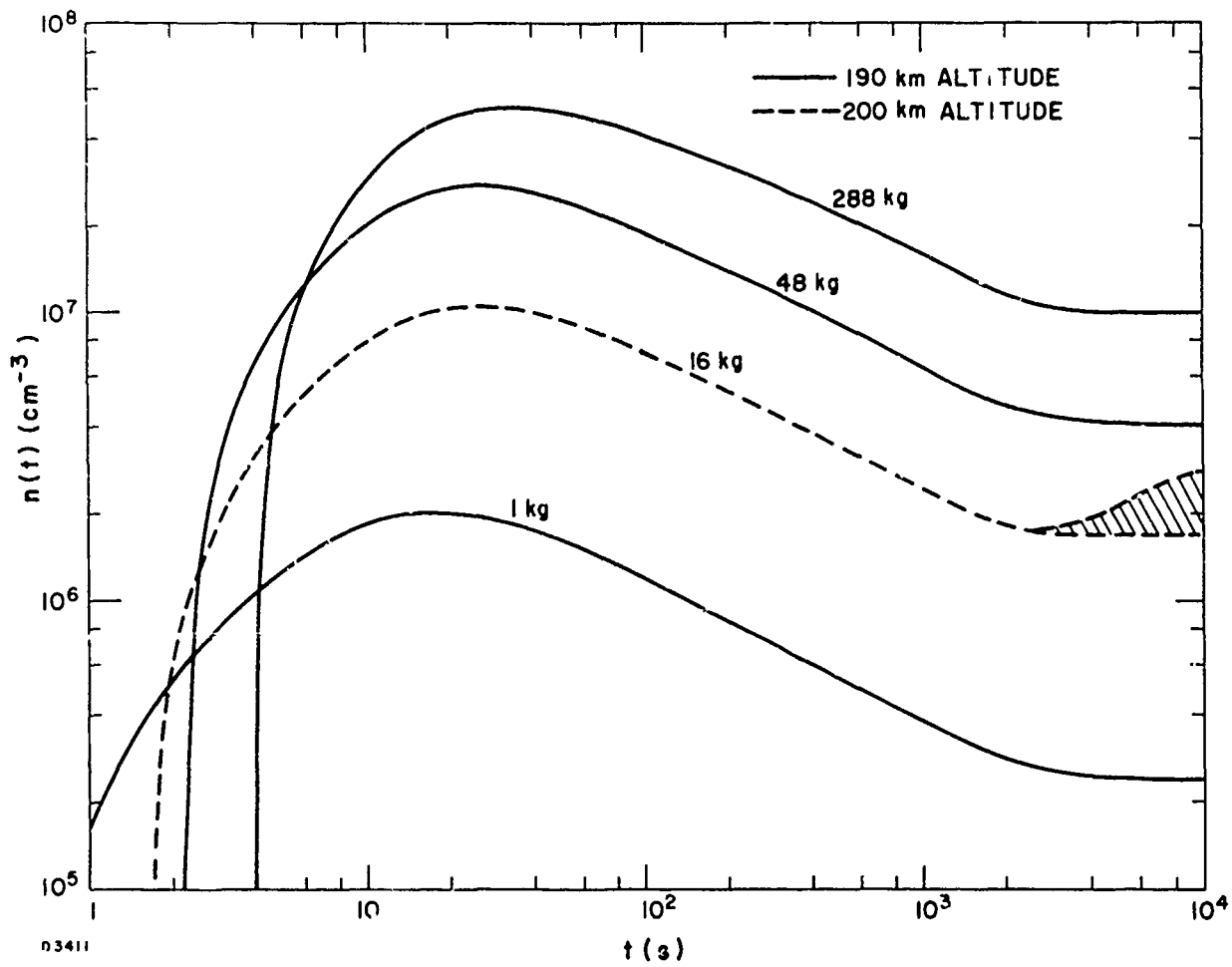


Fig. 13 The Time History of the Peak Electron Density for Several Different Payloads at an Altitude of Around 190 to 200 km

Since the asymptotic value of the density, Eq. (21), varies inversely as the asymptotic gaussian length ℓ_A given by Eq. (20), the late-time electron density can slowly increase as the cloud descends in altitude. A more rapid descent in altitude will cause the electron density to decrease more slowly than shown in Figs. 12 and 13 as discussed above. One must not base the late-time behavior of the peak electron density on the altitude of release if it indeed is descending in altitude.

E. COMPARISON WITH DATA

We are now in a position to evaluate the results given by this model. Although the model has a reasonable physical basis, the values of the parameters used were chosen to give agreement with optical and radar data. The first point to make is that the value of the barium-neutral collision time, τ , given by Eq. (1) is in agreement with the optical and radar measurements of the time variation of the gaussian radius of the neutral cloud and the time variation of the gaussian length of the ion cloud parallel to the magnetic field. In addition to the physical modeling, this parameter is the single most important parameter in obtaining the results that have been given above.

The optical data have also been used to obtain an estimate of the early-time expansion of the neutral cloud and estimates of the most likely scale size of the ion cloud transverse to the magnetic field. This estimate is difficult to make accurately because the ion cloud is optically thick to its resonance radiation, which tends to result in too large an estimate. However, by recognizing that one is primarily concerned with the scale size of the high density portion of the ion cloud, one could sometimes obtain the best estimate of the appropriate scale size many minutes after release

when the dense core has moved away from the denser portions of the surrounding ion bridge. This determination at these later times can be complicated by the fact that the ion cloud has elongated considerably, parallel to the magnetic field. Hence, we have had to use our judgment in obtaining the best estimates with which we wish to match the model.

The HF long pulse radar data provide a lower bound on the peak electron density. At early times when the ion cloud has not been distorted very much from a gaussian shape, this measurement probably provides a fairly reliable estimate of the peak ion density. However, due to the changing aspect of the ion cloud, the additional ionization deposited in the ion bridge, and the structuring that takes place in the ion cloud at later times, the HF data provide a less reliable estimate at later times. Hence, we have tended to place a larger reliability on the times of the dropout of the highest frequencies tended to occur in the time range $t_1 < t < t_A$ where the peak density given by Eq. (24) is felt to be most reliable.

Table 1 presents a comparison of the data with the values of several parameters obtained from the model. The ion-cloud radius is estimated from optical data, and the ion-cloud densities are given for each event at the time after release indicated. We see that the model estimate of the scale size of the ion cloud transverse to the magnetic field, a_{\perp} , is in excellent agreement with estimates obtained by the optical data. The value of the peak electron density obtained from the HF data for the 48-kg payload at 190 km represents an average of the Dogwood, Spruce and Quince data at 100 s after release. The model gives excellent estimates for these nominal releases. In particular the estimate for the electron content agrees with the value produced by Event Quince as measured by Faraday rotation. Events Dardabasi I and Redwood I are also modeled very accurately.

TABLE I. CORRELATION OF MODEL WITH
OPTICAL AND RADAR DATA

Event	Payload (kg)	Altitude (km)	DATA			MODEL ESTIMATES		
			Ion-Cloud Radius (km)	Time $R +$ (sec)	Electron Density (cm $^{-3}$)	a_{\perp} (km)	f (km)	n (cm $^{-3}$)
Nutmeg	48	150	1.5-2.0	160	$>1.6 \times 10^7$	1.8	4.2	4.1×10^7
Dogwood	48	190	3.5-4.0	100	1.9×10^7	3.8	8.3	1.9×10^7
Spruce								2.8×10^{13}
Quince								
Olive	288	193	5.5-6.25	180	3.5×10^7	6.1	11.5	3.4×10^7
Dardabasi	16	200	---	---	7×10^6	3.6	8.3	7.4×10^6
Redwood	48	255	3-11	100	3.5×10^6	8.9	18	3.6×10^6
								9.8×10^{12}

In the case of Olive the returns from the 36 MHz radar, corresponding to a density of $1.6 \times 10^7 \text{ cm}^{-3}$, dropped out at 660 seconds after release. By extrapolating backward using a $t^{-1/2}$ decay law, one obtains an estimate of $3.1 \times 10^7 \text{ cm}^{-3}$ at three minutes after release. At the same time the incoherent backscatter radar was measuring a peak concentration of the order of $5 \times 10^7 \text{ cm}^{-3}$. This latter radar technique has consistently tended to give values of peak electron density somewhat higher than those indicated by the HF radar. We also note that Olive II and Olive III have not been included in the tabulated model estimate. Each of these releases can be expected to be similar to Dardabasi at 3 minutes after release and could thus contribute an additional $1.1 \times 10^7 \text{ cm}^{-3}$ to the indicated value of the peak density for Olive. Since these two events did not occur at the same altitude as the main ion cloud, this latter estimate of $4.5 \times 10^7 \text{ cm}^{-3}$ represents an upper bound to the estimated peak density of Olive. On the other hand, the total electron content in the three Olive releases is one-third larger than the result given in Table 1 for Olive I alone.

The model predicts a high value of the electron density for Nutmeg I. This value is not inconsistent with the data. The 36-MHz signal dropped out at 160 seconds after release and the next two lower frequencies dropped out considerably faster than a $t^{-1/2}$ law would predict. However, optical records show that Nutmeg I was definitely striated before 105 seconds after release and previous experience has shown that the HF radar tends to underestimate the ion-cloud electron density when the cloud is striated. We suggest that the value given by the model is an accurate estimate of the electron density in Nutmeg I.

The time histories for the peak electron density for the sample cloud shown in Figs. 12 and 13 also are quite reasonable and do not conflict with any radar data. In particular the asymptotic values of the density shown in Figs. 10, 12, and 13 provide an explanation for the fact that HF returns from ion clouds last for very long times after release. This result indicates that the scattering at late time is indeed from electron densities that exceed the critical density. It should be remembered that the asymptotic values given in Fig. 10 are for a release whose peak remains at the release altitude. As the ion cloud descends, the inventory on a field line remains constant and the peak density increases as ℓ_A given by Eq. (20) decreases. The asymptotic value can also be obtained by cross-plotting along constant content contours with the aid of Fig. 6.

The most important parameter that is necessary for describing the behavior of barium ion clouds once they have been produced is the height-integrated Pedersen conductivity given by

$$\Sigma_P = \frac{e^2}{m_{Ba}} \int \frac{\tau}{1 + (\Omega\tau)^2} n(z) dz \sim \frac{3.2 \times 10^{-11} \times \Omega\tau}{1 + (\Omega\tau)^2} N_\ell \text{ mho} \quad (25)$$

where N_ℓ is in cm^{-2} and $\Omega = eB/m_{Ba} = 35 \text{ s}^{-1}$ for a magnetic field of $1/2$ gauss. The variation of the cloud conductivity with altitude and payload is shown in Fig. 14. We shall make use of these estimates for the ion-cloud conductivity when we compare the theory of ion-cloud dynamics with data obtained during the Secede test series.

F. DISCUSSION

There are a number of effects whose variations have not been included in the above modeling and that have an influence on the properties of the ion cloud. These effects include the ambient neutral wind and

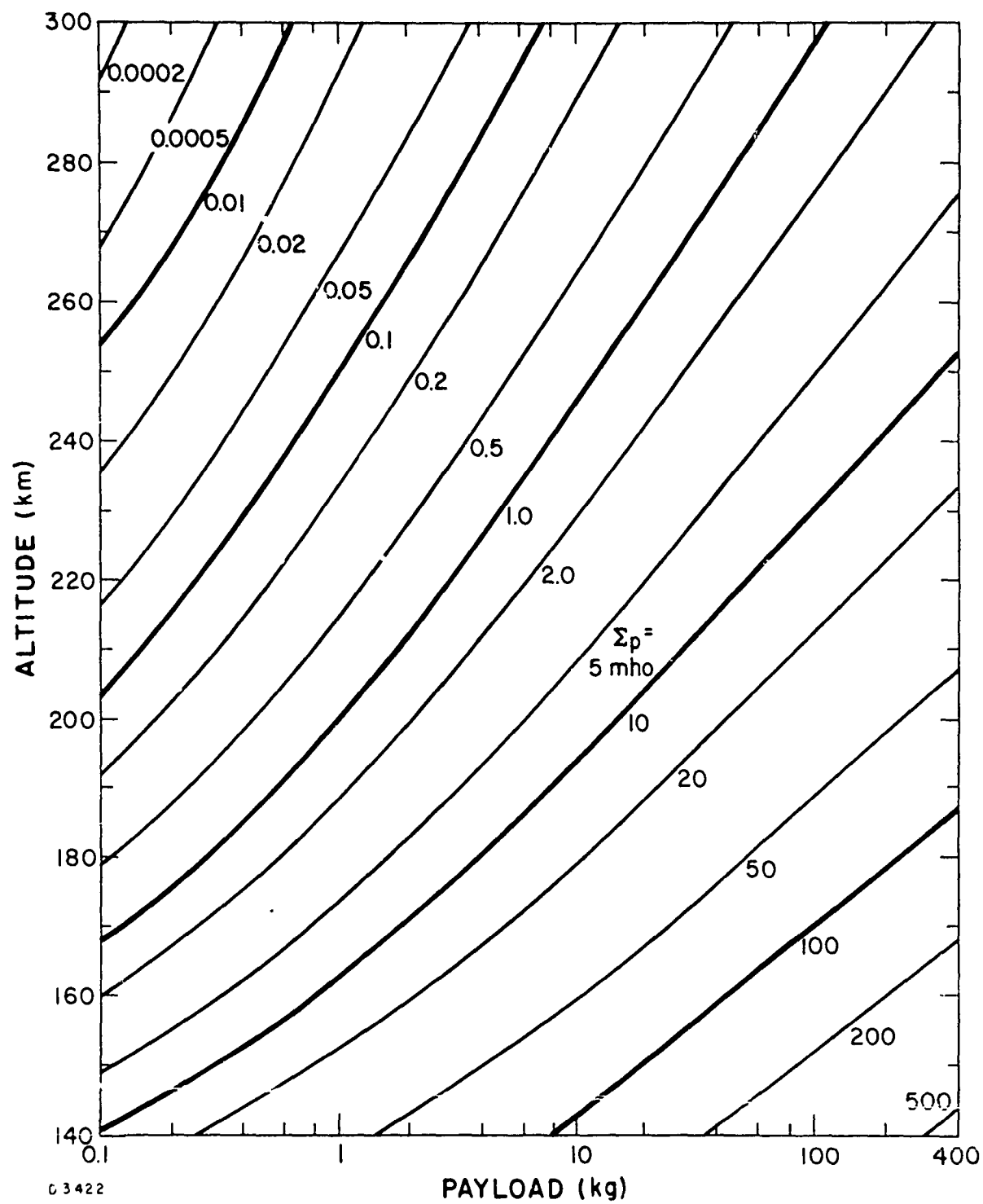


Fig. 14 The Height-Integrated Pedersen Conductivity for a Barium Ion Cloud as a Function of Altitude and Payload

electric field, the optical thickness of the neutral cloud, the cloud size and inventory, the latitude of the release, the time of day and the season of the year of the release, and the effects of barium cloud dynamics. We shall discuss each of these briefly, indicating the assumptions and limitations of the model and how it may be extended to include some of these effects.

The ions have been assumed to remain at rest after the barium atoms have been ionized. If there is a large wind of the ambient atmosphere at the altitude of the release, or if there is a large ambient ionospheric electric field, there will be a relative velocity between the neutral barium atoms which are being ionized and the barium ions thus created. Hence the ionization will be distributed over a larger area in the plane transverse to the magnetic field. As a result the electron density will be less than if no neutral wind existed as assumed in the model. For instance, a neutral wind of 100 m/s at an altitude of 190 km would displace the neutral cloud by 2.5 km during the 25-s ion-creation time appropriate to that altitude given by Eq. (12). A simple calculation indicates that the volume in which the ionization is now distributed has been increased by approximately 50%:

$$\text{Volume} \sim \frac{4\pi a_{\perp}^3}{3} \left[1 + \frac{3}{4} \frac{V_n t}{a_{\perp}} \right] \sim 1.5 \frac{4\pi a_{\perp}^3}{3}. \quad (26)$$

This effect probably accounts for the fact that the electron density in Event Plum I which had a large neutral wind present was approximately 2/3 that of the Spruce and Quince ion clouds. During Secede III the electron density of ion clouds released during high ambient neutral winds and electric fields was significantly reduced from the values given by this model.

We have not treated the influence that the thickness of the neutral cloud to the metastable-exciting solar radiation has on the production of ions in the ion cloud. Many of the barium atoms on the dark side of the neutral cloud should be shielded from this radiation until the excited atoms have been consumed by photoionization and oxidation. This effect should cause a lengthening in the time in which the bulk of the ionization is created. As a result, the electron density in the ion cloud should be somewhat less than that given by the model, since the neutral cloud would have diffused to a larger size and any ambient winds would have further displaced the neutral cloud. In spite of this influence, this model has been seen to give excellent agreement with observations of barium ion clouds. Perhaps the fact that we have assumed that the size of the ion cloud is determined by the size of the neutral cloud at two ionization time constants rather than one after an equal mass radius has been reached, has partially compensated for the optical depth effect. This effect should also cause a more non-uniform deposition of the ions in the ion cloud, which is probably of more importance for the initial condition to be assumed in developing the theory of barium ion clouds than it is here, in giving typical values for key parameters.

We note that in order for our modeling to give agreement with the radar data we have assumed a 30% vaporization efficiency for the production of barium atoms. This value is somewhat higher than the normally accepted 5% to 10% efficiency that has often been reported. However, Minkoff⁵ has reported vaporization efficiencies approaching 45% in the cases of Events Kumquat and Lime when the fraction of barium atoms lost to oxidation has been accounted for. The 30% figure is in agreement with the inventories

reported for Events Sapsucker and Titmouse.⁶ By using beacon data Prenatt⁷ has developed an ion-cloud model for Plum that corresponds to a 20% vaporization efficiency. In view of the excellent agreement that this model has produced with the optical and radar data we feel that this 30% figure is realistic for the chemical mixtures used during Secede II.

If the ion inventory had corresponded to a 5% to 10% vaporization efficiency, the size of the ion cloud transverse to the magnetic field would have to be smaller than the value given by a_{\perp} in Eq. (11) in order that the electron densities remain as high as reported by radar. A minimum possible size that might be considered reasonable is

$$a_m = (a_0^2 + 4D_n t_i)^{1/2} \quad (27)$$

corresponding t , the size of the neutral cloud at one ionization time constant after the vapor has reached an equal-mass radius. This size was found to be between 0.6 and 0.7 times a_{\perp} given by Eq. (11) throughout the altitude and payload range covered by the model. Hence there is a possibility that an 8% vaporization efficiency could be assumed if the transverse scale size for the Spruce ion cloud was 2.5 km instead of 3.75 km. We note that Prenatt⁷ has estimated a gaussian radius of 2.8 km for Event Plum I, and the incoherent backscatter radar results⁸ at early times in Event Spruce indicate a gaussian radius of 2.5 km transverse to the magnetic field. It should be noted that the same experiment reports an effective initial gaussian length of 4.3 km parallel to the magnetic field. At 22 seconds after release, these two sizes should have been equal. However, it is not likely that the Spruce ion cloud was gaussian-shaped at that time due to optical thickness effects. These small values for the transverse scale size of the

ion cloud appear to conflict with the optical data. It is fair to suggest that the scale size of the ion cloud transverse to the magnetic field and the total ion inventory are somewhat unresolved questions. In spite of this uncertainty it appears that the electron densities produced by the above model are in excellent agreement with the data.

The modeling that has been done has tacitly assumed midlatitude locations with magnetic dip angles larger than 45° but southward of the auroral zone. One parameter that changes as a function of altitude is the downward drift due to gravity as given in Eq. (23). Above 200 km, this drift is significant for large barium ion clouds. The latitude of the release will also have an effect on the limiting value of the density n_A that is reached by the ion cloud. In particular the value given by Eq. (21) should be decreased by the factor $\sin \theta_d$, since the ion cloud can diffuse parallel to the magnetic field for a longer time before it has diffused a scale height in altitude. As far as high latitude is concerned, it should be noted that this model should be applied with caution due to the large neutral winds and ambient electric fields that can exist in and near the auroral zone and to the large temporal and spatial variability of both of these parameters.

Linson⁹ has shown that the conductivity of the conjugate ionosphere in the southern hemisphere influences the motion, distortion, and striation characteristics of barium ion clouds. Although the conductivity of the local ionosphere will be more typical of nighttime values than of daytime values, the conductivity of the conjugate ionosphere can depend on both the time of day (i. e., whether it is a morning or evening twilight release) and the season of the year. Hence the behavior of barium ion clouds does depend on whether the conjugate ionosphere is in sunlight or in darkness. For instance,

during the morning releases of Secede I in May, the conjugate ionosphere was in darkness while during the evening releases of Secede II in January, the conjugate ionosphere was in sunlight. Hence in planning future tests both the time of day and the season of the year need to be considered if one is attempting to make predictions of the motion of barium ion clouds or the onset time for the formation of striations.

The modeling described in this section has not included any of the dynamics of barium ion clouds that are discussed in Chapter 5 that summarizes the relevant theory. In particular the motion, distortion, and striation behavior of barium ion clouds depends on the ratio of the ion-cloud height-integrated Pedersen conductivity to the height-integrated Pedersen conductivity of the ionosphere in both hemispheres. In order to model these plasma effects the conductivity of the ion cloud can be estimated with the aid of Fig. 14. Once this value is known, an estimate can be made of the expected ionospheric conductivity. It is important to remember to include the contribution to this conductivity from the ionospheres in both hemispheres. In particular, near the magnetic equator the magnetic field lines on which the ion clouds are created never leave the ionosphere and an accurate estimate carried out over the entire length of the field line must be made. Once the value of this ratio of conductivities is known, then an estimate can be made for the motion of barium ion clouds.⁹

Once barium ion clouds have striated so that very small scale lengths perpendicular to the magnetic field have been formed, then diffusion perpendicular to the magnetic field, which has been neglected in the above modeling due to the large scale sizes involved, becomes

important and is the mechanism by which the ionization is eventually dissipated. The time scale for this dissipation is also discussed in Chapter 5 describing the theoretical results.

REFERENCES

1. J. H. Mitchell and K. E. W. Ridler, "The Speed of Positive Ions in Nitrogen," Proc. Roy. Soc., (London) A146, 911, 1934.
2. R. H. Wand, "Electron to Ion Temperature Ratio from Radar Thomson Scatter Observations," J. Geophys. Res., 75, 829-838, 1970.
3. J. R. Bannister and H. L. Davis, "Descent of Particles and Molecules Through the Upper Atmosphere," Phys. Fluids, 5, 136, 1962.
4. B. Rao Pendyalo, "A Comparison Between Thomson Scatter Radar Observations and a Diffusion Model," in Proceedings of the SECEDe II Final Data Review Meeting, RADC TR-72-153, Volume II, pp. 129-141, SRI, Menlo Park, Calif. (May 1972).
5. J. B. Minkoff, ed., "Report on PRESECEDE Experiments," Report TR-27/068-4-00, Riverside Research Institute (March 1970).
6. J. H. M. Fu, E. P. Marronn, T. B. Ponder, J. R. Breddlove, "Photographic Data Reduction Report on Birdseed I Barium Releases," EGG 1183-5003, EG & G, (August 1971).
7. R. E. Prenatt, "A Preliminary Model for the Electron Concentration in the Early Plum Ion Cloud," in Proceedings of the SECEDe II Final Data Review Meeting, RADC TR-72-153, Vol. II, Stan. Res. Inst. (May 1972), p. 285.
8. R. T. Tsunoda, "Incoherent-Scatter Results for Event Spruce," in Proceedings of the SECEDe II Final Data Review Meeting, RADC TR-72-153, Vol. II, Stan. Res. Inst. (May 1972), p. 111.
9. L. M. Linson, "Motion of Barium Ion Clouds", in Analysis of Barium Ion Clouds, RADC TR-72-103, Vol. I, Avco Everett Research Laboratory. (January 1972) p. 39. See also Chapter 5 of this report.

CHAPTER 2
PARTIAL REDISTRIBUTION IN RADIATION TRANSPORT

2. PARTIAL REDISTRIBUTION IN RADIATION TRANSPORT

B. Kivel

A. INTRODUCTION

Artificial clouds produced by chemical releases in the upper atmosphere are of current interest.^{1,2} The clouds are produced at twilight so that they may be observed in the scattered sunlight while the sky is dark. Photographic information allows determination of cloud position and spatial extent. It is also possible to estimate the column densities of the scattering material using calibrated intensity data. However, because of optical depth effects, the relation between the intensity and the amount of material is not linear. The purpose of this paper is to assist in understanding the relation between column density and scattered intensity using simple models.

We consider the problem of scattering by a slab of atoms with only one resonant transition that scatters isotropically. Of primary interest is the effect of the partial redistribution of radiation energy which is caused by the Doppler effect. Collisions are neglected, which is reasonable for the high altitudes of interest. For simplicity the effect of polarization will also be omitted. We approach the problem using two models. The first is an analytic treatment which does not allow for redistribution of photon energy in the scattering event and the second is a Monte Carlo calculation which allows for the correct redistribution caused by the Doppler effect.

In many radiation transport problems, especially where collisions dominate, it is customary to use complete redistribution.^{3,4} No redistribution is also used, in particular it has been used in analysis of the atmospheric sodium in the airglow.⁵ The importance of redistribution is that it

allows photons which start near the center of the line and have a small mean free path to change in energy to regions where the mean-free-path is longer and it is easier to escape the cloud. An analytic solution taking into account the effect of partial redistribution has been used for the interpretation of spectra from an optically thick nebula.⁶ Comparison of the Monte Carlo with the analytic results for no redistribution allows one to estimate the importance of the redistribution effect in the upper atmosphere scattering produced by artificial clouds.

In Section B we give the analytic solution for diffusion of monochromatic energy photons with constant mean-free-path through a one-dimensional slab. This solution is well known and hence forms the basis for testing the Monte Carlo results. In Section C we give the physical basis and in Section D the mathematical details, for the Monte Carlo calculations. Section E contains a comparison of the results for both methods and, in particular, compares the reflection and transmission coefficients. A discussion of the results is given in Section F.

B. ANALYTIC MODEL

In this section the problem of resonant isotropic scattering neglecting the effect of polarization by scattering atoms with a Maxwell-Boltzmann distribution of velocities in a one-dimensional slab is treated. We solve the one-dimension diffusion differential equation. This is a well known elementary problem and a basic discussion of it may be found in standard texts such as Morse and Feshbach.⁷

We treat the problem of an incident flux normal to one face of the cloud and vary the photon energy and slab thickness. Our primary interest will be in regions in which the cloud is optically thick since the optically thin solution which relates intensity linearly to the number of scatterers is trivial. It will be seen from the results that in the optically thick regions the radiation is essentially reflected from the illuminated face. However, in the line wings as the cloud becomes less thick a fraction of the light is diffusely transmitted through the slab. In the still less thick regions a part is transmitted without scatter and of the fraction which is scattered, about half is reflected and half transmitted.

We start with a one dimensional diffusion equation for the radiation flux (J_ν) at frequency ν ; i. e.,

$$J_\nu = - \frac{c\lambda}{3} \frac{\partial \rho_\nu}{\partial \xi} \quad (1)$$

where c is the velocity of light

λ is the mean-free-path at frequency ν

ξ is the distance normal to the plane parallel faces
of the slab

ρ_ν is the photon density at frequency ν

The incident solar flux is treated as a source at the location of the first scattering and for the solar flux normal to the face of the slab we have

$$\frac{\partial J_\nu}{\partial \xi} = \frac{I_\nu e^{-\xi/\lambda}}{\lambda} \quad (2)$$

where I_ν is the solar flux at frequency ν . Combining Eqs. (1) and (2) and introducing $z \equiv \frac{\xi}{\lambda}$ we have

$$\frac{\partial^2 \rho}{\partial z^2} = - \frac{3}{c} I e^{-z} \quad (3)$$

The boundary conditions are

$$\rho_o = 0.7 \left(\frac{\partial \rho}{\partial z} \right)_o \quad (4)$$

where the subscript o stands for the solar illuminated side of the cloud,
and

$$\rho_\tau = -0.7 \left(\frac{\partial \rho}{\partial z} \right)_\tau \quad (5)$$

where the subscript τ stands for the values on the dark side of the slab
of optical depth τ normal to the plane face of the cloud. These boundary
conditions are derived approximately in Morse and Feshbach. They are
required to give an average of zero for the diffusing flux from outside into
the slab. The result is justified by more rigorous solutions of the corres-
ponding integral equation

The solution of the differential equation (Eq. (3)), is

$$\rho_\nu = -\frac{3}{c} I_\nu e^{-z} + a z + b \quad (6)$$

where the two unknown constants a and b are fixed by the boundary conditions (Eqs. (4) and (5)). In this way we find

$$a = -\frac{3I_\nu}{c} \left(\frac{1.7 - 0.3 e^{-\tau}}{1.4 + \tau} \right) \quad (7)$$

and

$$b = 1.7 \left(\frac{3I_\nu}{c} \right) + 0.7 a \quad (8)$$

As an example consider the case with $\tau = 2.3$. A plot of the diffusing radiation density ρ normalized by the solar flux I_ν , divided by the velocity of light ($\rho / (I_\nu/c)$) as a function of distance in the slab ξ normalized by the radiation mean-free-path λ is shown in Fig. 1. The density peaks at a distance close to optical depth of 1 ($\xi \approx \lambda$). There is more radiation on the solar illuminated side ($\xi = 0$) than on the dark side ($\xi = 2.3\lambda$). Also the gradient of density is larger on the solar illuminated side and this implies more radiation is re-emitted from the solar side than from the back. The figure also indicates that the boundary conditions are satisfied, since the curve of ρ extrapolates to zero at a distance $\Delta\xi = 0.7\lambda$ from the boundary (i. e., at $\xi = 3.0\lambda$ and at $\xi = -0.7\lambda$).

At higher τ the values of $R \equiv \rho/(I/c)$ are larger for the same z and the peak occurs at larger z . For example, at $\tau = 4.6$ at $z = 0$, $R = 1.5$; the maximum occurs at $z = \ln_e(-3I/ca)$, i. e., at $z = 1.28$ with $R = 2.6$. On the other hand the value of R at the back face is lower;

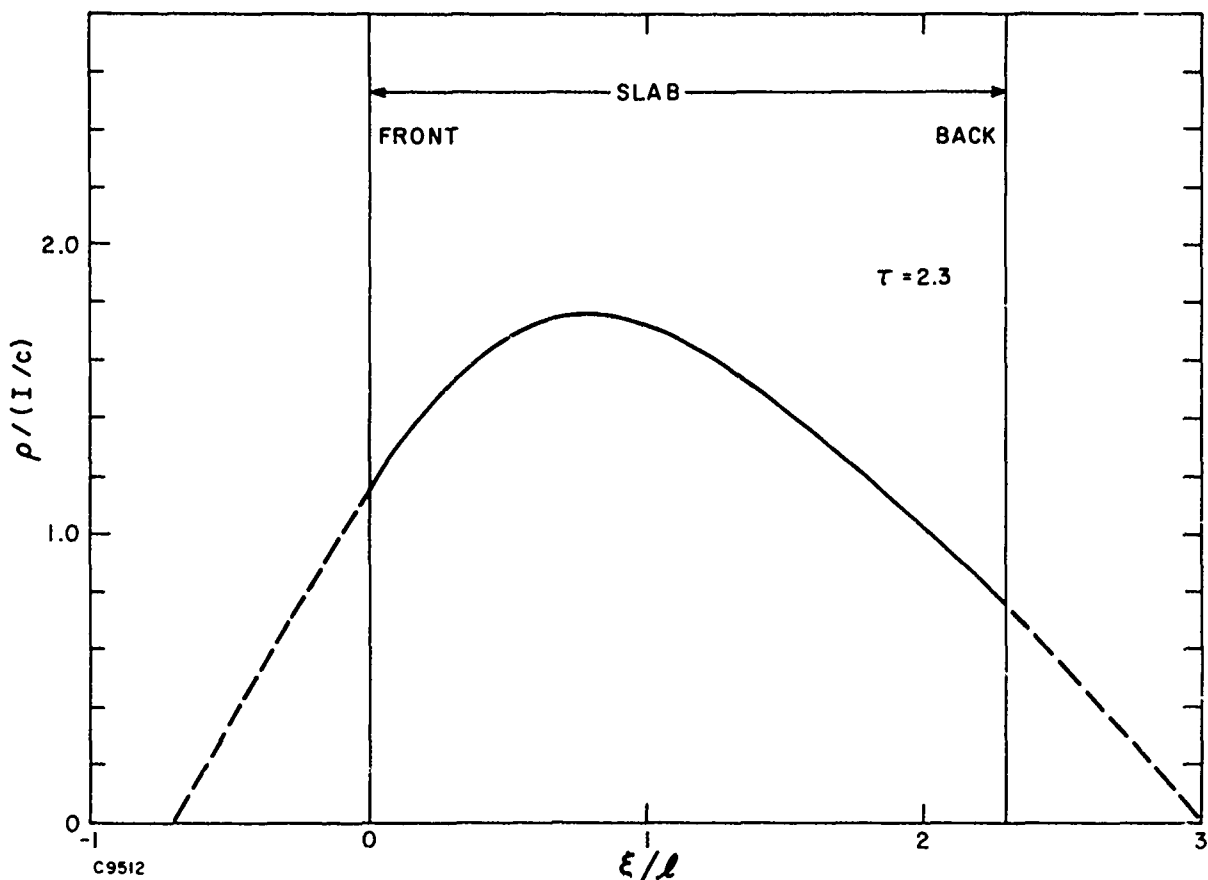


Fig. 1 Diffusion solution in a slab of optical depth $\tau = 2.3$. This figure illustrates that the radiation density peaks near optical depth of about 1 and that the gradient of density at each boundary extrapolates to 0 at 0.7 of a mean-free-path away from the slab.

i. e., at $z = 4.6$ $R = 0.58$. These differences provide the basis for the larger reflection coefficient for the slab of higher optical depth.

We can now express the emitted radiation resulting from diffusion outward which is in proportion to the gradient of the radiation density at the boundary (see Eq.(1)). However, because of the boundary conditions (Eqs. (4) and (5)) the re-emission is in proportion to the density of radiation at the boundary. Taking account of the fact that $e^{-\tau}$ of the incident light is transmitted without scattering we have

$$I_o = I_v (1 - e^{-\tau}) \frac{\rho_o}{\rho_o + \rho_\tau} \quad (9)$$

and

$$I_\tau = I_v (1 - e^{-\tau}) \frac{\rho_\tau}{\rho_o + \rho_\tau} \quad (10)$$

where, as before, the subscript o stands for solar illuminated side and τ for the opposite side. For $\tau = 2.3$, illustrated in Fig. 1, we have $I_o/I_v \approx 0.55$ and $I_\tau/I_v \approx 0.35$ and the remaining 10% of the incident flux is transmitted unscattered.

We can now express the intensities of re-emission analytically as a function of τ . Defining relative intensities for reflected (i_R) and transmitted (i_T) components, we have

$$i_R \equiv \frac{I_o}{I_v} = 1 - a \quad (11)$$

and

$$i_T \equiv \frac{I_\tau}{I_v} = a - e^{-\tau} \quad (12)$$

where (compare Eq. (7))

$$a \equiv \frac{1.7 - 0.3 e^{-\tau}}{1.4 + \tau} \quad (13)$$

From Eqs. (11) and (12) we obtain $i_R + i_T = 1 - e^{-\tau}$ so that the total re-emitted light is equal to the total scattered light and energy is conserved. In the limit of very small optical depth ($\tau \rightarrow 0$) we have $i_R = i_T = \tau/2$ which is the expected result for a thin slab. Here the amount of light scattered is in proportion to the amount of material and for isotropic re-radiation $1/2$ of the light comes out of each face of the slab. In the limit of large optical depth ($\tau \rightarrow \infty$) we have $i_R \rightarrow 1$ and $i_T \rightarrow 0$ so that, again as expected for a semi-infinite non-absorbing scattering medium, all of the light is reradiated from the illuminated face.

These results can now be applied to a scattering medium with a single scattering line with Gaussian profile. In Fig. 2 we give the relative intensity (or line profile) for an incident flux independent of frequency, as a function of frequency normalized to the Doppler half-width for an optical depth at the line center of 100. The optical depth as a function of wavelength is

$$\tau = 100 e^{-x^2} \quad (14)$$

where

$$x \equiv \Delta v / \Delta v_D$$

the ratio of the frequency from the line center (Δv) to the Doppler half width (Δv_D). The curve in Fig. 2 labeled FRONT corresponds to i_R and BACK to i_T . In this case, the light reflected from the solar illuminated face is about 5 times larger than that scattered from the dark side. The radiation from the back face comes mainly from regions in the line wings where the optical depth is about 2. In the far wings where the scattering slab is optically thin the intensities are the same front and back.

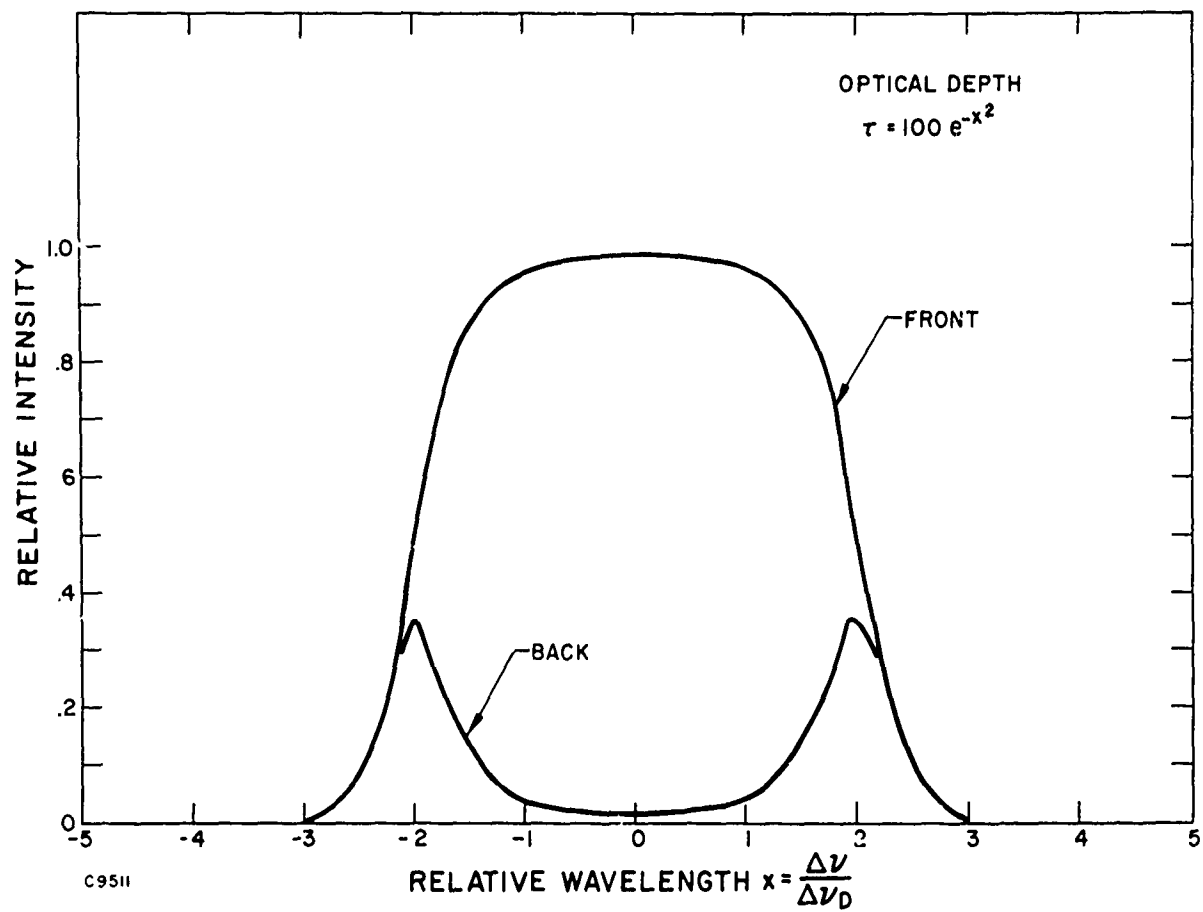


Fig. 2 Spectral line profile as seen from the illuminated face (front) and the opposite (back) for a slab of scatterers with a Gaussian profile and an optical depth of 100 at the line center.

At the line center all light is reradiated from the front and the total intensity scattered from the front is determined by the effective line width (i. e. , the wavelength region where $\tau \sim 1$).

We have assumed throughout that there is no redistribution of radiation in wavelength because of the absence of collisions. This assumption is not true because of the Doppler effect, where the recoiling atom may gain or lose energy at the expense of the photon. The importance of this effect is explored in the following sections using Monte Carlo calculations.

C. PHYSICAL BASIS FOR MONTE CARLO CALCULATION

The problem to be solved is the scattering of radiation by a slab of low density gas with only one transition and no line broadening except the Doppler effect.

Each scattering event is incoherent because there is a large phase change as a result of the scattering.⁸ Even radiation, which deviates from the transition energy of an atom at rest by an amount large compared to the Doppler width, is in resonance since the difference in energy is compensated for by a change in the atom's kinetic energy. As a result we can 1) treat the scattered light as being emitted isotropically from the scattering atom, and 2) neglect the interference effects of the several scattering centers.

The correct problem allows the photon to diffuse, both in space and energy. The photon can be absorbed only by those atoms that have the specific projected velocity along the photon direction required by the Doppler effect. The velocity of the atom, of course, can be appreciably larger since it is only the projected component that is fixed. The re-emitted photon can be shifted to the red or the blue independent of the initial incident photon energy and depending only on the total velocity of the scattering atom and the direction of emission relative to the atom's velocity vector. We assume that the reradiation is isotropic and pick the emission direction at random and independent of the velocity of the scattering atom. The energy of the emitted photon is determined by the Doppler effect, using

the projected velocity of the scatterer on the direction of emission. The mean-free-path of the emitted radiation is determined by the photon energy. For a Maxwell-Boltzmann velocity distribution the mean-free-path has a Gaussian dependence on energy. Since the number of scatterers is proportional to $\exp - (v_{||}^2 M / 2kT)$, where $v_{||}$ is the component along the direction of the photon flight path and the Doppler shift is given by the relation $\Delta \tilde{\nu} = v_{||} \tilde{\nu} / c$.

Because we are interested in a uniform slab which is infinite in area we are not concerned with the motion of the photons parallel to the face of the slab. It is only necessary to calculate the projected motion normal to the face. This calculation is done by using the polar angle between the photon direction and the direction normal to the face. The length of motion between scattering is determined at random assuming an exponential attenuation with distance and a mean-free-path determined by the atomic cross section and the Maxwell-Boltzmann distribution of scatterers. The projected length of the distance between scattering events is used to determine the successive positions relative to the face of the cloud. The photon is tracked from initial entrance until it emerges from either face of the slab. If the photon reemerges from the face it entered, then it is reflected. Reemergence from the rear face after scattering is diffuse transmission. It is also possible, even in optically thick cases, that a photon traverses the cloud without scattering; we call this unscattered transmission.

D. MATHEMATICAL DETAILS OF MONTE CARLO METHOD

There are three variables which determine the photon state; 1) its location in the slab, given by the normal distance z , which goes from 0 at the face of initial incidence, to a variable upper limit Δz ; 2) the polar angle, Θ , fixing the direction of motion with respect to the z axis; and 3) the photon energy, given by the non-dimensional ratio, x , of the deviation from the line center divided by the Doppler half-width, $\Delta \tilde{\nu}_D \equiv \tilde{\nu} v_0 / c$, where $\tilde{\nu}$ is the wave number value for the transition, $v_0 = \sqrt{2kT/M}$ a nominal particle speed at temperature T , for mass M , with $c = 3 \times 10^{10}$ cm/s and $k = 1.38 \times 10^{-16}$ erg/ $^{\circ}$ K. A typical set of initial conditions for these parameters are $x_0 = 0$; i.e., at the line center, $\Theta_0 = 0$, incident normal to the face, and $z_0 = 0$, at the incident face of the scattering region.

The mean-free-path for a Maxwell-Boltzmann distribution of particle speeds is $\lambda = e^{x^2} / (nQ)$ where n is the particle density and Q is the peak Doppler cross section

$$Q = \sqrt{\pi} r_e f / \Delta \tilde{\nu}_D \quad (15)$$

where

$$r_e = 2.8 \times 10^{-13} \text{ cm}$$

f = transition number

$$\Delta \tilde{\nu}_D = v_0 \tilde{\nu} / c$$

For Ba ion clouds at $\lambda = 4934\text{A}$, $T = 900^\circ\text{K}$ and $f = 0.35$, $Q \approx 10^{-11}\text{cm}^2$.

For $n = 3 \times 10^6 \text{ cm}^{-3}$, $1/nQ \approx 1/3 \text{ km}$. For simplicity and generality we have normalized the distance scale z by dividing by the mean-free-path at the center of the scattering line $1/nQ$. The probability of going a distance s and being scattered in an interval ds is $dp = e^{-s} ds$. We determine s by picking p at random from a uniform distribution between 0 and 1 and setting $s = \ln_e(1/p)$. In this way s covers the range from 0 to ∞ and has a probability of occurrence in proportion to e^{-s} .

The distance the photon moves perpendicular to the slab face is then determined for s, x and the polar angle according to $\Delta z = se^x \cos \theta$. The photon goes forward for $\theta < 90^\circ$. The distance moved is longer in the line wings, increasing as e^x .

The velocity vector of the scattering atom is determined so that the component ($v_{||}$) in the direction of the incident photon is given by the Doppler effect; i.e., $v_{||} = c \Delta \tilde{v}/\tilde{v} = v_0 x$. The perpendicular component (v_{\perp}) is picked at random consistent with a Maxwell-Boltzmann distribution; defining $u = v_{\perp}^2/v_0^2$ we set $u = \ln_e(1/p)$ where p is a random number from a uniform distribution between 0 and 1. The polar angle between the initial photon direction and the velocity vector is then $\psi = \tan^{-1} \frac{\sqrt{u}}{x}$ for positive x , and $\psi = 180^\circ - \tan^{-1} \frac{\sqrt{u}}{x}$ for negative x . The azimuthal angle of the velocity vector around the direction of the incident photon is ϕ , picked at random between 0 and 360° ($\phi = 360 p$ where p is uniform random 0 to 1).

We will need the polar angle of the velocity vector with respect to the z axis, θ . This is determined by the law of cosines in spherical trigonometry

$$\cos \theta = \cos \psi \cos \Theta + \sin \psi \sin \Theta \cos \phi. \quad (16)$$

The angle of emission is taken as isotropic. We define the polar angle with respect to the velocity vector as $\bar{\Theta}$ and the azimuthal angle as ϕ . The element of solid angle is $\sin \bar{\Theta} d\bar{\Theta} d\bar{\phi} = d\mu d\phi$ where $\mu \equiv \cos \bar{\Theta}$. We pick μ at random between +1 and -1 and ϕ between 0 and 360° ($\mu = 2p-1$ and $\phi = 360p$ and p is uniform random 0 to 1).

The Doppler shift of the emitted photon is determined by the velocity component along the direction of emission. The shift is given by the product of the scattering atoms velocity $\sqrt{u + x^2}$ and $\cos \bar{\Theta}$.

The polar angle of the emitted photon with respect to the z axis (Θ) is determined by the law of cosines;

$$\cos \Theta = \cos \bar{\Theta} \cos \theta + \sin \bar{\Theta} \sin \theta \cos \phi. \quad (17)$$

With the values for x and Θ the distance to the next scattering event is calculated as described above. The photon is followed in this way until it emerges from either the front or rear face of the slab.

E. RESULTS

Calculations have been made for eleven incident photon energies $x_0 = 0, \pm 0.5, \pm 1, \pm 1.5, \pm 2$ and ± 2.5 . All cases are for a normal angle of incidence, $\Theta_0 = 0$, and all start at $z_0 = 0$. We have followed the trajectories of 100 photons for each of these cases. The calculation was done on an IBM-360 series 145 using FORTRAN IV and OSMFT; the 1100 cases took less than 10 minutes of computing time. The results are analyzed to give the fraction of photons reflected and transmitted. The dependence on the initial energy of incidence and on the slab thickness is reported in this section. The energy spectrum of the reflected photons is given for a uniform spectral flux of incident photons. We also correlate the angular dependence of the reflected photons.

Comparison of the Monte Carlo calculations for reflection and diffuse transmission with the diffusion solution without redistribution for depth $\Delta = 100$ as a function of x are shown in Fig. 3. For $x \lesssim 1$ the optical depth is $\tilde{\tau} > 30$ and 95% or more of the incident light is reflected according to both methods of calculation. At $x = 1.5$, $\tau \equiv \Delta e^{-\tilde{\tau}} \approx 10$ and according to both methods the reflected part has dropped to about 85%, the rest being transmitted. At $x = 2$, $\tau \approx 2$, about 20% is transmitted unscattered and of the rest 50% is reflected and 30% diffuse transmitted according to Monte Carlo. Here both reflection and transmission differ from the analytic solution; Monte Carlo gives slightly more reflection and less transmission. At $x \gtrsim 2.5$ more than 80% is unscattered and the scattered radiation is approximately half reflected and half scattered.

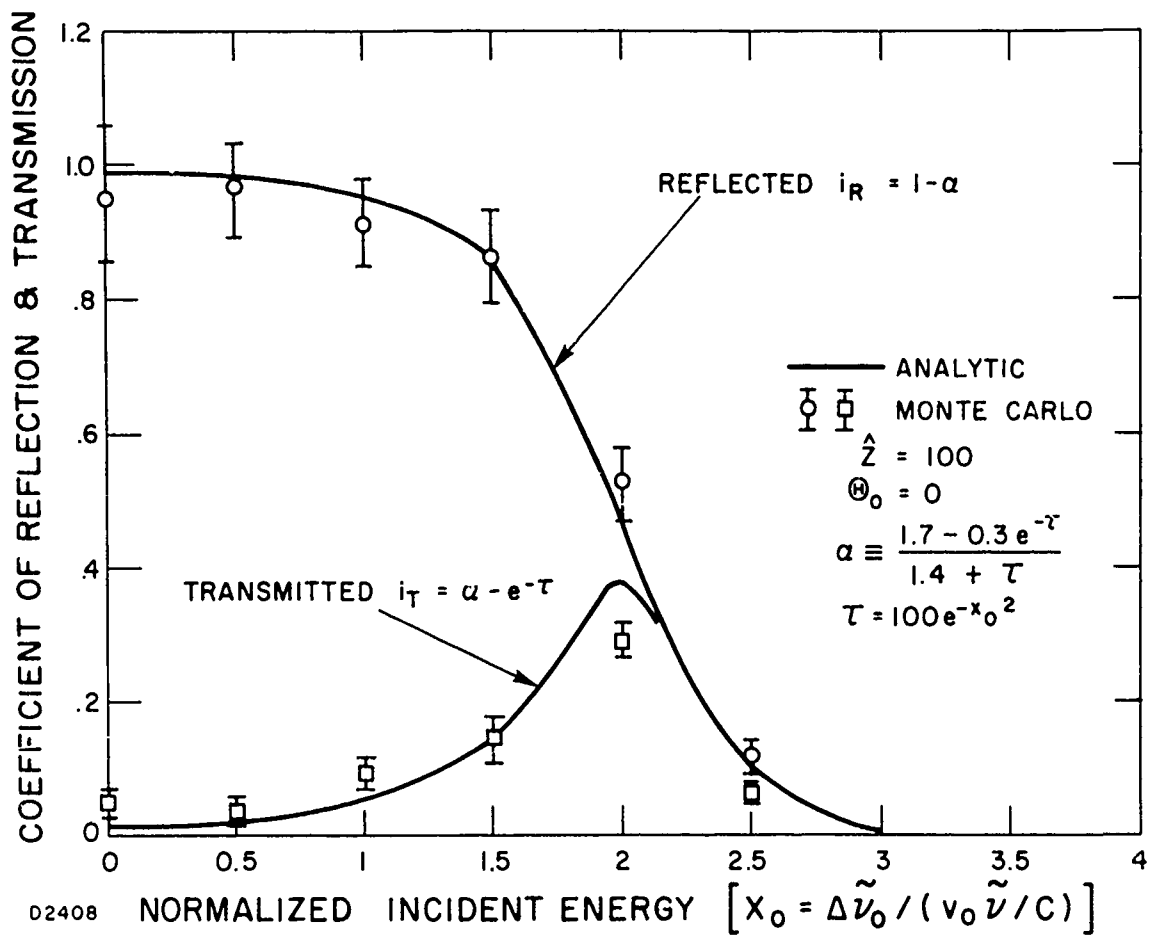


Fig. 3 Coefficients of reflection and transmission as a function of the normalized incident energy. The solid lines are the analytic solutions without redistribution. The data symbols are obtained by the Monte Carlo method with the correct redistribution. The results are for an optical depth $\hat{Z} = 100$ and an incident flux normal to the face of the scattering slab ($\Theta_0 = 0$). The reflection coefficient is close to 1 at the line center, drops to about 1/2 at twice the Doppler half width where the optical depth is about 2 and the transmission coefficient peaks in the region where the optical depth is about 2.

In conclusion, Doppler redistribution does not allow significant transmission where there is large optical depth. Where the optical depth is about 2 in the line wing, the Doppler redistribution estimated from the Monte Carlo result implies somewhat less transmission (not more) than given by the analytic method. However, the total reflection for a uniform input spectrum is close to 70% in both cases. The total reflected intensity increases with increasing scattering material because the increasing optical depth leads to a larger spectral range where the optical depth exceeds 2; i. e., the effective line width increases with an increase in the column density of scattering atoms in the slab.

1. Dependence on Slab Thickness

Information has also been obtained on the effect of slab thickness. The results are shown in Fig. 4. The analytic results for the relative intensity as a function of the cloud thickness in terms of the mean-free-path at the line center is shown by the solid lines. Monte Carlo calculations for finite slab thicknesses were also carried out and the results are shown by the data symbols. Within the statistical uncertainty of the finite samples the Monte Carlo results agree with the analytic method which has no redistribution of photon energy as a result of scattering. These results are for an incident of photon with energy at the Doppler half width, i. e., $x_0 = 1$. Thus we again find that the Monte Carlo calculation agrees with the method that neglects the effect of redistribution.

The transmitted component peaks where the optical depth is about 2; i. e., $\tau \equiv \sum e^{-x^2} \approx 6 e^{-1}$. This is consistent with the result in Fig. 3. As a result the total amount of light diffusely transmitted is not sensitive

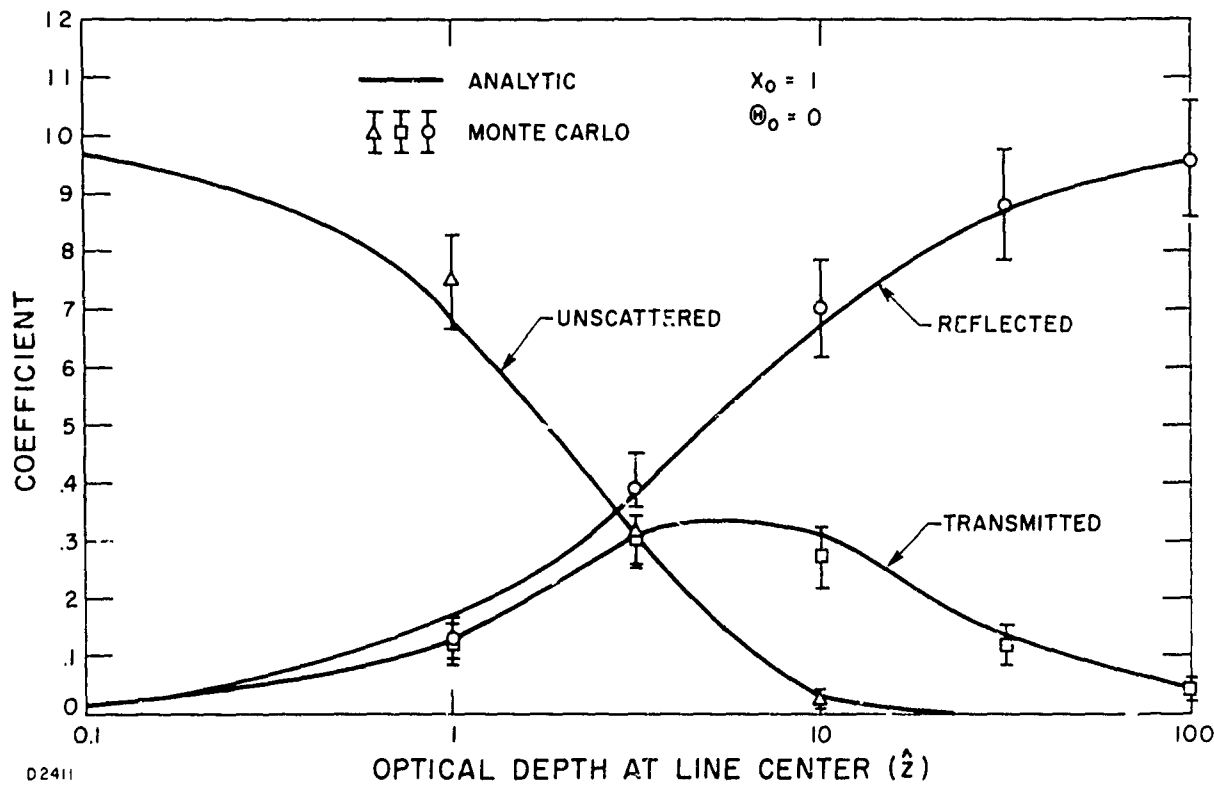


Fig. 4 Coefficients of diffuse reflection and transmission and unscattered transmission for a slab as a function of the optical depth at the line center. The incident light has an initial energy at the Doppler half width ($x_0 = 1$) and starts at normal incidence to the face of the slab ($\Theta_0 = 0$). The analytic results are given by the solid lines and the Monte Carlo results by the data symbols. The values at $\hat{z} = 100$ are the same as those in Fig. 3.

to the optical depth and hence insensitive to the amount of scattering material. Of course, the spectral separation of the bands increases with increasing optical depth.

2. Reflected Spectrum

The final energy (x) of the reflected photons has been recorded and it is possible to estimate the spectral profile for a uniform incident spectral flux. For the uniform incident spectrum the emitted line is symmetric about the central frequency. However, it should be noted that the spectrum depends on the distribution of the incident flux. Photons near the line center are emitted with the profile approximately like that given by the uniform distribution, while photons incident at the line wings are reradiated in the wings where comparable amounts of red and blue photons emerge. The distribution for emerging photons gives slightly more reradiation on that side of the line center at which the incident flux started. The difference, however, is not statistically proven by the limited number of calculations carried out in this study. For example, taking all positive photons incident (i. e., $x_0 = +0.5$ to $+2.5$) the difference between the final $x > 0$ and $x < 0$ is less than 5% of the total number of events. A similar result occurs for the incident negative energy cases ($x_0 < 0$).

The total number of events are equally divided between final x values greater than and less than 0. As a result we summarize the results using the absolute value of x . The final energies are divided into half integer regions of x space. The results are given in Table 1. The first column gives the final energy range of the reflected photons. The next column gives the fraction expected in the energy range. The third column

is the number of the 769 observed reflected photons expected to have the final energy in the given range and the last column is the number observed in the Monte Carlo results.

The curve of the expected spectrum given by the diffusion differential equation without redistribution is the same as that for the reflected component given in Fig. 3. This follows because no redistribution requires that the final energy equals the incident energy ($x = x_0$).

TABLE 1
REFLECTED SPECTRUM

x Range	Fraction Analytic	Analytic Number Expected	Monte Carlo Number Observed
0 - 0.5	.256	197	170
0.5 - 1.0	.252	194	183
1.0 - 1.5	.237	182	157
1.5 - 2.0	.175	135	164
2.0 - 2.5	.066	51	85
2.5 - 3.0	.012	9	10

The Monte Carlo results give 769 reflected photons from a uniform distribution of 1100 incident photons in the range $x_0 = -2.5$ to $+2.5$, that is, there are 70% reflected. A numerical integration of the analytic result shows that the reflection in the same range from $x_0 = 0$ to 2.75 is also approximately 70%. That both methods give the same average reflection is seen in Fig. 3 from the agreement between the analytic and Monte Carlo results. Because of this agreement we normalize the area of the Monte Carlo histogram for the emitted spectrum to the area under the analytic curve for the reflection coefficient in the region $x_0 = 0$ to 2.75. This normalization is accomplished

by dividing the number of events (N_x) in each half integer range of x by 202. Similarly, the estimated error bracket is given by $(N_x \pm \sqrt{N_x})/202$. The results are shown in Fig. 5. The solid line is the analytic result and the data symbols represent the Monte Carlo histogram. While the integrated energy reflected is the same in both cases, there is a slight redistribution of the energy. The Monte Carlo shows that because of partial redistribution less photons are reflected in the line center. Of course, our conclusions are limited to the case calculated where the optical depth at the line center is $z = 100$ and photons arrive at normal incidence, $\Theta_0 = 0$. The reduction is about 15% in the spectral range out to about 1.5 times the Doppler half width. The difference appears as an excess in the region between 1.5 and 2.5 times the Doppler half width. Qualitatively, the spectrum for both methods is described by strong intensity, comparable to the incident flux, in the neighborhood where the optical depth is 2 or greater and a rapid decrease in intensity occurs as the optical depth goes below the value 2.

3. Reflected Angular Distribution

The Monte Carlo results give an angular distribution for reflected photons which is consistent with Lambert's law. In our case the photon distribution $[I(\Theta) d\Theta]$ is in proportion to the product of the Lambert factor, $\cos \Theta$ and the solid angle factor $\sin \Theta d\Theta$. This product is proportional to $\sin 2\Theta$.

$$I(\Theta) d\Theta \propto \cos \Theta \sin \Theta d\Theta = \frac{1}{2} \sin 2\Theta d\Theta \quad (18)$$

For comparison we divide the Θ range into six 15° intervals. The expression $\sin 2\Theta$ is analytically integrated to give the fraction expected

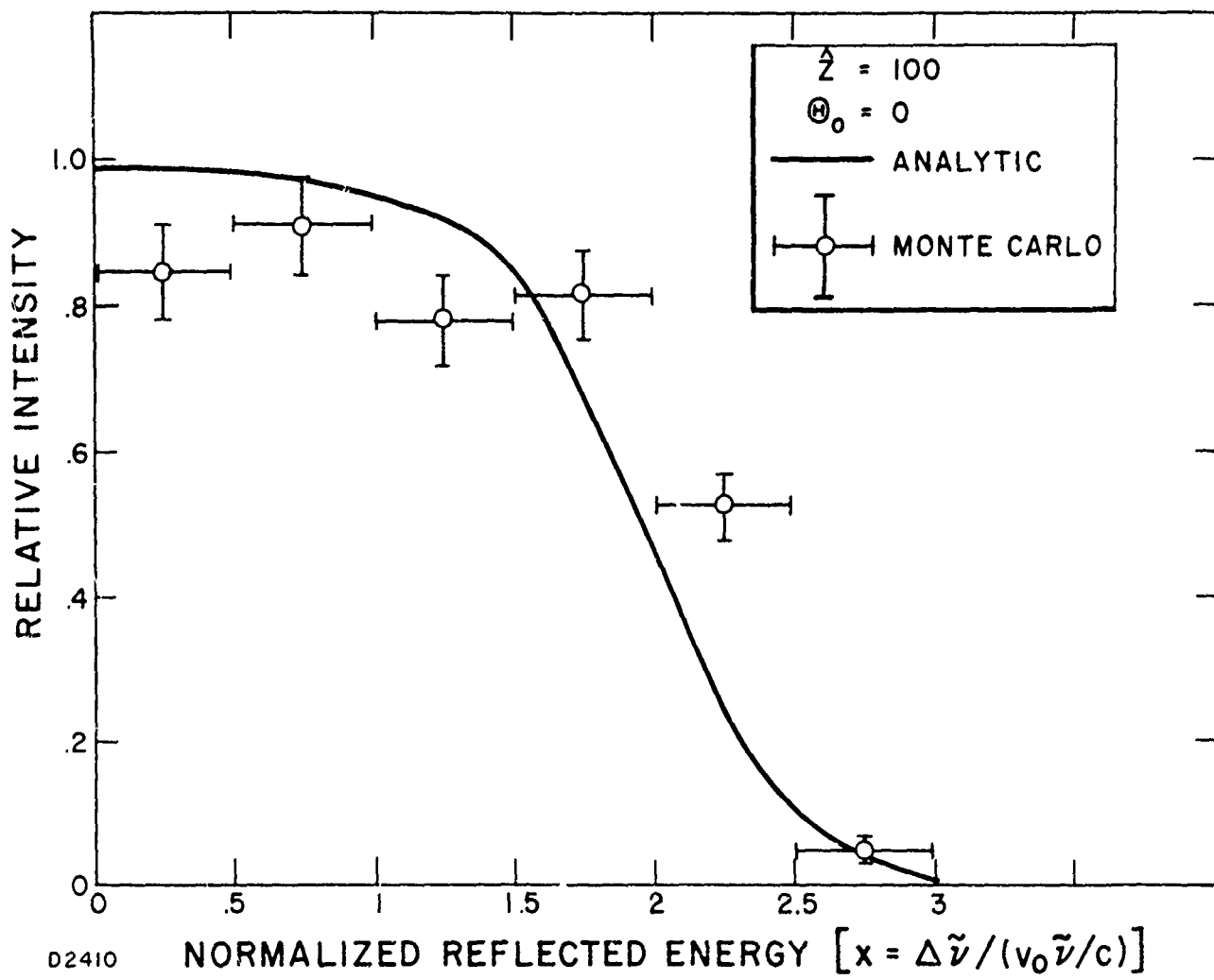


Fig. 5 The reflected spectrum for a uniform incident spectrum as a function of the final energy of the reflected photons. The solid line is the analytic solution and the data symbols give the Monte Carlo histogram. The total reflected energy is the same for the two cases. However, the Monte Carlo solution is between 10 and 20% lower at energies less than 1.5 times the Doppler half width and correspondingly higher in the region 1.5 to 2.5 times the Doppler half width.

in each interval. The results are given in Table 2. The first column gives the angular range, the second column the expected fraction for a Lambertian distribution, the third column is the number of reflected events expected for the 769 observed reflections, and the last column gives the actual number given by the Monte Carlo calculation. It is seen that the observed distribution is well within the uncertainty for the finite number of events.

In Fig. 6 we compare the results of the observed number of events (N_Θ) and the analytic curve for $\sin 2\theta$. The number of events is normalized by dividing by 201 which is the number of events (769) multiplied by the angular range in radians ($\pi/12$). The error bars are $\pm \sqrt{N_\Theta}/201$.

The distribution function for diffuse reflection neglecting redistribution is approximately $(4-6 \cos \theta)/7$ (see Ref. 7, p. 187 and also Ref. 9). Multiplying this distribution by $\sin \theta \cos \theta$ for the solid angle and projected area effect we obtain a distribution which is given in Table 2 labeled No Redistribution and which is inconsistent with the Monte Carlo results. The difference is attributed to the few scattering events for the incident light problem treated by Monte Carlo. About half of the reflected photons experience 10 or less scattering events and hence are approximately isotropic. In an example of 100 photons started at $z_0 = 50$, $x_0 = 0$, $\Theta_0 = 90^\circ$ for $\hat{\gamma} = 100$ the photons were emitted consistent with the non-Lambertian expression given at the start of this paragraph. In the central source problem about 1/2 of the photons experienced between 100 and 300 scattering events before emerging from the slab and hence diffusion is a reasonable description.

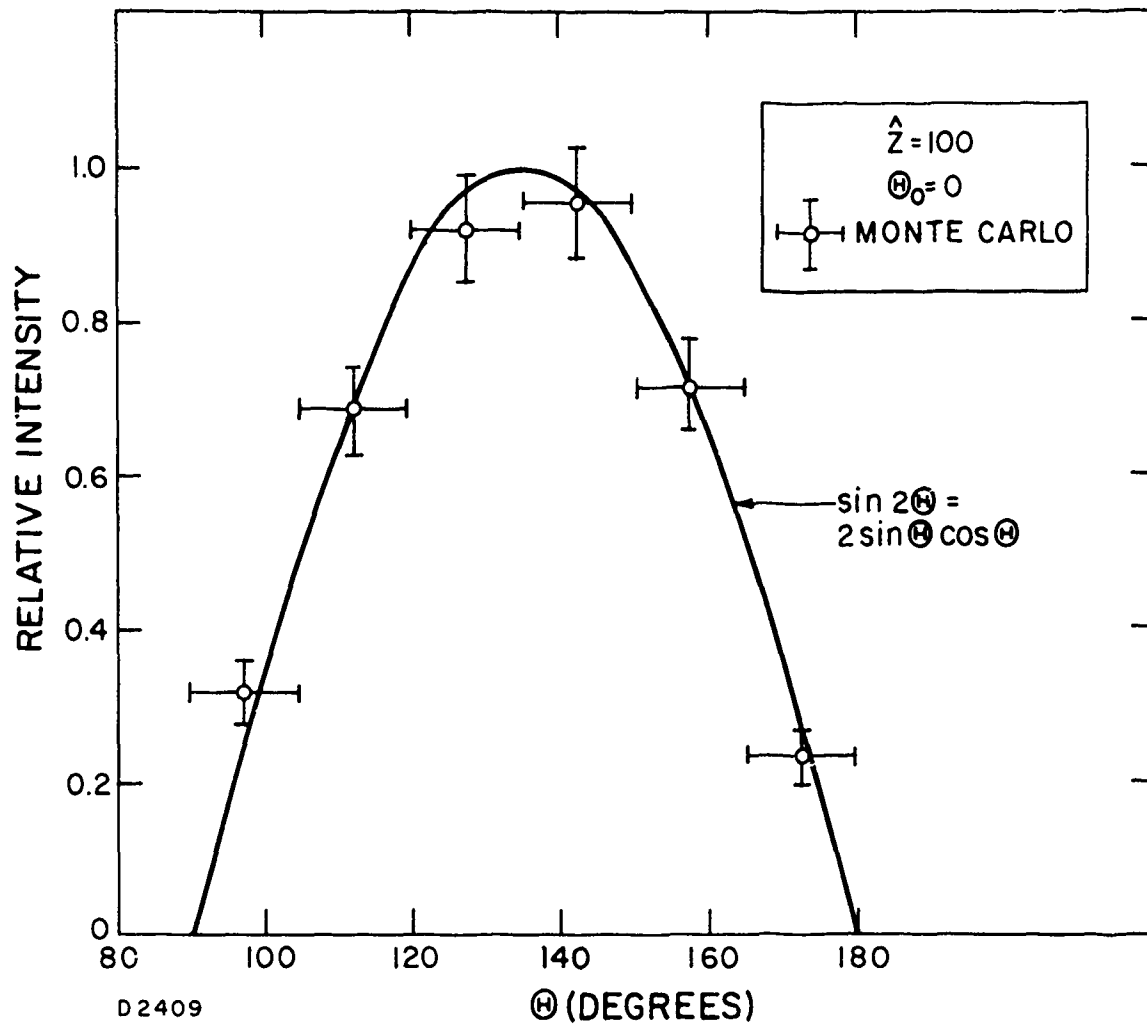


Fig. 6 The angular distribution of reflected light which is incident normal to the face of the slab with optical depth 100. The solid line is the analytic expression for a Lambert law reflection. The data symbols give the Monte Carlo histogram.

TABLE 2
REFLECTED ANGULAR DISTRIBUTION

<u>Angular Range</u>	<u>Fraction</u>	<u>Number Expected</u>		<u>Number Observed</u>
		Lambert	No Redistribution	
90° - 105°	0.067	51	32	64
105° - 120°	0.183	141	112	137
120° - 135°	0.250	192	184	185
135° - 150°	0.250	192	210	192
150° - 165°	0.183	141	167	144
165° - 180°	0.067	51	64	47

There were 129 diffuse transmitted events which is 0.17 of the amount reflected. This is close to the analytic ratio of about 0.18. The histogram of the spectrum of the diffuse transmitted photons is in statistical agreement with the analytic method and has two peaks near $x = \pm 2$. The histogram for the angular distribution does not have enough accuracy to distinguish between the Lambert law and the diffusion distribution given in the preceding paragraph.

F. DISCUSSION

A word is in order on the effect of complete redistribution. Horak, Kerr and Tierney⁴ assumed complete redistribution in their numerical calculation for the scattering of sunlight by an artificial cloud of strontium atoms. In their model 1) the neutral cloud is spherically symmetric with a radial Gaussian density dependence, 2) the two level atom has a Doppler (Gaussian) resonance transition, and 3) the solar flux is treated as constant in the scattering region. Their results for this model can be described by an effective line width. That is all of the sunlight in the spectral range where the scattering line is optically thick is scattered isotropically. Actually there is somewhat more backscattered toward the sun than away and the isotropic approximation is better at 90° from the direction of incident solar flux. The intensity (power per unit area per solid angle) at the line center is approximately the solar flux divided by 4π . The effective width of the line is the spectral region in which the optical depth through the center of the cloud exceeds 1. This result is similar to that obtained analytically without redistribution and with the correct redistribution of the Monte Carlo method. Physically this is expected since, 1) the cloud is non-absorbing and all of the incident light which enters and is scattered by the cloud must eventually diffuse out and 2) the spectral region in which the cloud is optically thick is an effective measure of the part of the solar flux which is scattered.

In summary, the total light reflected by a purely scattering slab

increases with optical depth because of the increase in effective width of the scattering resonance. This implies that a measurement of reflected intensity may be used as a measure of the column density of the scattering material. On the other hand, the total light transmitted diffusely through the slab is not sensitive to column density. In this case, two bands occur in the line wings. With spectral information the separation of these bands may be measured and may give a measure of the effective line width and hence of column density.

The spectrum determined using the Monte Carlo method with the correct redistribution shows a small effect for optical depth 100; 1) the reflected spectral intensity near the line center is reduced by about 15% and 2) this energy is displaced to a region between 2.0 and 2.3 times the Doppler half width from the line center.

The angular distribution of the reflected radiation is found to be Lambertian.

REFERENCES

1. G. Harendel and R. Lust, Artificial Plasma Clouds in Space, Scientific American, p. 81, Nov. 1968.
2. N. W. Rosenberg and G. T. Best, Chemistry of Barium Released at High Altitudes, J. Phys. Chem. 75, 1412 (1971).
3. J. T. Jefferies, Spectral Line Formation, (Blaisdell, Waltham, Mass., 1968).
4. H. G. Horak, D. M. Kerr and M. S. Tierney, Resonance Radiation in Artificial Strontium and Barium Clouds, LA-4313 (LASL, Los Alamos, New Mexico, Dec. 1969).
5. J. W. Chamberlain, Physics of the Aurora and Airglow, (Academic Press, N. Y., 1961).
6. D. E. Osterbrock, Ap. J. 135, 195 (1962).
7. P. M. Morse and H. Feshbach, Methods of Theoretical Physics, Part I, (McGraw-Hill, N. Y., 1953).
8. W. Heitler, The Quantum Theory of Radiation, (Clarendon Press, Oxford, 1954).
9. S. Chandrasekhar, Radiative Transfer, (Oxford Univ. Press, London, 1950).

CHAPTER 3
SPRUCE CORRELATION

3. SPRUCE CORRELATION

S. J. Powers Jr. and B. Kivel

A. INTRODUCTION

Considerable attention has been given to event Spruce at R + 14 min because of the coincidence of radar and optical measurements.^{1,2} This note addresses two problems in the data correlation of the event. First the optical analysis depends on the angle at which the cloud is viewed. In order to take account of the angle dependence estimates have been made of the orientation of the ion cloud face and the angle of solar illumination as well as the view angles. It is found that Tyndall views the face opposite to the solar illuminated one, while the solar illuminated face is observed from Barin. This explains the higher intensity seen from Barin. With these angles known an improved analysis of the optical intensity data leads to a consistent ion column density from Barin and Tyndall and agreement with the radar determined density. The second problem is the difference in the e^{-1} length along the earth's magnetic field direction of the ion cloud given by Thomson scatter data and that given by both optical data and an ambipolar diffusion estimate.³ According to Thomson the observed length to e^{-1} is ~ 25 km compared to the ambipolar diffusion estimate ~ 40 km. The difference is attributed to the skew angle at which the radar intersects the magnetic field line (the angle between these two directions is 3.5°). This implies, for an elliptical density profile, a width of ~ 2 km. The difference between the 2 km result and the beacon determined distance of ~ 5 km may in part be due to the east-west extent of the several sheets that comprise the trailing edge. Also, the Thomson measurement is west of the trailing edge

and does not see the four density peaks observed in the beacon data.

Section B describes the method and results of the triangulation study which locates and orients the ion cloud with respect to the sun and the measurement sites. Sections C & D consider the peak density and the density profile along the magnetic field. Density comparisons are given here. Section E treats the problem of the ion cloud length along the magnetic field and estimates the width of the ion cloud just west of the structure in the trailing edge.

B. TRIANGULATION

In order to locate the clouds, and to a somewhat lesser extent, to determine the ion cloud shape and orientation, a system of triangulation was employed. The application of triangulation requires definition of the same point in space as seen from two or more locations. The symmetry of the neutral cloud lends itself to the application of rigorous triangulation since the center of the cloud can usually be estimated unambiguously from any location. Identification of a common point on the ion cloud as seen from two different locations is more difficult since many prominent features as seen from one sight become confusingly dissimilar when viewed from another site with different viewing aspect.

Instead of a rigorous triangulation method, estimates of cloud location and shape were made by projecting photographic point images from one location into the other photographic field of view.

Photographic records of the Spruce release taken from Tyndall and C-6 were available at various common times after release. Included on each record were the neutral cloud, ion cloud and background stars. Star coordinates were read from an overlay grid on each photograph. Approximately six sets of coordinates on each photograph were measured. These measurements, along with the known right ascension and declination of each star, and refraction corrections were combined in a least squares solution for determination of three angles of photograph orientation with respect to the local vertical-north coordinate system and an equivalent focal length (plate scale).

Having oriented the photograph we obtain a vector from the center of the earth to a point in the photograph as follows. The transformation matrix M between the photograph and the observer's local vertical coordinate system can be formed from trigonometric functions of the orientation angles. A vector from the observer in the direction of a photographic image can be expressed in the local system as:

$$\underline{v} = M \underline{c}$$

where

$$\underline{c} = \begin{pmatrix} x \\ y \\ f_1 \end{pmatrix}$$

$$M = \begin{pmatrix} c\beta c \chi - s \alpha s \beta s \chi & -c\beta s \chi - s \alpha s \beta c \chi & c \alpha s \beta \\ -s \beta c \chi - s \alpha c \beta s \chi & s \beta s \chi - s \alpha c \beta c \chi & c \alpha c \beta \\ c \alpha s \chi & c \alpha c \chi & s \alpha \end{pmatrix}$$

α = elevation angle of the optical axis

β = azimuth angle of the optical axis

χ = rotation of the photographic coordinate system about the optical axis

$s \equiv \sin$

$c \equiv \cos$

x and y are photograph measurements and f_1 is the equivalent focal length.

The position vector \underline{q} of the observation site in the earth centered coordinate system was formed using the method suggested by Chang and

Oetzel.⁴ The rotational transformation R between the observation site local vertical system and t^1 , earth centered coordinate system was formed based on the longitude and latitude of the site. The line of sight unit vector in the direction of a photographic image can then be expressed in the earth centered system as:

$$\underline{e} = R \underline{v}$$

and

$$R = \begin{pmatrix} -s\theta & -s\phi c\theta & c\phi c\theta \\ c\theta & -s\phi s\theta & c\phi s\theta \\ 0 & c\phi & s\phi \end{pmatrix}$$

where

- θ = longitude measured positive east
- ϕ = geodetic latitude
- $s \equiv \sin$
- $c \equiv \cos$

The position vector $\underline{t} = \underline{q} + k \underline{e}$ represents the earth centered position vector of a target that is k units in range from the observation site. The magnitude, k , of the target vector was varied and the corresponding altitude, longitude, and latitude was computed in the iterative procedure suggested by Chang and Oetzel. In this manner, ground plots of the line of sight vector at different altitudes were generated.

The line of sight can now be located in a photograph taken at the same time from another site. Knowledge of the latitude, longitude, and altitude for the second observation site enables one to compute its earth centered position vector \underline{q}_2 . The line of sight vector to the target as seen

from the second location is given by:

$$\underline{e}_2 = \underline{t} - \underline{q}_2$$

where the subscript 2 is for the second site values. Expressed in the local vertical system at the second location:

$$\underline{v}_2 = R_2^{-1} \underline{e}_2$$

where R^{-1} is the inverse matrix of R . This is expressed in the second photographic system as:

$$\underline{c}_2' = M_2^{-1} \underline{v}_2$$

When the third component of c_2' is scaled to the previously computed effective focal length of the second photograph, the photographic coordinates of the target result:

$$\underline{c}_2 = \begin{pmatrix} x_2 \\ y_2 \\ fl_2 \end{pmatrix}$$

The results of projecting points, C, G, and E, noted in the Tyndall photograph, Fig. 1, at $R + 13 \frac{1}{4}$ min, into the photographic field of view at the C-6 site are shown in Fig. 2. Also noted is the projection of point P from the Fort Meyers site as observed at $R + 14$ min into both fields of view.

Computation of Normal Angles

The approximate midpoint of the sharp edge of the ion cloud, designated point C in Fig. 1, was determined to be at 182 km altitude based on the line of sight intersection seen in Fig. 2. This agrees with the

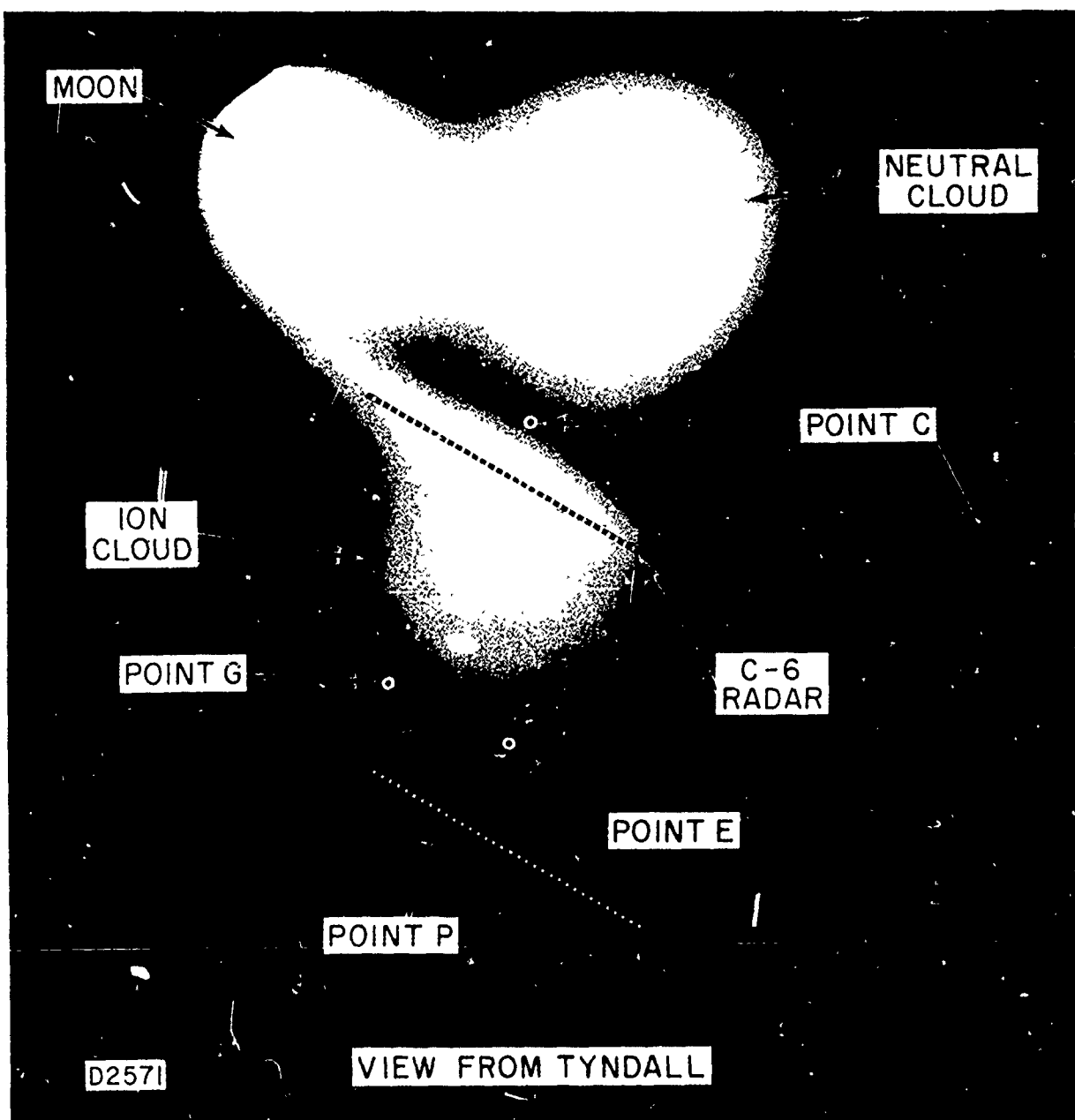


Fig. 1 Photograph from Tyndall of Spruce at R + 13.25 min.

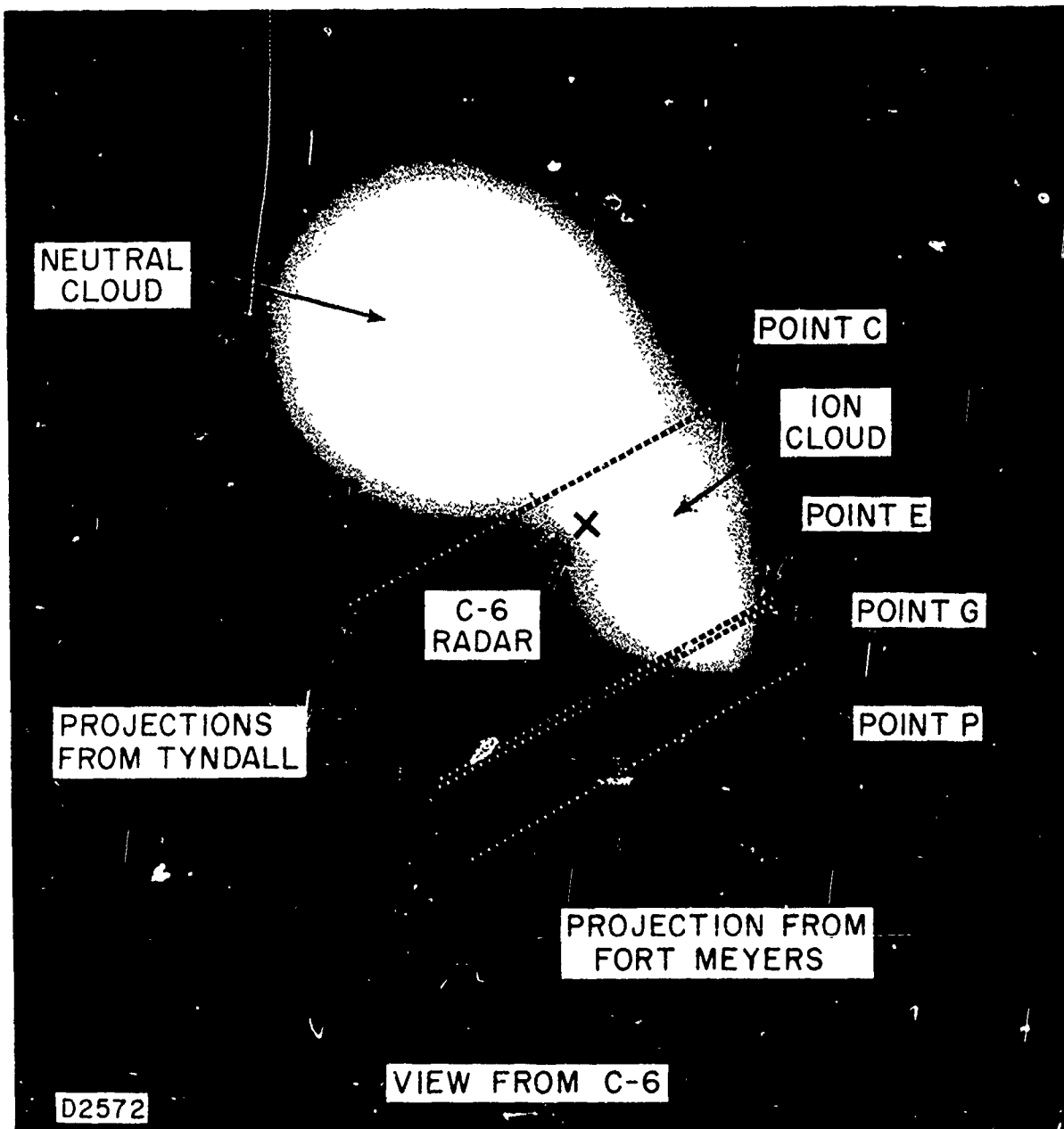


Fig. 2 Photograph from C-6 site of Spruce at R + 13.25 min.

earlier results⁵ (see Ref. 5, p. 91). The corresponding latitude and longitude for point C at that altitude is shown in the ground plot in Fig. 3. A preliminary estimate of the altitude for point C was 185 km and initial calculations were carried out based on this value.

In a similar manner, approximate positions for points G, E, and P were determined. The earth centered position vectors \underline{t}_c , \underline{t}_e , \underline{t}_g , and \underline{t}_p were calculated and the differences formed; $\underline{t}_e - \underline{t}_c$, $\underline{t}_g - \underline{t}_c$, and $\underline{t}_p - \underline{t}_c$. Since all points are assumed to lie in the plane of the ion cloud sheet, the above difference vectors were assumed in that plane. These vectors were expressed in the local vertical system at point C as:

$$\underline{E} = R_c^{-1} (\underline{t}_e - \underline{t}_c)$$

$$\underline{G} = R_c^{-1} (\underline{t}_g - \underline{t}_c)$$

$$\underline{P} = R_c^{-1} (\underline{t}_p - \underline{t}_c)$$

The magnetic field vector direction, H, was defined in the local vertical system at point C by means of the dip angle and declination. The sharp edge of the ion cloud is felt to be parallel to H. The vector product of H with each of the difference vectors represents a vector normal to the plane since all vectors are assumed coplanar. This vector is designated \underline{V}_N . For H we have assumed dip = 61.2 and dec. = 2.6°E.

The line of sight vector from point C to the sites at Tyndall and Barin is expressed in the local vertical system at point C as:

$$\underline{v}_T = R_c^{-1} (\underline{q}_T - \underline{t}_c)$$

$$\underline{v}_B = R_c^{-1} (\underline{q}_B - \underline{t}_c)$$

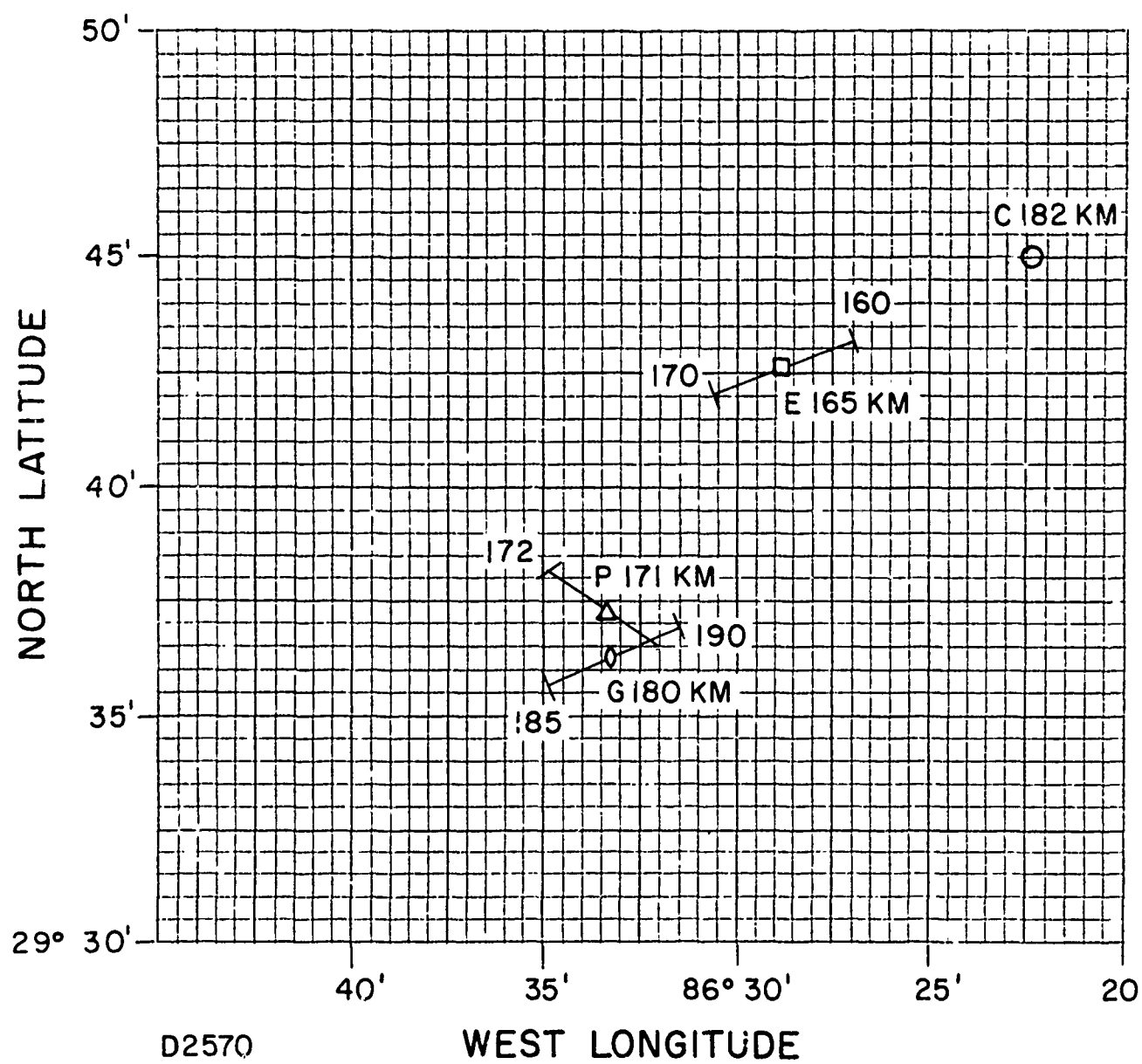


Fig. 3 Ground plot locating Spruce at R + 13.25 min.

A vector, \underline{S} , in the direction of the sun from point C was formed from the computed azimuth and elevation angles of the sun. After normalizing all vector magnitudes to unity, the scalar product of the line of sight vector to the sun, \underline{S} , and the vector normal to the plane, \underline{V}_N , was formed. This quantity represents the cosine of the angle, Θ_S , between the two vectors.

$$\cos \Theta_S = \underline{S} \cdot \underline{V}_N$$

We have used for the location of the sun at R + 14 min, right ascension = 20h 59. 83 and declination = $-17^\circ 3. 6'$.

In a similar manner, the angles to Tyndall and Barin (Θ_T and Θ_B) were computed. The positions of E, G, and P were adjusted until the angle between the resultant vector normal to the plane and the line of sight vectors to Tyndall and Barin and the sun gave consistent results. These results are given in Table 1. Angles larger than 90° are on the face opposite to those with angles less than 90° . The values obtained assuming an altitude for point C of 185 km are given in Table 2, which may be compared with the results in Table 1 to estimate the sensitivity to the altitude of point C.

The approximate orientation of the ion cloud was determined in the above manner. In a coordinate system centered at the position of point C, the vectors \underline{H} , along the magnetic field; \underline{V}_N , normal to the plane of the sheet; and $\underline{V}_L = \underline{H} \times \underline{V}_N$ are used to describe the orientation of the ion cloud.

The R + 14 min line of sight of the radar located at the C-6 site is indicated in the photographs from Tyndall and C-6 (Figs. 1 and 2). We use

the values provided by Roland Tsunoda of SRI of 61.3° elevation and 189.9° azimuth. The scalar product of the radar line of sight vector with each of the coordinate axes indicated that the radar line of sight makes an angle of 3.5° with the magnetic field line. The intersection of the radar line of sight and the ion cloud appears to occur at a point ~ 2 km below C in altitude and ~ 5 km in the V_1 direction.

TABLE 1
POINT C AT 182 km*

Point	Alt. (H) (km)	θ_S ($^\circ$)	$\frac{d\theta_S}{dH}$ ($^\circ/\text{km}$)	θ_B ($^\circ$)	$\frac{d\theta_B}{dH}$ ($^\circ/\text{km}$)	θ_T ($^\circ$)	$\frac{d\theta_T}{dH}$ ($^\circ/\text{km}$)
P	171	118	6.6	108	3.3	59	0.7
G	180	117	1.5	108	0.8	59	0.2
E	164	118	2.0	108	0.9	59	0.06

*longitude = $86^\circ 22.4'$ W, latitude = $29^\circ 45.1'$ N

TABLE 2
POINT C AT 185 km*

Point	Alt. (H) (km)	θ_S ($^\circ$)	$\frac{d\theta_S}{dH}$ ($^\circ/\text{km}$)	θ_B ($^\circ$)	$\frac{d\theta_B}{dH}$ ($^\circ/\text{km}$)	θ_T ($^\circ$)	$\frac{d\theta_T}{dH}$ ($^\circ/\text{km}$)
P	171	121	6.4	109	3.0	58	0.3
G	180	121	1.6	109	0.8	58	0.1
E	165	121	1.9	109	0.9	59	0.15

*longitude = $86^\circ 23.1'$ W, latitude = $29^\circ 44.9'$ N

C. PEAK DENSITY

With information on the angles made by the solar flux and the views from Tyndall and Barin to the face of the cloud we can make a correction to the analysis of column density in event Spruce at 14 min after the release. As a first approximation we have been using a model developed for a spherical cloud. Modeling for a slab has also been reported.^{1,2} In this section we apply the slab model to obtain improved estimates of the peak ion column density. The peak unfiltered intensity as seen from Barin is $6.3 \times 10^{-8} \text{ w/cm}^2 \Omega$ (see Ref. 5, p. 29). For the spherical model this gave a column density of $1.2 \times 10^{13} \text{ cm}^{-2}$. Assuming a cloud width⁶ of 5 km the corresponding peak ion density is $2.4 \times 10^7 \text{ cm}^{-3}$. This is about three times higher than indicated by the radar data (see Ref. 1, p. 34 and Ref. 2, Fig. 5). At normal incidence for the solar flux the slab case is about 4 times that estimated for the sphere for large optical depth. The solar flux of $\sim 60^\circ$ to the normal reduces the slab intensity by about a factor 2. There is not much correction for the view angle in the neighborhood of 60° and optical depths $\gtrsim 100$. As a result it requires less column density to provide the observed intensity. For the unfiltered light at densities of interest the intensity increases approximately as the square root of the column density. Accordingly, we estimate the column density to be reduced to $\sim 3 \times 10^{12} \text{ cm}^{-2}$. Again taking a slab width of 5 km this implies a peak density of about $6 \times 10^6 \text{ cm}^{-3}$ in agreement with the other data.

In view of the insensitivity of cloud intensity to column density on the

dark side we cannot reliably estimate column densities from the observed intensity at Tyndall. We do, however, try to show for the ion density $\sim 3 \times 10^{12} \text{ cm}^{-2}$ that the observed intensity is consistent. The data from Tyndall is for the spectral line at 4934A. The ratio of the filtered light at 4934A to the total unfiltered light for a column density in the neighborhood of $3 \times 10^{12} \text{ cm}^{-2}$, is about 1/10 (e.g., Ref. 5, p. 140). At the corresponding optical depth $\tau \approx 30$ the intensity on the back face should be about 1/2 of that on the front face (Ref. 1, p. 10). Combining these two factors we expect the observed intensity from Tyndall in the filtered photograph to be about 1/20th of that observed from Barin in the unfiltered photograph. Reducing the Barin intensity by 20 we obtain $3 \times 10^{-9} \text{ w/cm}^2\Omega$. This is slightly larger than the observed value from Tyndall of $2 \times 10^{-9} \text{ w/cm}^2\Omega$ (Ref. 1, p. 27); however, not inconsistent in view of the approximate method used to estimate the expected intensity. By comparing Tyndall to Barin we have avoided making the correction for the solar and view angles since the solar flux angle is the same for both cases and the result is insensitive to view angle. The view angle from Barin is $\sim 70^\circ$ to the normal compared to $\sim 60^\circ$ for Tyndall. While the reciprocal of the cosine of the view angle differs in the two cases by a factor 1.5, in the optically thick limit the effect of view angle is small and the difference can be neglected (Ref. 1, p. 19).

D. DENSITY PROFILE

In order to estimate the ion density along the magnetic field at positions away from the peak density, we have prepared the correlation between intensity and column density shown in Fig. 4. The dashed lines are the results for spherical clouds for unfiltered and 4934A intensities as a function of column density. The solid lines are the slab estimates appropriate to the analysis of Spruce data at 14 min after release. The data from Barin is an unfiltered photograph. In the optically thin region the intensity for the same column density is expected to be about three times larger, corresponding to a view angle of $\sim 70^\circ$ from the normal to the cloud face. The effect of view angle becomes negligible when the column density is $3 \times 10^{12} \text{ cm}^{-2}$. The factor 4 for the geometric difference between the slab and sphere reflection is reduced by a factor 2 for the solar flux angle of $\sim 60^\circ$. In a similar manner we estimate the correlation as seen on the backside of the cloud from Tyndall. In the optically thin region the view angle of $\sim 60^\circ$ leads to an expected factor of 2 increase in intensity. In the optically thick region the intensity is insensitive to column density. Our correlation in this region is only indicative since it is not calculated with precision.

Using the correlation in Fig. 4 between column density and observed intensity appropriate for the Spruce at $R + 14$ min the column density as a function of location along the magnetic field in the neighborhood of the trailing edge is obtained. The results are shown in Fig. 5. The symbols x and o indicate respectively the data from Barin in the unfiltered photograph and

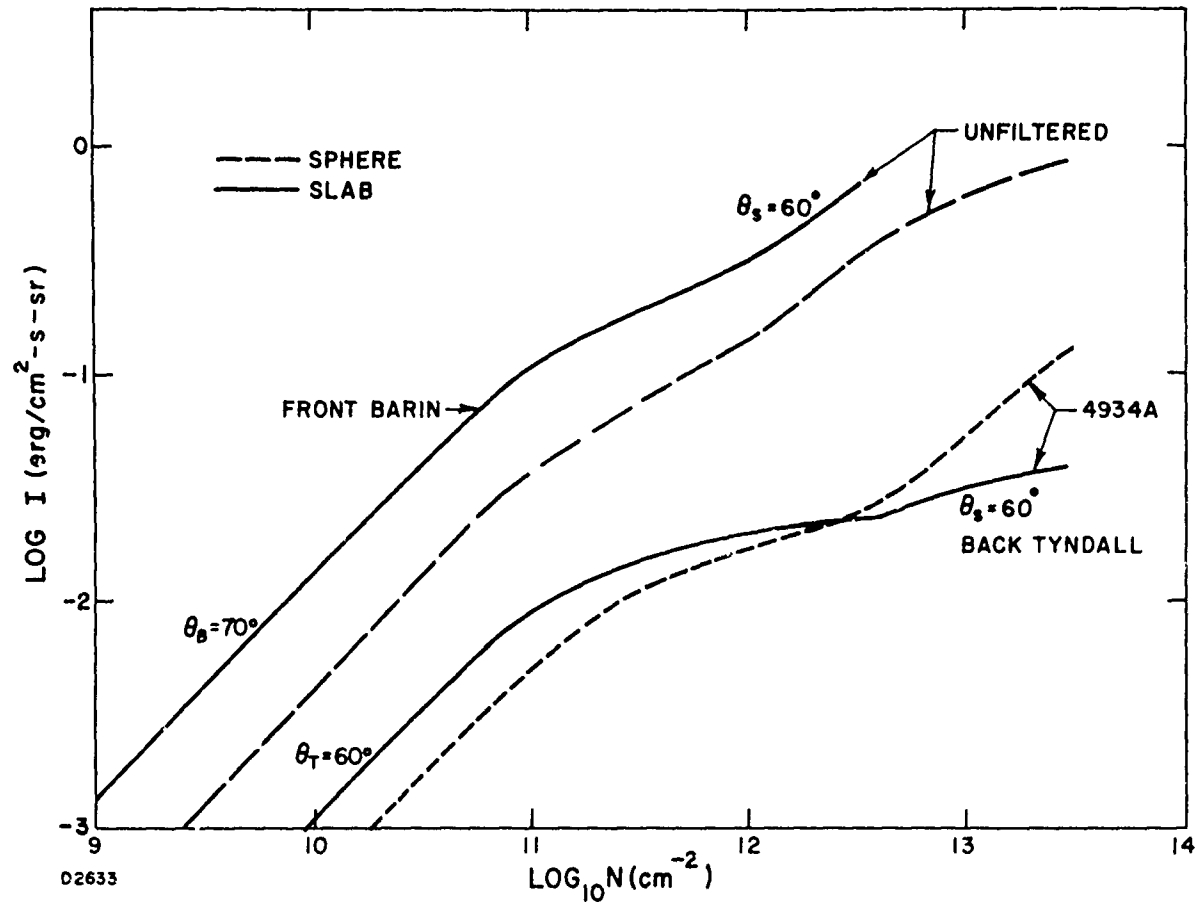


Fig. 4 Correlation of cloud intensity vs ion column density comparing spherical and slab models. The slab model is appropriate to Spruce at R + 14 min.

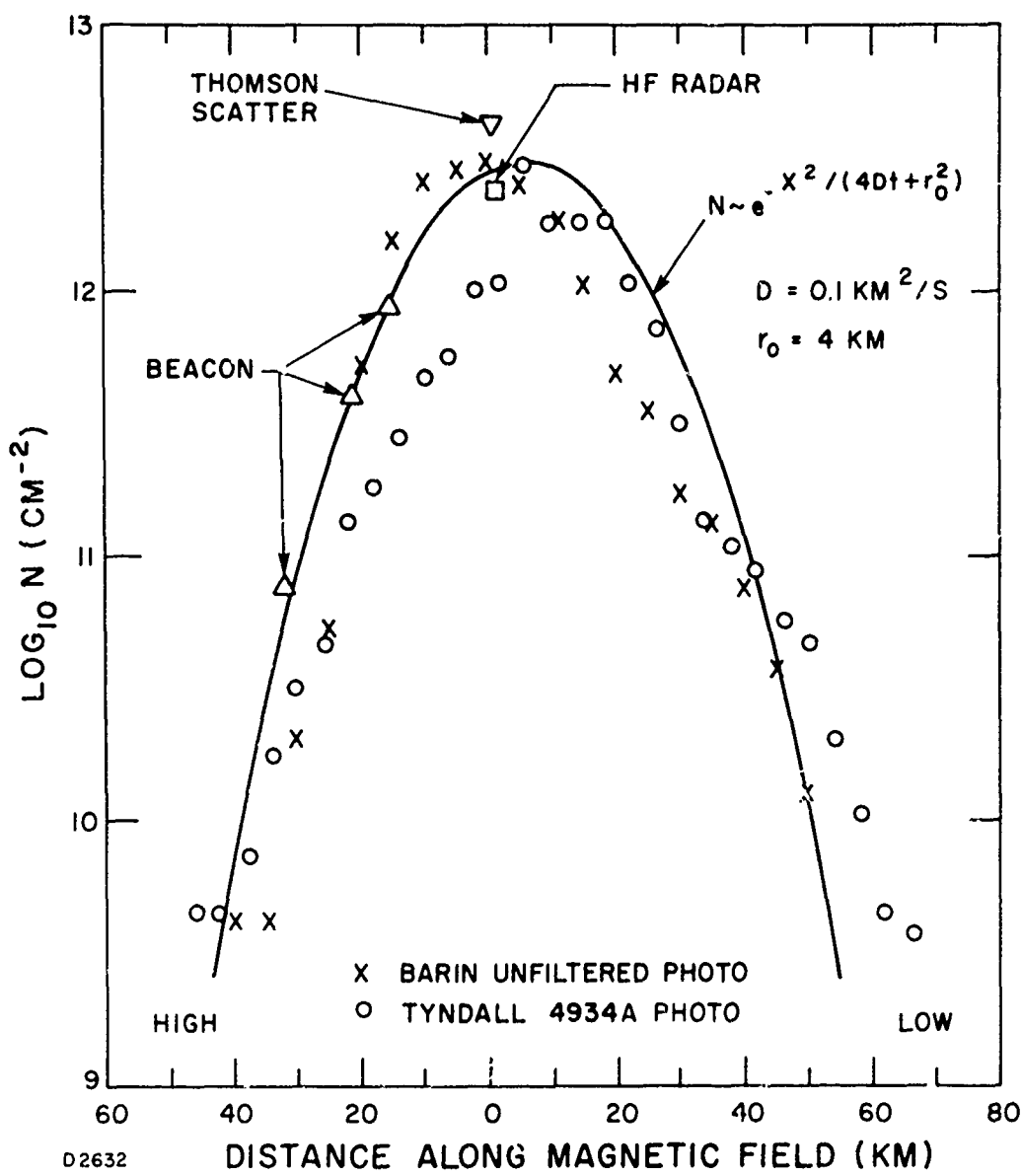


Fig. 5 Data correlation of Spruce at R + 14 min giving ion column density near trailing edge as a function of relative distance along the earth's magnetic field.

from Tyndall in the filtered photograph at 4934A. The distance along the magnetic field is the abscissa and the log to the base 10 of the column density is the ordinant. The high altitude region is to the reader's left and the low to the right as marked on the figure. In the figure we compare an expression for the expected distribution for ambipolar diffusion and results from radar observations. The ambipolar diffusion has a Gaussian distribution with a half width of $\sqrt{(4Dt + r_o^2)}$ where D is the ambipolar diffusion coefficient taken to be $0.1 \text{ km}^2/\text{s}$, r_o is the initial radius taken to be 4 km and t is the time.³ This distribution is consistent with the optical data. The beacon data is also consistent with the Gaussian distribution in the high altitude region where data was obtained.⁶ The beacon data also gives an estimate of the cloud thickness appropriate to the trailing edge of the cloud of about 5 km . We use this width in converting the Thomson scatter and HF radar data electron density to column density. Taking this width the radar data is in agreement with the optical result.

The density profile from the Thomson scatter data does not agree with the optical value having a half width of about 12 km compared to 19 km from the optical data and ambipolar diffusion model. We postulate that the shorter extent of the Thomson data is a result of the angular offset of the radar line of sight from the direction of the earth's magnetic field. In the next section we use this difference to estimate the width of the Spruce cloud in the region of the Thomson scatter measurement.

E. CLOUD WIDTH FROM THOMSON SCATTER DATA

The Thomson scatter results may be used to estimate cloud width. We have noted in comparing the profile of the Thomson scatter with the optical density that the Thomson determined length along the field direction is significantly less than: 1) that determined optically, and 2) that expected from Linson's correlation. We attribute this to the skew angle at which the cloud is observed by the Thomson scatter measurement.

Using the center beam orientation as provided by R. Tsunoda of SRI we have oriented the beam with respect to the ion cloud at $R + 14$ min. The ion cloud is defined by the following three vectors. The magnetic field vector pointing from the cloud down toward the north (\underline{H}). A vector perpendicular to the magnetic field and pointing from the center of the trailing edge in the east toward the center of the leading edge in the west (\underline{V}_\perp) and a mutually perpendicular vector which is also normal to the face of the ion slab pointing down (\underline{V}_N). In this coordinate system we define the polar angle, θ , with respect to the \underline{H} axis and the azimuthal angle, ϕ , in the plane defined by \underline{V}_N and \underline{V}_\perp with the $\phi = 0$ value in the \underline{V}_N direction. In terms of these angles the radar intersects the cloud at $\theta = 3.5^\circ$ and $\phi = -15.9^\circ$. With these values the radar beam is more to the east when close to the radar site than a magnetic field line through the center of the trailing edge of the ion cloud, while further west when away from the radar toward the southern conjugate region. This is consistent with the azimuth of the radar and the declination of the earth's magnetic field. The radar

beam is below the magnetic field line through the center of the trailing edge when close to the radar in the north and above the magnetic field line when away from the radar towards the south.

To estimate the cloud width we assume a Gaussian ellipsoidal shape which is independent of the location in the east-west direction along \underline{V}_\perp . The major axis of the ellipse is taken along the magnetic field line, \underline{H} , and is estimated from the optical data and from Linson's correlation to have a half length of about 19 km. The breadth along the normal to the cloud face \underline{V}_N is estimated from the observed Thomson radar profile which shows a half width of about 12 km at R + 14 min. The breadth b is obtained from

$$1 = \left(\frac{r \cos \theta}{a} \right)^2 + \left(\frac{r \sin \theta \cos \phi}{b} \right)^2$$

where r is the Thomson scatter e^{-1} range, a is the e^{-1} range along the earth's magnetic field (19 km), θ , ϕ , are the polar and azimuthal angles as defined above, and b is the e^{-1} half-width of the cloud breadth normal to the face of the cloud. This evaluation gives a value for the width of $2b \approx 2$ km.

There are two obvious differences between Thomson scatter and beacon experiment results. Thomson scatter measures only one ion density peak and a 2 km width while the beacon experiment measures several peaks and a 5 km width. We assume that this difference is explained by the fact that the Thomson scatter measurement is made west of the trailing edge; that is, west of the region where the structure is observed in the optical photographs. (Note that in Figs. 1 and 2 the radar line of sight at 14 min is used with photographs at $13\frac{1}{4}$ min. At 14 min the radar is about 7 km

west of the trailing edge and slightly further west than indicated in the figures.) The lack of structure and smaller width west of the trailing edge region is consistent with current models for ion cloud structure.⁷

REFERENCES

1. B. Kivel and L. F. Cianciolo, "Data Correlation" in Analysis of Barium Clouds, RADC TR-72-103, Vol. I, (Avco Everett Research Laboratory, Semi-Annual Technical Report, January 1972), pl.
2. B. Kivel and G. M. Weyl, "SECEDE II Optical and Radar Data Correlation (U)," in Proceedings of the SECEDE II Final Data Review Meeting, RADC TR-72-153, Vol. I, (Stanford Research Institute, May 1972) p. 127. (SECRET)
3. L. M. Linson and M. J. Baron, "Ion-Cloud Parallel Diffusion -- Comparison of RF, Optical, and Theoretical Results," in Proceedings of the 1971 Technical Planning Session, RADC TR-71-200, Vol. I (Stanford Research Institute, September 1971) p. 161. (SECRET)
4. N. J. F. Chang and G. N. Oetzel, "Comparison of Coordinate Systems for SECEDE II Data Reduction," (U) in Proceedings of the 1971 Technical Planning Session, RADC TR-71-200, Supplement (Stanford Research Institute, December 1971), p. 85. (SECRET)
5. B. Kivel, Fig. V. 20 in "Ion Density Data Study" in Analysis of Barium Clouds, Semi-Annual Technical Report, RADC TR-71-253, Vol. I, (Avco Everett Research Laboratory, June 1971) p. 140.
6. A. A. Burns and R. C. Livingston, "R. F. Beacon Experiment Results," in Proceedings of the SECEDE II Final Data Review Meeting, RADC TR-72-153, Vol. II (Stanford Research Institute, May 1972) p. 243.
7. L. M. Linson", Status of Theoretical Understanding of Barium Cloud Phenomenology," in Proceedings of the SECEDE II Final Data Review Meeting, RADC TR-72-153, Vol. II (Stanford Research Institute, May 1972) p. 1. (See also Chapter 5 of this report.)

CHAPTER 4

**USE OF PHOTOGRAPHIC DATA FOR ESTIMATING
ION DENSITY AND INVENTORY**

4. USE OF PHOTOGRAPHIC DATA FOR ESTIMATING ION DENSITY AND INVENTORY

B. Kivel

A. INTRODUCTION

Photographic data give important information on cloud shape, growth and location; in addition, when calibrated to give absolute intensity, photographic analysis can be used in a more quantitative way to obtain estimates of ion density and ion column density. Unfortunately because of many unknowns, which we will discuss, it is not at present possible to make an absolute density determination independent of other measurements. The intensity must be normalized by radar data. The radar normalization of the relation between ion column density and photographic intensity is less complicated at short times after the chemical release when the ion cloud has a symmetric shape. Once a semi-empirical relation has been established, it is possible to use the result at other times and places in the same event and, even more important, for other events.

One aspect of the quantitative use of calibrated film data that has not been pursued is its use in regard to the triangulation problem. It is difficult to find a cloud location by triangulation because the cloud is transparent, not symmetric, and data from different sites often have different sensitivity and as a result it is difficult to find points of coincidence in diverse pictures. This problem may be ameliorated using data calibrated in terms of ion column density.

The remainder of this chapter is divided into four parts. The uncertainties in calibrating and interpreting film data are discussed in Sec. B. Section C deals with data in the optically thin limit. In this limit effects of optical depth are not important and the column density is linearly related to the measured intensity. This relationship is particularly useful for application at the cloud edge and at late times. Section D deals with the optically thick limit where an effective line width method for semi-empirical correlation of ion column density and film intensity is presented. Also in Sec. D the effects of cloud shape, the angle at which the cloud is viewed and the angle at which the solar flux impinges on the cloud are discussed. Section E deals with applications to data from releases in SECEDE I and Spruce in SECEDE II.

B. DIFFICULTIES WITH OPTICAL ANALYSIS

The difficulties can be divided into two classes: 1) data reduction, and 2) interpretation of the reduced data.

Film calibration to obtain the absolute intensity of the source is generally a difficult problem; however, with care, consistent results can be obtained with accuracy generally better than a factor 2.

SECEDE observation has several specific problems. These include reciprocity, film temperature, and atmospheric transmission. The reciprocity effect is the sensitivity of the film to the exposure time. To correct for this effect it is necessary that the calibration be applied at the same exposure time. Film sensitivity also depends on film temperature. In SECEDE II, although the experiments were done in Florida, the temperature of the observing outdoor cameras was $\sim 30^{\circ}\text{F}$ while the calibration standard was put on the film at an indoor temperature. The colder film is apparently more sensitive and a correction for this effect is required.

Atmospheric transmission reduces the signal from a barium cloud but does not change the signal from a standard lamp. Because the ground haze in the Eglin area was particularly heavy at times, transmission corrections should be made. One method, which corrects all three of these effects simultaneously, is the use of known standard star intensities within the photographic data to normalize the intensity calibration. The stars are exposed on the film with the same exposure time, the same film temperature, and having the same elevation angle as the observed ion cloud and hence the same attenuation correction for atmospheric haze. There are two limitations on the use of star calibration techniques: 1) stars are not

evident in filtered photographs which look at selected ion lines, and 2) the unfiltered photographs which show stars are not useful at early time after release when the neutral and ion clouds overlap. These two problems may be alleviated by combining several data films. Unfiltered late time photographs when stars are available and the ion cloud is separated from the neutral cloud may provide a standard to calibrate the intensity in terms of the star intensities. With this information filtered photographs at the same time can be normalized by comparing ion cloud intensities. This calibration information can also be used at earlier times. The reciprocity correction can be achieved by comparing photographs at essentially the same time with different exposure times.

Calibrated intensity information does not immediately give ion cloud density. There are several unknowns which prevent this correlation being made on an absolute basis. A basic requirement is the solar flux spectral distribution. Because of the strong Fraunhofer effect the spectrum is far from uniform in the neighborhood of the barium ion lines. Since it is possible to measure the spectral flux from the sun with good resolution, it is recommended that these measurements be made. One must also consider sunlight reflected from the earth. Another fundamental limitation, not as easily removed, is the difficult problem of radiation transport. Barium has odd and even mass isotopes. The odd mass isotopes have resonant scattering transitions split into several spectral components. This complicates the spectrum and allows photons to travel with longer mean-free-paths than in adjacent spectral regions. Another complication of the radiation transport problem is the occurrence of metastable levels

in the barium ion. The population of the metastable levels depends on the radiation density in the neighborhood of the scattering ion, which in turn is determined by the metastable level population. Therefore, the atomic population and radiation transport are not uncoupled problems. Also this problem is not a local one since the radiation density at the ion is determined by radiation emission throughout the cloud. Radiation transport approximations have been made for simple geometric shapes and will be discussed in Sec. D. The correct solution requires a complicated iteration between guessing cloud geometry and ion density distribution, solving the radiation transport problem, comparing the predicted intensity from the radiation transport solution with the observed photographic intensities, then correcting the geometric model in order to correct for the discrepancies between the predictions and observations and then repeating the process until a satisfactory agreement between prediction and observation is obtained. One aspect of the geometry that has to be handled even for simple methods of analysis is the dependence of intensity on view angle and solar flux angle. Another complication is the effect of collisions which can reduce the metastable level population. This latter complication becomes more important at lower altitudes.

As a result of the difficulties enumerated above, it is concluded that optics is an uncertain source for absolute ion density determination. Its basic value is for interpolating and extrapolating from radar determined values of peak ion density or column density.

C. OPTICALLY THIN LIMIT

In the optically thin limit the intensity is proportional to the column density. In this region the cloud is essentially transparent and only single scattering events need be considered. After the solar flux has been determined, this method can be used on an absolute basis independent of radar measurements. The difficulty of determining the metastable populations is simpler in the thin than the thick limit because the transition rates are determined by the solar flux independent of the cloud properties.

The optically thin limit is useful in analyzing the outer edge of ion clouds at early times even though the center is optically thick. The approach is to determine the column density at the edge where the cloud is optically thin and then extrapolate to the cloud center using a Gaussian density distribution. Another application of the optically thin limit is at late times when the density has gotten sufficiently low because of cloud growth. This limit may be determined by taking the integral of the intensity over the area of the cloud. At early times this integral increases with time because of the increasing cloud area; however, when the cloud becomes optically thin the integral should remain constant corresponding to the constant total ion inventory in the cloud.

D. OPTICALLY THICK LIMIT

In the optically thick limit the cloud is not transparent and multiple scattering is important. In this case atoms on the observer's side of the cloud block radiation from atoms on the far side. The effect of the distant atoms is only seen in the wings of the scattering line where the cloud becomes transparent. In this case the total intensity does not increase linearly with column density but only as fast as the effective spectral line width increases. The effective spectral line width is determined by that spectral region of the scattering line which is optically thick.

In analyzing intensities for optically thick clouds, two cloud shapes should be distinguished. At early times the cloud is spherical or ellipsoidal and at later time after release a slab shape may be more appropriate. The elliptical cloud radiation is essentially isotropic although slightly more radiation is reflected toward the sun than away from it and this anisotropy increases with optical depth. The flat cloud gives a large reflection from the solar illuminated side while the total transmitted intensity is only ~ 20% of that reflected. The reflected intensity goes up with the effective spectral width and is about four times the intensity from an ellipsoidal cloud. The transmitted intensity occurs in the wings of the scattering line where the optical depth is about 2; i. e., the cloud thickness is about twice the radiation mean-free-path. The total transmitted light intensity is insensitive to column density; however, the spectral shape does change and the separation between the two bands in the wings of the line increases with optical depth. This separation cannot be measured photographically but may be observed with an interferometer.

Another aspect of the slab type cloud is the effect of the angle at which the cloud is viewed and the angle at which the sun illuminates the cloud. In the optically thin limit the intensity increases inversely as the cosine of the angle of view made with the normal. This increase occurs because more atoms are viewed through the slab at a slant angle than at the normal direction. On the other hand, in the thin limit the intensity is independent of the solar angle since all atoms receive the same solar flux. In the optically thick limit on the reflected side the intensity is independent of angle since the surface is approximately a Lambert law scatterer. In this case, however, the solar flux angle enters as the reciprocal of the cosine to the normal since the solar flux is spread over a larger area of the slab face.

E. APPLICATIONS

In this section we briefly comment on data from SECEDE I and II. The SECEDE I releases are used to illustrate the method of adjusting the correlation between ion density and intensity using the HF radar determined peak electron density. The Spruce cloud is of interest because it has a significant body of radar, photographic and optical interferometer data. In addition, the Spruce cloud at 14 minutes after release may be described as a slab and the effects of solar and view angle are important.

In Fig. 1 we show a correlation of intensity as a function of column density for Apple and Dogwood data for $\lambda = 4554\text{A}$ BalI resonance line. The numbers under the data points indicate the time after release in minutes. For these early time data, the elliptical cloud model is reasonable. The solid line in the figure is a semi-empirical model which is linear at lower column density and levels off following an effective width at high optical depth. The magnitude of the line is adjusted to agree with the data points. The intensity of the data points is determined photographically and the column density is the product of the peak radar determined electron density and the cloud width for a Gaussian shaped cloud based on the optical data.

A more complete correlation is given in Fig. 2. Correlations for sphere and slab models are given for both unfiltered photographic data and for light at $\lambda = 4934\text{A}$ BalI resonance line. The dashed lines are for the spherical model. The solid lines are for observations from Barin and Tyndall as indicated. Barin was on the solar illuminated side and views the cloud at 70 degrees to the normal. The solar flux is incident on the cloud making an angle of 60 degrees to the normal. Tyndall is on the back

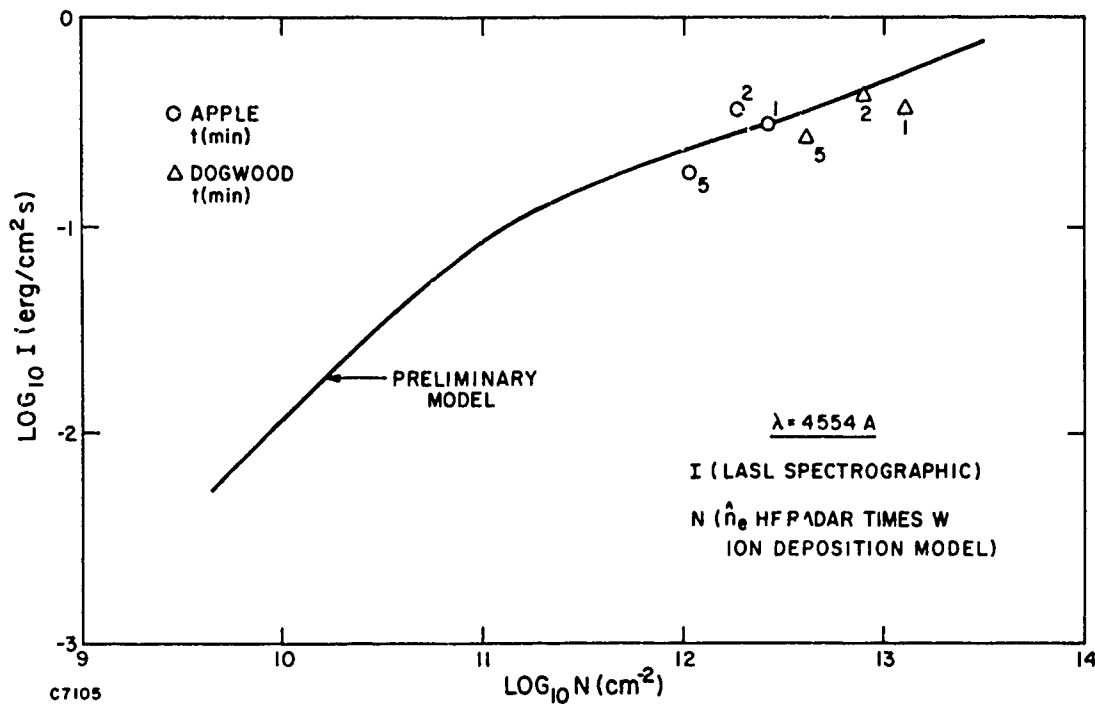


Fig. 1 Correlation of photographic data from SECEDE I.

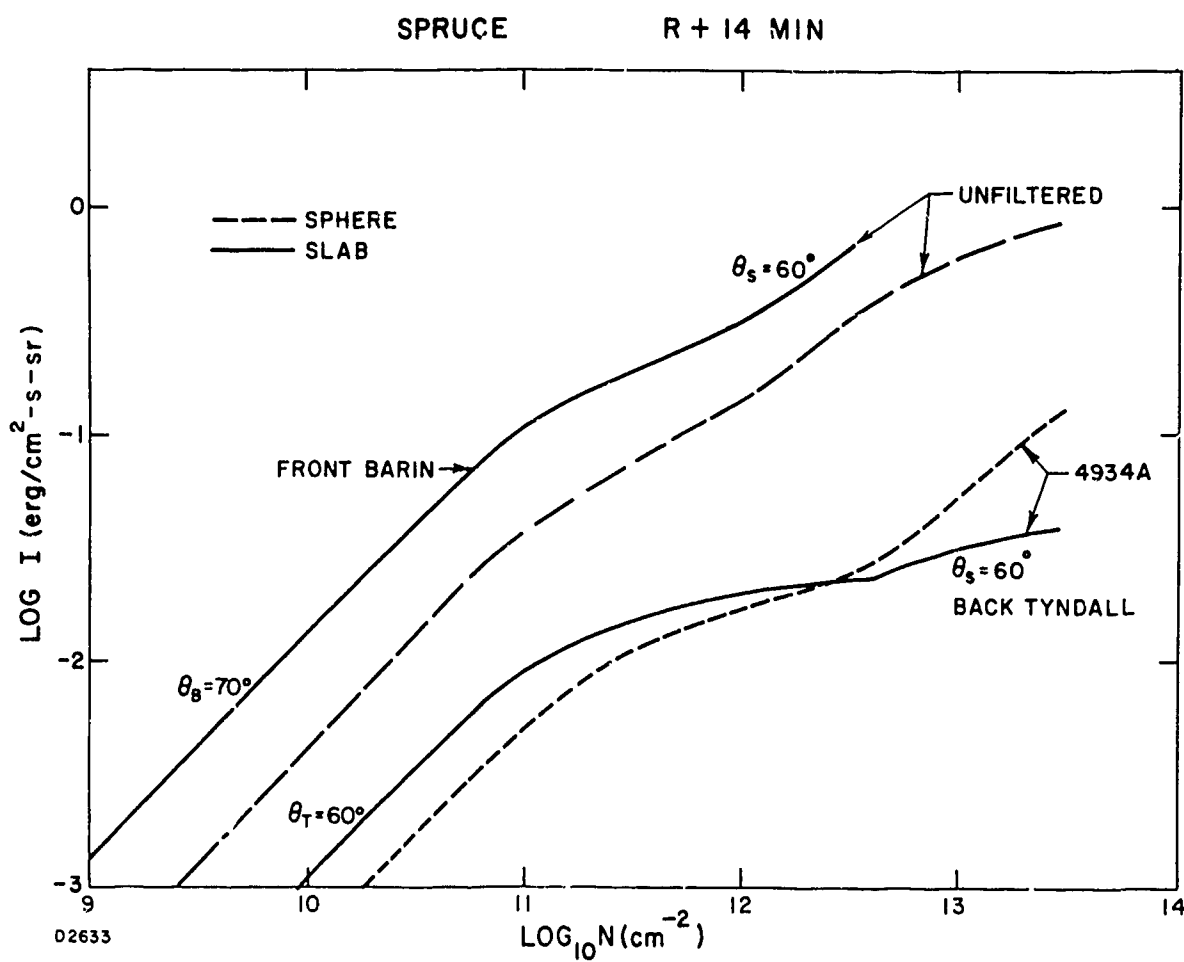
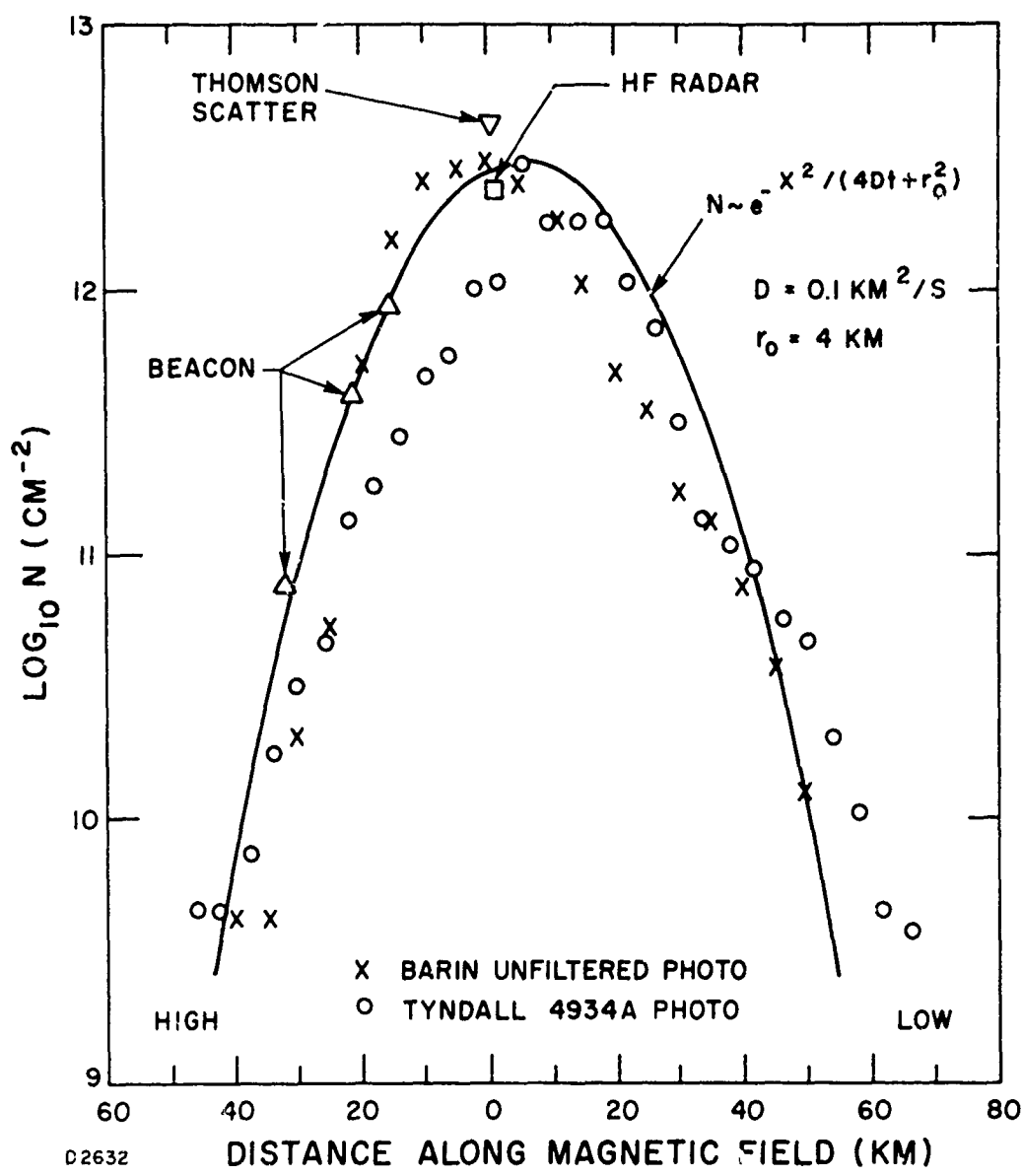


Fig. 2 Relation between intensity and ion column density.

face of the cloud and has a view angle of 60 degrees to the normal. Here again we see the effect of optical depth, the intensity starts linearly with density for the thin cloud and goes up more slowly when the cloud is optically thick. On the backside of the cloud the intensity is very insensitive to column density.

In Fig. 3 we give a correlation for Spruce at $R + 14$ min comparing column density as a function of distance along the magnetic field. The comparison is made in the striated region on the eastern part of the ion cloud. The photographic data are compared with results obtained on the Beacon experiment and from HF and Thomson scatter radar measurements. Also shown is a Gaussian correlation given as a solid line in the figure based on a diffusion coefficient of $D = 0.1 \text{ km}^2/\text{s}$ and an initial radius $r_0 = 4 \text{ km}$. The photographic data are given by the symbol \times for data from Barin in the unfiltered photograph and \circ for data from Tyndall at $\lambda = 4934\text{\AA}$. The HF radar and Thomson scatter radar data give peak densities. These are converted to column density using an effective cloud width of 5 km determined from the Beacon experiment. The data from Barin being on the solar illuminated side is the more reliable photographic data. The agreement of the data from Tyndall in the low density extremes is expected because the cloud approaches the optically thin limit; however, the agreement in the central region of the cloud is surprising in view of the insensitivity of intensity to column density. The interferometric intensity determination made near the peak of the cloud from the same side as Tyndall gives comparable intensity to the photographically determined value and hence agree with the data shown in Fig. 3.



In conclusion, when treated with care and used in a semi-empirical manner, photographic data measures ion cloud column density.

REFERENCES

1. B. Kivel and G. M. Weyl, "SECEDE II Optical and Radar Data Correlation (U)," in Proceedings of the SECEDE II Final Data Review Meeting, RADC TR-72-153, Vol. I, (Stanford Research Institute, May 1972) p. 127. (SECRET)
2. B. Kivel, in Analysis of Barium Clouds, RADC TR-71-253, Vol. I (June 1971) and RADC TR-72-103, Vol. I (January 1972), (Avco Everett Research Laboratory Semi-Annual Technical Reports).

CHAPTER 5
THEORY OF ION CLOUD DYNAMICS AND MORPHOLOGY

5. THEORY OF ION CLOUD DYNAMICS AND MORPHOLOGY

Lewis M. Linson and Gerald Meltz*

A. INTRODUCTION

There are three principal reasons for acquiring a theoretical understanding of the complex phenomena that occur when barium ion clouds are released in the ionosphere. First, so that a proper interpretation of the data can be made; second, so that future test planning can be successfully carried out; and third, so that reliable theoretical extrapolations can be made to other environments where the conditions are different from those under which barium ion clouds have been produced.

We will show that a theoretical understanding coupled with an empirical scaling of the Secede data provides a basis for making reliable predictions of the motion of barium ion clouds and the expected onset time of striations for future test planning. To extend our predictions to other environments, it is necessary to comprehend the physical mechanisms that determine the onset time of striations, the spectrum of the spatial irregularities produced by the ionization, and the time during which one could reliably expect the structured ionization to exist. A knowledge of these factors will also be useful in arriving at a model of ion-cloud/radio-wave interactions.

*Mitre Corporation, Bedford, Massachusetts

For these reasons, we shall present a rather complete but somewhat cursory review of the status of our theoretical understanding of barium ion cloud phenomenology. This section will not review all the work that has been accomplished during project Secede nor will it present lengthy derivations of the theoretical results. Instead we will give references to the original papers and reports that contain complete discussions of the assumptions and restrictions. Our intent is to limit the scope to contributions that are relevant to the Secede barium release test series. We underscore the fact that our present theoretical understanding has grown out of the contributions of a number of people and has been sharpened by the critical comments of our colleagues.

In Section B we will briefly review barium-ion-cloud phenomenology and in Section C present the model that has been the basis of much of the theoretical work. The principal large-scale effect of the three-dimensional equations is to lead to ambipolar diffusion parallel to the magnetic field. The assumptions necessary to make the transition to a two-dimensional model are reviewed. The significance of the distinction between low and high cloud conductivity, and the current flow patterns, due to the presence of the cloud and connecting to other ionospheric layers by field-aligned currents, are discussed.

Section D discusses two aspects of the large scale behavior of barium ion clouds: their motion perpendicular to the magnetic field and the several stages of deformation that ion clouds undergo. These stages include steepening of the "backside", elongation in the direction of motion, and narrowing transverse to the direction of motion. The configuration of ionization at this stage is best approximated as a thin flat sheet elongated



Fig. 1 Event Titmouse at Three Stages of Development

along the magnetic field and in the direction of the neutral wind. In Section E we review the various aspects of the fine scale structuring of the ion-cloud density that occurs on the unstable backside of the ion cloud and has the appearance of striations. These aspects include the onset time of striations, the spectrum of scale sizes produced, the nonlinear evolution of the field-aligned sheets, and the eventual dissipation of ionization. Section F concludes with a brief summary of the principal points established in this chapter and a discussion of areas where future work is needed. Several key questions remain for which present theoretical understanding has not been developed sufficiently to provide definitive answers. We stress that the reliability of predictions depends on how well some of the basic background parameters are known, e.g., neutral wind velocity, ambient electric field, and the ionospheric conductivity.

B. BARIUM-ION-CLOUD PHENOMENOLOGY

Figure 1 shows a sequence of views of Event Titmouse from a direction nearly perpendicular to the magnetic field.¹ The picture on the left shows that the ion cloud is more elongated parallel to the magnetic field in comparison with the spherical neutral cloud. The fact that the ions extend further along the field than the neutrals is due to the electron pressure adding to the ion pressure. The result is the familiar ambipolar diffusion of the ion cloud in the direction of the magnetic field. The dimension of the ion cloud transverse to the magnetic field is smaller than the neutral cloud because the perpendicular diffusion of electrons and ions is negligibly small. In the middle picture we see that the ion cloud has separated from the neutral cloud and that the ion cloud has developed a large density gradient

on its "backside"; that is, the side closest to the neutral cloud out of which the neutrals flow. On the right side of Fig. 1 we see that the backside has structured and exhibits magnetic-field-aligned striations.

It is important to recognize, when viewing photographs of barium ion clouds, that one is seeing only a projection of a diffuse distribution of ionization, very much elongated in the direction of the magnetic field. The extent of this elongation can be typically as much as 1/3 or 1/4 of the distance from the viewer. No photograph of a barium ion cloud can give a true picture of the shape of the cloud in the plane transverse to the magnetic field because only one line of sight is directly up the magnetic field line. A striation that is only 200 meters wide will appear twice as wide on a photograph if it is located as little as only 1/5 of a degree, or 600 meters, away from the magnetic field zenith. We are fortunate, as we shall see later, that three of the barium ion clouds released during the Secede II test series passed through the magnetic zenith at a time when they were fully striated. These unique views have greatly enhanced our confidence in the validity of our theoretical understanding of the complex ion cloud phenomena.

We have stressed the fact that much of what we discuss depends on a number of ambient parameters and on the size of the barium ion cloud. Of primary importance are the ambient electric field, the neutral wind velocity, and the conductivity of the ambient ionosphere. The Secede barium ion clouds were predominantly very large ion clouds in the sense that their conductivity far exceeded the height-integrated Pedersen conductivity of the ambient ionosphere. Indeed, several of the ion clouds

contained more electrons on magnetic field lines than the ambient ionosphere contained.

Figure 2 illustrates the different appearance an ion cloud may have as seen from two different sites. It presents a pair of views of the Spruce ion cloud as seen from Site C-6 on the left and from Tyndall on the right. At this time, the barium ion cloud has elongated approximately 60 km parallel to the magnetic field and 40 km in the direction of the neutral wind, but has narrowed in the direction transverse to its motion as seen in the view from Site C-6 on the left. The bulk of the unstructured ionization is indeed representable as a flat sheet. There is a complication due to the late time ionization deposited by the neutral cloud. The structured ionization represents a series of smaller sheets and rods also very much elongated in the direction of the magnetic field.

We now turn to a description of the model that has been the basis for most of the theoretical work.

C. BASIC MODEL

1. Formulation of the Problem

Ion cloud drift, deformation and structuring are all determined by the delicate balance that exists between drag forces, due to ion-neutral collisions, and magnetic forces that are generated by Pedersen currents driven by the dynamo action of the wind-blown barium plasma. These currents which flow across the cloud, normal to the magnetic field, depend on the ratio of the height-integrated perpendicular (Pedersen) conductivity within the cloud to the background height-integrated ionospheric conductivity. This ratio determines to what extent the dynamo fields will be reduced, or



Fig. 2 Simultaneous Photographs of Event Spruce at R + 19 Minutes Seen From Site C-6 on the Left and from Tyndall on the Right (Technology International Corporation)

screened, by polarization of the cloud. A highly conducting background will drain any charge accumulations through parallel electron currents; a poorly conducting ionosphere will permit polarization charges to accumulate and thus greatly reduce the difference between the velocity of neutrals, \vec{V}_n , and barium ions, \vec{V}_i . Variations in the current flow within the inhomogeneous cloud will result in relative motion of the dense regions and hence deformation of the initial ion density distribution.

A low density ion cloud will be unscreened by polarization fields and will stand still or drift with the ionosphere as viewed in the earth's frame, and essentially maintain its initial distribution by expanding in a self-similar manner through ambipolar diffusion both parallel and perpendicular to the magnetic field. Regardless of the density in the ion cloud, steady state never is achieved nor is it theoretically realizable.² The time scales for most particle interactions, or collisions, are generally much shorter than the time scales for deformation and striation formation and development. As a result, inertial effects are seldom of importance in describing ion cloud behavior.

Drift and deformation are large scale phenomena that can be described in relatively simple terms as compared to striation formation and morphology which depend on the details of the barium cloud-ionospheric interaction. Although the same elements enter into an understanding of why striations develop, steepen, and bifurcate, these processes are complicated by the need to consider the finite, albeit large, parallel conductivity and the small perpendicular electron diffusion.

We develop in this section the fundamental fluid equations that govern ion cloud behavior. Subject to the assumptions discussed below,

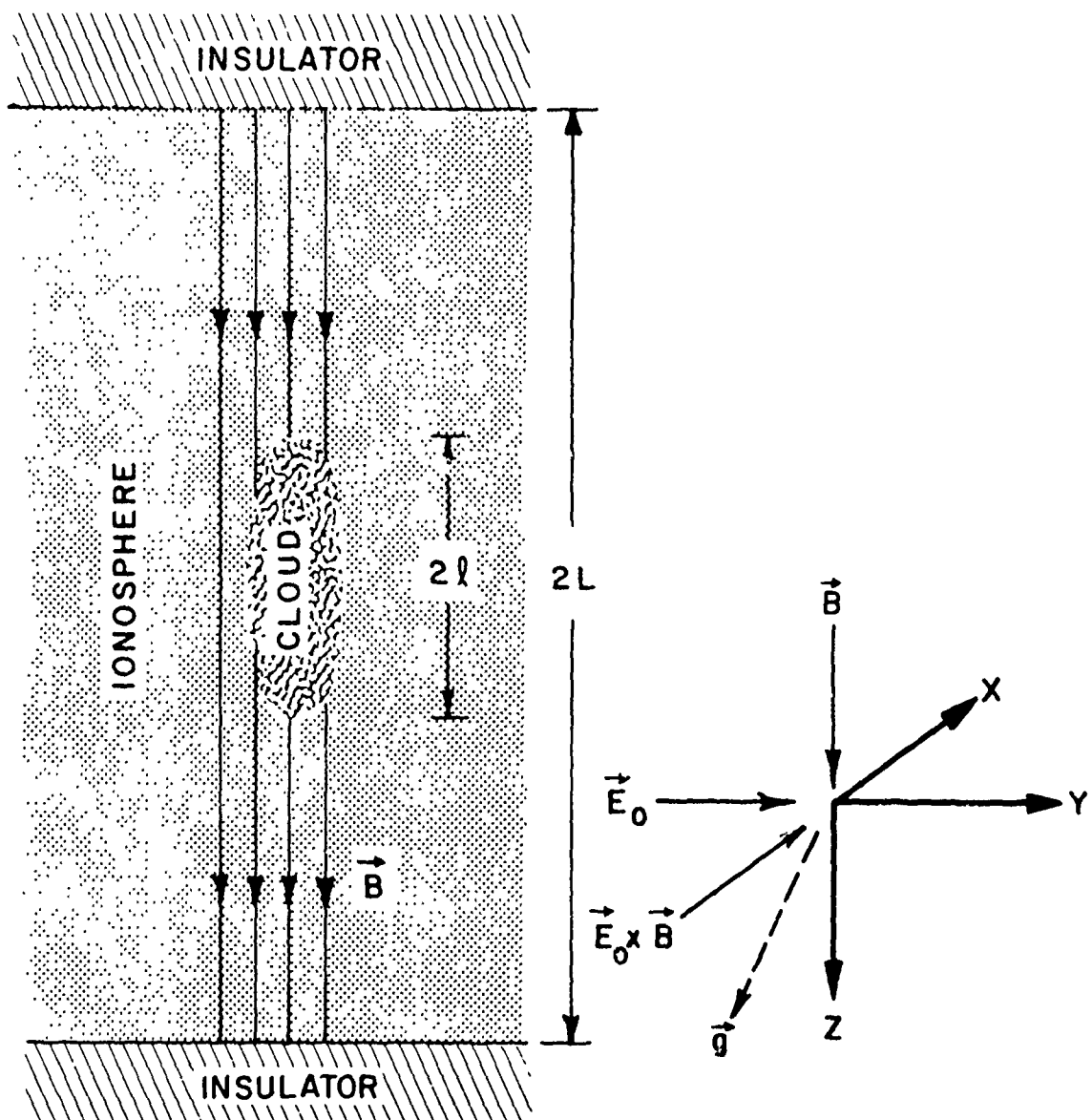
these equations can be reduced to two basic relationships: 1) An equation stating the zero divergence of the total current consisting principally of the ion Pedersen current (including the contributions of gravitational and pressure gradient drifts) perpendicular to the magnetic field and electron current along the field; and 2) the electron continuity equation which shows that the electron density changes because of $\vec{E} \times \vec{B}$ drifts, perpendicular and parallel diffusion, and the divergence of electron current flow along \vec{B} .

We further show that to lowest order in $(\kappa_e \kappa_i)^{-1}$ (κ_e and κ_i are the ratios of angular gyrofrequency to collision frequency for electrons and ions respectively), the problem can be reduced to a determination of parallel drift (due to gravity) and ambipolar diffusion along the field lines, plus a description of the change in column density brought about by incompressible $\vec{E} \times \vec{B}$ convection. The effective electric field is composed of the ambient field (in the frame of the neutrals), \vec{E}_o , a contribution due to gravity, $\tau \vec{g} \times \vec{B}$, and a polarization field, \vec{E}_p , generated by the presence of the cloud, and τ is the barium ion-neutral collision time.

a) Assumptions

We consider an isothermal, inhomogeneous plasma cloud in a finite, uniform ionosphere. The ionosphere is terminated by insulating boundaries that model the effect on the current flow of the unionized lower atmosphere and the collisionless topside protonosphere. A uniform magnetic field threads the cloud and its surroundings and is perpendicular to the boundaries. Gravity, which acts only on the ions, has both a perpendicular and parallel component as indicated in Fig. 3.

We assume that the ambient electric field and the neutral wind are constant and uniform. All changes in ion cloud dynamics due to image



D3515

Fig. 3 Plasma Cloud-Ionosphere Model

motions in the ionosphere subtended by the cloud and the generation of these ionospheric perturbations will be neglected. Large clouds are probably not affected by the secondary fields generated in this fashion although the lower ionosphere may be greatly modified on the field line below the cloud.

Our concern will be with low β , weakly ionized plasmas that change slowly compared to particle collision times. Inertial terms in the equations of motion will be small under these circumstances and can be neglected except at very high altitudes. Generally, finite Larmor radius effects can also be neglected although they too may be important at very high altitudes. Both inertial effects³ and the effective "kinematic viscosity"⁴ associated with the complete ion pressure tensor modify the dispersion relation for the gradient-drift instability and set a threshold for growth in the limit of collisionless ions.

At altitudes where large ion yields are attainable, collisions between electrons and neutrals or ions are extremely infrequent on the time scale of an electron gyro period. Ion collisions are more numerous on a corresponding time scale although they, too, are infrequent. As a result parallel diffusion coefficients and conductivities far exceed perpendicular transport properties and Pedersen currents always dominate Hall currents. If we denote the ratio of an angular cyclotron frequency to a collision frequency by $\kappa = \Omega \tau$, then for case of interest

$$\kappa_{en} \geq \kappa_{ei} \gg \kappa_i \geq 1.$$

Although these quantities are functions of altitude, we will in general neglect these variations, taking the neutral atmosphere to be of constant density. A relaxation of this assumption will be made in the discussion of ambipolar diffusion along the magnetic field.

b) Three-Dimensional Equations of Motion

We choose a rectangular coordinate system in the frame of the neutrals with the z-axis pointed along the magnetic field \vec{B} and the y-axis aligned with \vec{E}_o , the ambient electric field, as shown in Fig. 3. This system translates, as viewed in the earth's frame, with the velocity of the neutral wind, \vec{V}_n . In this frame \vec{E}_o is the sum of the ambient ionospheric field \vec{E}_a (in the earth's frame) and $\vec{V}_n \times \vec{B}$ associated with the moving reference system,

$$\vec{E}_o = \vec{E}_a + \vec{V}_n \times \vec{B}.$$

Electron and ion drag are balanced in the quasistatic moment equations by the conservative forces $\vec{F}_{e,i}$ and the magnetic component of the Lorentz force:

$$\vec{F}_e - \vec{V}_e \times \hat{b} = \kappa_{en}^{-1} \vec{V}_e + \kappa_{ei} (\vec{V}_e - \vec{V}_i). \quad (1)$$

$$\vec{F}_i + \vec{V}_i \times \hat{b} = \kappa_i^{-1} \vec{V}_i. \quad (2)$$

The "forces" are given by

$$\vec{F}_e = - \frac{\vec{E}}{B} - \frac{T}{eBn} \nabla n, \quad (3)$$

$$\vec{F}_i = \frac{\vec{E}}{B} - \frac{T}{eBn} \nabla n + \frac{1}{\Omega_i} \vec{g}, \quad (4)$$

where $\hat{b} = \vec{B}/B$ is a unit vector in the direction of the magnetic field and \vec{E} is the sum of the ambient and cloud generated fields, $\vec{E}_o + \vec{E}_p$. The common electron and ion temperature is expressed in energy units.

In addition, we require quasineutrality

$$n_i \approx n_e = n \quad (5)$$

and solenoidal current flow

$$\nabla \cdot \vec{J} = e \nabla \cdot (\vec{\Gamma}_i - \vec{\Gamma}_e) = 0 \quad (6)$$

where $\vec{\Gamma}_i$ and $\vec{\Gamma}_e$ are the ion and electron fluxes, respectively. Two other equations are needed, electron continuity

$$\frac{\partial n}{\partial t} + \nabla \cdot \vec{\Gamma}_e = 0 \quad (7)$$

and

$$\nabla \times \vec{E} = 0. \quad (8)$$

Equation (8) implies the existence of a scalar potential ϕ such that

$$\vec{E} = -\nabla \phi \quad (9)$$

Note that ϕ includes an ambient contribution $-\vec{E}_0 \cdot \vec{x}$. Before proceeding further it is useful to separate ϕ into components due to ambipolar parallel diffusion and gravitational fall and a potential $\bar{\phi}$ that drives currents along and normal to \vec{B} . Thus

$$\phi = \bar{\phi} + \frac{T(1-\Delta)}{e(1+\Delta)} \ln \frac{n}{n_a} + \frac{Mg_{||}\Delta}{e(1+\Delta)} z \quad (10)$$

where $\Delta = \kappa_i / \kappa_{en} \ll 1$ and n_a is the ambient ionospheric density. Zabusky et al⁵ have derived the expressions for the parallel and perpendicular fluxes in terms of $\bar{\phi}$ and $\nabla n/n$. By substituting into Eq. (6) and then deleting small terms on the order of κ_i^{-1} , Δ , and κ_i / κ_e , they have derived the following simplified equation for the potential $\bar{\phi}$:

$$\nabla_{\perp} \cdot n \nabla_{\perp} \phi - \tau \vec{g} \times \vec{B} \cdot \nabla_{\perp} n + \frac{2T}{e} \nabla_{\perp}^2 n + \kappa_i \nabla_{||} n \kappa_e \nabla_{||} \bar{\phi} = 0 \quad (11)$$

This equation states that the divergence of the ion Pedersen current and transverse gravitational and pressure gradient drifts must be balanced by electron current flow along \vec{B} .

The electron continuity equation (7) can also be simplified by eliminating the $\nabla_{\perp} \cdot n \nabla_{\perp} \bar{\phi}$ term by using Eq. (11). The result is

$$\begin{aligned} \frac{\partial n}{\partial t} - \frac{1}{B} \nabla_{\perp} n \cdot \nabla_{\perp} \bar{\phi} \hat{b} + g_{||} \nabla_{||} \tau n - \frac{2T}{eB} \nabla_{||} \kappa_i \nabla_{||} n \\ - \frac{2T}{eB} \nabla_{\perp} \kappa_{ei}^{-1} \nabla_{\perp} n + \frac{1}{B} \nabla_{||} n \kappa_e \nabla_{||} \bar{\phi} = 0. \end{aligned} \quad (12)$$

This equation states that changes in the electron density are due to $\vec{E} \times \vec{B}$ drifts, gravitational fall, parallel and perpendicular diffusion and the divergence of the electron current along the magnetic field.

These equations can be reduced to a particularly simple and useful form by neglecting diffusion (low temperature limit) and gravity and assuming that the potential is constant along field lines. With these restrictions, which will be discussed in the next section, Eqs. (11) and (12) become

$$\nabla_{\perp} \cdot n \nabla_{\perp} \bar{\phi} = 0 \quad (13)$$

and

$$\frac{\partial n}{\partial t} - \frac{1}{B} \nabla_{\perp} n \cdot \nabla_{\perp} \bar{\phi} \times \hat{b}. \quad (14)$$

If we introduce a new potential ψ defined by

$$\bar{\phi} = \psi - \vec{E}_o \cdot \vec{x}_{\perp}$$

and integrate Eq. (13) along \vec{B} , then

$$\nabla_{\perp} \cdot (N \nabla_{\perp} \psi) = \vec{E}_o \cdot \nabla_{\perp} N. \quad (15)$$

This Poisson type equation determines the polarization fields in terms of the ratio N/N_o where $N = \int_{-L}^L n dz$ and N_o is the ambient ionospheric column density. The integral of Eq. (14) yields

$$\frac{\partial N}{\partial t} + (\vec{U}_o - \nabla \psi \times \hat{b}/B) \cdot \nabla N = 0 \quad (16)$$

which describes an incompressible plasma motion with the local $\vec{E} \times \vec{B}/B^2$ velocity and \vec{U}_o is simply the ambient $\vec{E}_o \times \vec{B}/B^2$ drift. Alternatively, we could have written Eqs. (15) and (16) as

$$\nabla \cdot N \vec{E} = 0, \quad (17)$$

$$\frac{\partial N}{\partial t} + \frac{\vec{E} \times \vec{B}}{B^2} \cdot \nabla N = 0. \quad (18)$$

a form used extensively in later sections.

Parallel diffusion can be introduced by assuming a separable density

function and noting that

$$n(x, y, z) = f(z) N(x, y).$$

Then one finds from Eq. (12) that f must satisfy the generalized one-dimensional ambipolar diffusion equation

$$\frac{\partial f}{\partial t} + g_{||} \frac{\partial}{\partial z} \tau f - \frac{2T}{eB} \frac{\partial}{\partial z} \kappa_i \frac{\partial}{\partial z} f = 0. \quad (19)$$

c) Simplifying the Model

An important simplification⁵ is achieved by recognizing that the large parallel conductivity implies nearly constant potentials along the field lines. We assume that $\bar{\phi}$ can be expanded in powers of $(\kappa_e \kappa_i)^{-1}$; thus

$$\bar{\phi} = \bar{\phi}^{(0)} + \frac{1}{\Lambda} \bar{\phi}^{(1)}$$

where $\Lambda = \kappa_e \kappa_i$ is treated as a constant. From the potential Eq. (11) in lowest order, we find

$$\frac{\partial}{\partial z} n \frac{\partial}{\partial z} \bar{\phi}^{(0)} = 0. \quad (20)$$

Since the insulating boundary conditions require $\nabla_{||} \bar{\phi} \Big|_{L, -L} = 0$, Eq. (20) implies $\nabla_{||} \bar{\phi}^{(0)} \equiv 0$. Thus the first order potential equation becomes

$$\nabla_{\perp} \cdot (n \nabla_{\perp} \bar{\phi}^{(0)}) - \nabla_{\perp} n \cdot (\tau \vec{g} \times \vec{B}) + \frac{2T}{e} \nabla_{\perp}^2 n + \frac{\partial}{\partial z} \left(n \frac{\partial \bar{\phi}^{(1)}}{\partial z} \right) = 0. \quad (21)$$

If we integrate Eq. (21) along \vec{B} and note that $\nabla_{\parallel} \bar{\phi}^{(1)}$ vanishes at the boundaries then we obtain

$$\nabla_{\perp} \cdot (N \nabla_{\perp} \bar{\phi}^{(0)}) - \nabla N \cdot \tau g \times \vec{B} + \frac{2T}{e} \nabla_{\perp}^2 N = 0 \quad (22)$$

where the electron column density $N = \int_{-L}^L n dz$ is proportional to the height-integrated Pedersen conductivity \sum_p since κ_i and κ_e are assumed to be constant.

We introduce a polarization potential ψ through

$$\bar{\phi}^{(0)} = \psi - \frac{2T}{e} \ln \frac{N}{N_0} - \vec{E}_0 \cdot \vec{x}_{\perp} \quad (23)$$

where N_0 is the ambient electron column density which is proportional to \sum_p^a , the ambient integrated Pedersen conductivity. Combining Eqs. (22) and (23) we obtain the basic two-dimensional potential equation

$$\nabla_{\perp} \cdot (N \nabla_{\perp} \psi) = \vec{E}^* \cdot \nabla_{\perp} N \quad (24)$$

where

$$\vec{E}^* = \vec{E}_a + \vec{V}_n \times \vec{B} + \tau g \times \vec{B}$$

is an effective background field----the source of transverse Pedersen currents. The potential ψ extends beyond the cloud but becomes vanishingly small at large distances. Note that the perpendicular component of gravity can also drive currents. In fact it acts like an electric field in the potential equation of magnitude τgB which for barium ions is about 0.3 mV/m at midlatitudes and altitudes of 185 km.

We can proceed the same way with the electron continuity equation, noting that $\nabla_{||} n \Big|_{-L}^L$ and n vanish at the boundaries, to obtain the second basic relationship

$$\frac{\partial N}{\partial t} + \frac{(\vec{E}_o - \nabla \psi) \times \hat{b}}{B} \cdot \nabla N = 0 \quad (25)$$

or re-expressed in terms of $\vec{E} = \vec{E}_o - \nabla \psi$,

$$\frac{\partial N}{\partial t} + \frac{\vec{E} \times \vec{B}}{B^2} \cdot \nabla N = 0. \quad (26)$$

Since

$$\frac{dN}{dt} = \frac{\partial N}{\partial t} + \vec{v} \cdot \nabla N,$$

the preceding equations imply that the column density is incompressible and hence that deformations are caused by the relative $\vec{E} \times \vec{B}$ convection of various parts of the cloud.

To summarize, we find that ion cloud drift and deformation can be described by parallel diffusion and incompressible convection. It can be shown that if we assume that the plasma density is separable, then $\bar{\delta}$ ⁽¹⁾ is also vanishingly small. Rigorously, our model does not lead to a separable z -dependence. However if the Pedersen conductivity of the cloud dominates the background then the z -dependence of n will be nearly separable within the cloud and the ambient plasma will produce the parallel-resistivity effects. Thus, the density variation along the magnetic field follows from the one-dimensional parallel diffusion equation (19) with gravitational fall which has been studied by Bannister and Davis⁶ and applied to barium plasma clouds by Pendya⁷ as discussed in Chapter 1 of this report.

d) Parallel and Perpendicular Diffusion

An extensively studied feature of barium ion cloud behavior is the ambipolar diffusion of the ions parallel to the magnetic field. The parallel diffusion coefficient (cf. Eq. (19)) is given by

$$D_{\parallel} = \frac{(T_e + T_i)}{M_i} \tau = \frac{T_e + T_i}{eB} \kappa_i \quad (27)$$

so that its measurement yields an estimate for the barium ion-nitrogen collision time, τ . Measurements have yielded collision times in agreement with earlier classical measurements of barium ion mobility in nitrogen.⁸ At altitudes around 185 km, the effective collision time is approximately 0.7 s and we obtain a value of 25 for the product of the ion gyrofrequency and the ion-neutral collision time, $\kappa_i \equiv (\Omega\tau)_i$. The perpendicular diffusion coefficient based on the measured κ_i is several orders of magnitude smaller than the parallel diffusion coefficient and can be taken to be zero as far as large scale motion of ion clouds is concerned. We shall see later that the value of the perpendicular diffusion coefficient is exceedingly important in determining the striation scale size and lifetime.

A number of optical analyses have yielded a parallel diffusion constant of $0.1 \text{ km}^2/\text{s}$ at altitudes around 185 km. Figure 4, taken from Ref. 20, shows the agreement between the observed ion cloud thickness along \vec{B} as inferred from Thomson scatter measurements at Site C-6 and the calculated value based on a solution of the one-dimensional diffusion equation. The agreement is excellent for the first 10 or 15 minutes for both Event Spruce and Event Olive I. At later times, the Thomson scatter radar line of sight through the ion cloud was not parallel to \vec{B} .

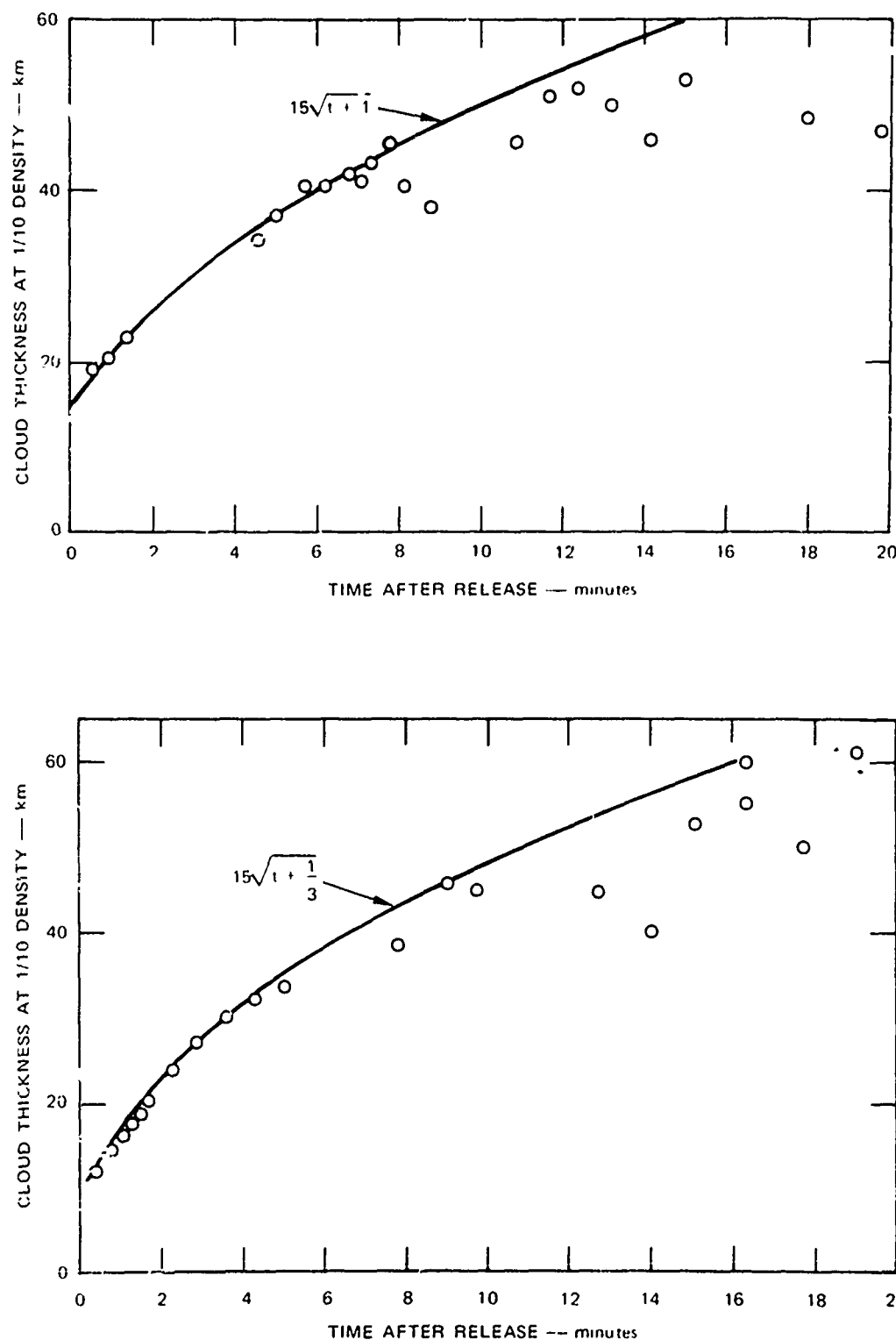


Fig. 4 Comparison of the Olive and Spruce Ion Cloud Thicknesses in the Direction of the Magnetic Field as Obtained by the Thomson Scatter Radar Shown by the Open Circles and the Solid Theoretical Curves Based on Ambipolar Diffusion Parallel to the Magnetic Field

The lack of diffusion perpendicular to the magnetic field implies that in a uniform atmosphere the maximum electron density in the ion cloud should decrease as $t^{-1/2}$ in accord with one-dimensional parallel diffusion. The general behavior of the peak electron density as a function of time is in broad agreement with this prediction. In an exponential atmosphere, the decrease in the peak density is limited because the cloud comes into diffusive equilibrium. The bottom side of the ion cloud will become very flat while the topside becomes broader than a gaussian. In addition, gravity, a downward or northward component of the neutral wind, or a westward component of the electric field will cause the location of the peak electron density to descend. The change in altitude will result in a compression of the ion density profile since the neutral-atmosphere scale-height is smaller at lower altitudes. These effects are illustrated in Fig. 5 taken from Ref. 7. Not shown in this figure, but discussed in detail in Chapter 1 of this report, is the fact that the peak electron density can slowly increase as the ion cloud descends in altitude. Figure 5 was drawn under the assumption that the vertical drift due to the neutral wind and electric field effects was constant in altitude.

Let us turn to the question of the value of the diffusion coefficient perpendicular to the magnetic field. The cloud generated electric field, which generally extends beyond the cloud boundaries, determines the dominant diffusion. It has been shown to first order in $(\kappa_e \kappa_i)^{-1}$ and for large ratios of cloud to background height-integrated Pedersen conductivities (see Eq. (12)) that perpendicular diffusion proceeds at a very slow rate controlled by electron collisions. A low cloud density expansion due to Simon⁴ leads to the result that the perpendicular diffusion is controlled by ions.

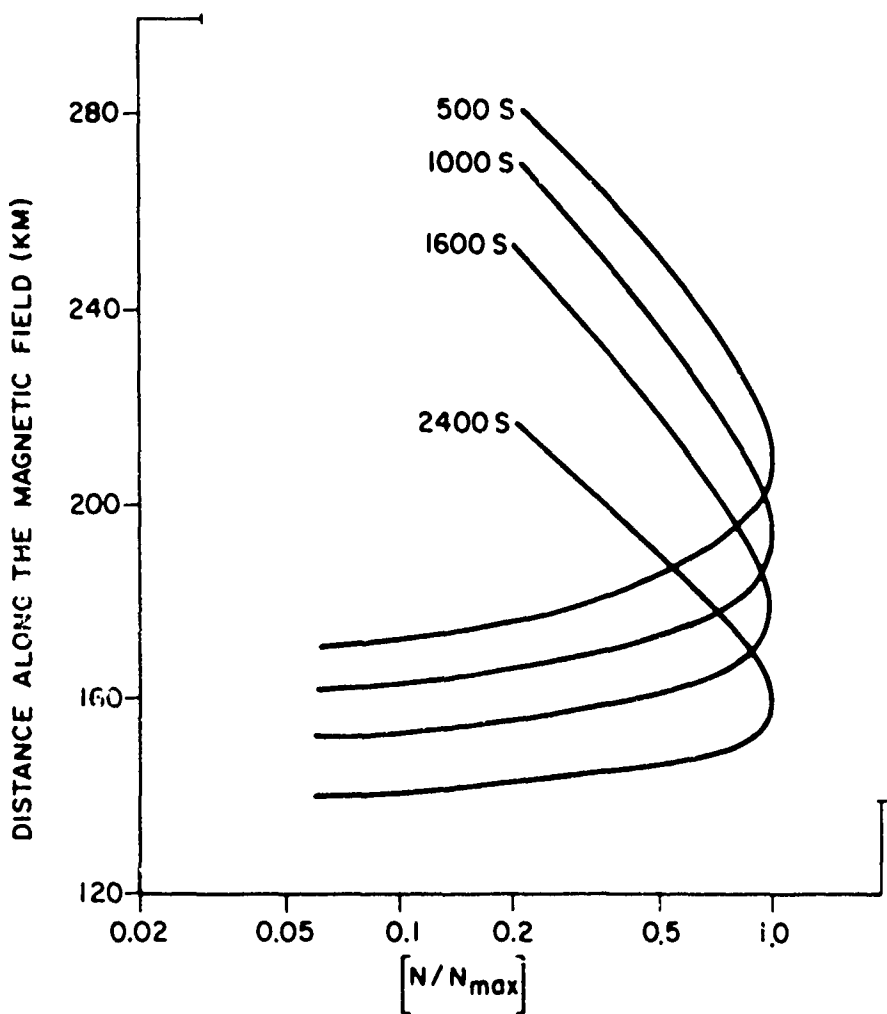


Fig. 5 Diffusive Equilibrium Electron-Concentration Distributions Along the Earth's Magnetic Field

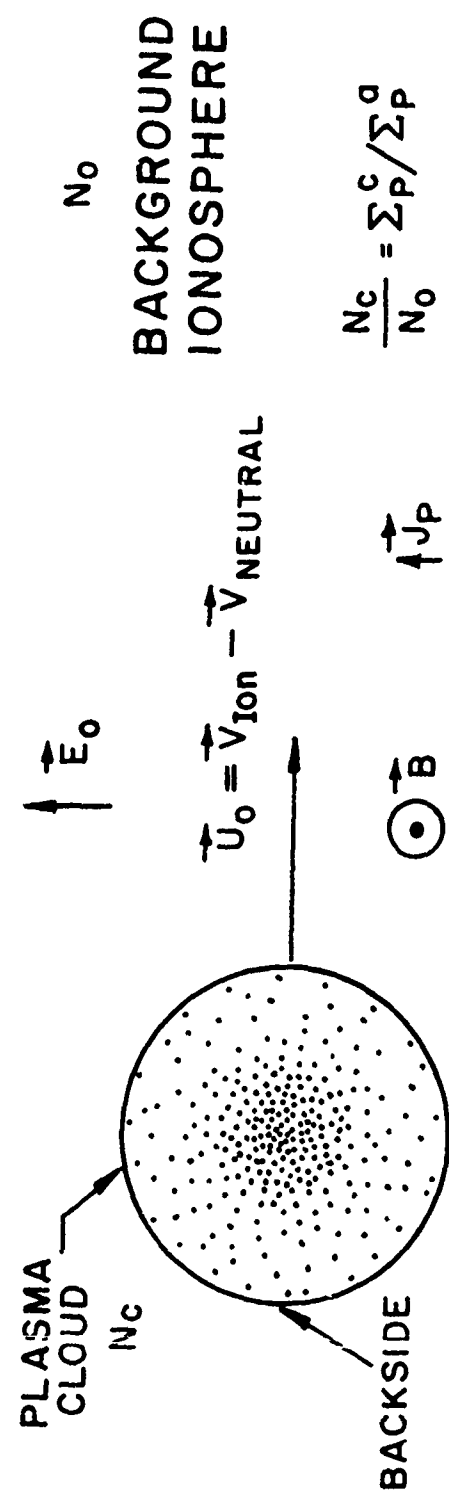
Simon's solution is valid as long as the changes in electron density which occur as a result of the higher-order electric field do not give rise to a large change in the zero-order electric field.

2. Two-Dimensional Model

a) Incompressible Convection

We turn our attention to the dynamics of barium ion clouds in the plane transverse to the magnetic field. These dynamics are best studied by the system of coupled nonlinear two-dimensional equations (15) and (16) derived from the moment equations by integrating parallel to the magnetic field. These equations can also be obtained by starting with simplified equations of motion for electrons and ions in the limit of zero electron collision frequency. The resulting two-dimensional equations express the conservation of electron flow and zero divergence of the total current. In a purely two-dimensional model everything is uniform parallel to the magnetic field and there is no flow of either species in the vertical direction. However, the same two-dimensional equations also represent the limit of vanishingly small parallel resistivity in which the electrons are allowed to flow freely up and down the magnetic field lines but ions are restrained to flow perpendicular to the magnetic field in response to the transverse electric fields.

Figure 6 shows a schematic of the cross section of the ion cloud in the plane perpendicular to the magnetic field. The ion cloud is moving to the right with respect to the neutrals. In the two-dimensional model, the ratio of height-integrated conductivities; Σ_p^c / Σ_p^a , can be represented as the ratio of the cloud center density, N_c , to the ambient ionospheric density, N_o . Due to the slow rate of development of the ion cloud and the



C5554 -1

Fig. 6 Simple Two-Dimensional Model

small plasma pressure relative to the magnetic field pressure (low β), the ambient electric fields are electrostatic as expressed by the condition $\nabla \times \vec{E} = 0$. Since the electrons do not experience any collisions they flow at the local $\vec{E} \times \vec{B}/B^2$ velocity. The flow of the ionization is incompressible as shown in Section C. 1. The fact that the flow is incompressible is extremely important in theoretically determining the behavior of barium ion clouds. This assumption precludes the possibility of an electron density increase. The ion motion closely follows the electron motion but the ions do have a component of velocity in the direction of the electric field as a result of collisions with the neutrals. At high altitudes the ion velocity with respect to the neutrals is given approximately by

$$\vec{V}_i = \frac{\vec{E} \times \vec{B}}{B^2} + \frac{1}{\kappa_i} \frac{\vec{E}}{B}. \quad (27)$$

The simple set of coupled nonlinear differential equations that describe the motion of barium ion clouds transverse to the magnetic field are repeated here

$$\frac{\partial N}{\partial t} + \frac{\vec{E} \times \vec{B}}{B^2} \cdot \nabla N = 0; \quad (28)$$

$$\nabla \cdot \vec{J}_p \propto \nabla \cdot \vec{N} \vec{E} = 0; \quad (29)$$

$$\nabla \times \vec{E} = 0. \quad (30)$$

Equation (28) is the continuity equation for the incompressible flow of the electrons at the local $\vec{E} \times \vec{B}/B^2$ velocity. Equation (29) describes the conservation of the current flow perpendicular to the magnetic field in the ionosphere and Eq. (30) is the quasistatic assumption of the low- β approximation. The Pedersen current, \vec{J}_p , is proportional to the product of the conductivity, N (proportional to the ion density) and the electric field, \vec{E} , all measured in the frame of the ambient neutrals.

Three different approaches have been used successfully to obtain information about the nature of the solutions. A number of analytical studies have been carried out^{3, 4, 5, 9, 10, 11} and numerical calculations have been used.¹² A third method involves the use of a hydrodynamic analog¹³ discussed below. This experiment has been particularly instructive in regard to the detailed structure of striation development.

b) The Hele-Shaw Cell

A variable-density but incompressible fluid confined between two closely spaced plates and moving under the influence of gravity, Fig. 7 obeys the following momentum equation in the quasi-steady limit:

$$-\frac{1}{\rho} \nabla p + \eta \nabla^2 \vec{u} + \vec{g} = 0$$

where p is the pressure, ρ the fluid density, η the kinematic viscosity and \vec{u} the fluid velocity. For small plate separation the viscous drag may be estimated by

$$\eta \nabla^2 \vec{u} \approx -8\eta \vec{u}_c / D^2$$

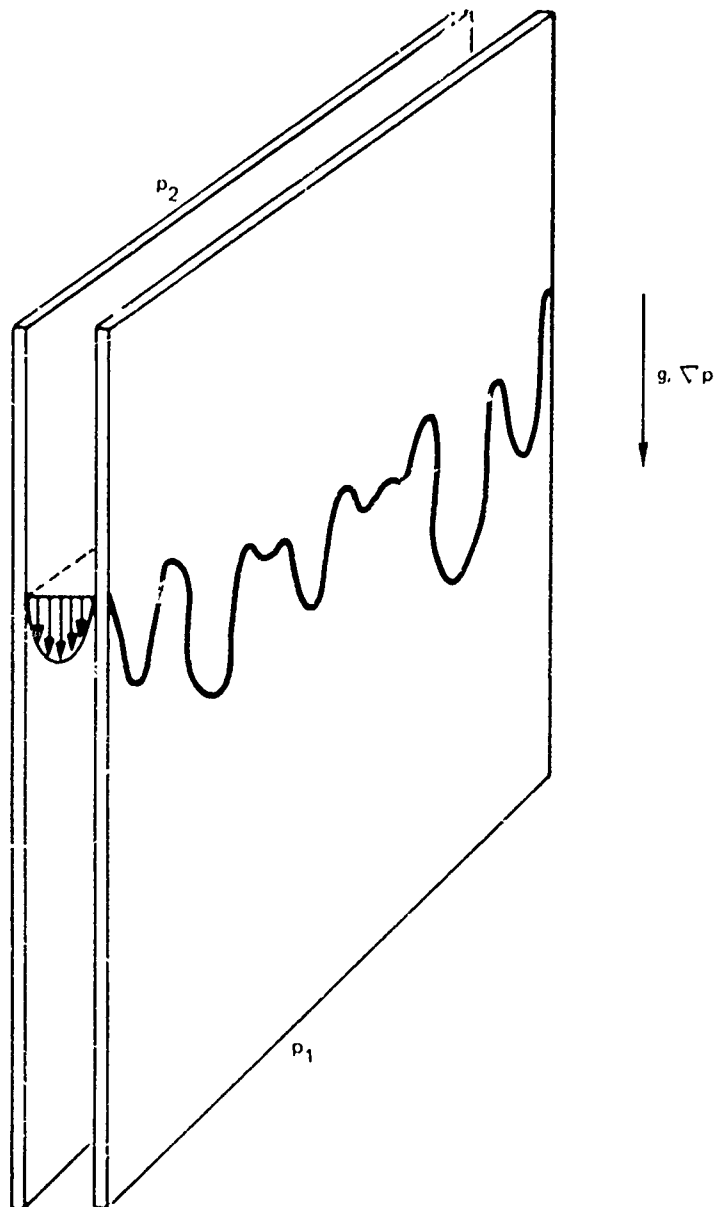


Fig. 7 The HELE-SHAW Cell (Physical Dynamics, Inc.)

where \vec{u}_c is the midplane velocity and D is the plate spacing. Since the fluid is incompressible ($\nabla \cdot \vec{u} = 0$) there exists a two-dimensional stream function $\xi(x, y)$ such that

$$\vec{u} = -\nabla \times (\xi \hat{b})$$

where \hat{b} is a unit vector perpendicular to the plate. It follows from this relation that

$$\nabla_{\perp} \cdot (\rho \nabla_{\perp} \xi) = \nabla \rho \times \left(\frac{D^2 g}{8 \eta} \right) \cdot \hat{b}$$

and

$$\frac{\partial \rho}{\partial t} + \vec{u} \cdot \nabla \rho = 0$$

If we neglect gravity and write Eq. (24) in the frame where the ambient \vec{E} field vanishes with $\vec{E}^* = \vec{V}_n \times \vec{B}$, we obtain

$$\nabla_{\perp} \cdot (N \nabla_{\perp} \Phi) = (\nabla_{\perp} N \times \vec{V}_n) \cdot \hat{b}$$

where \vec{V}_n is the uniform neutral wind and $\Phi = \psi/B$. This equation is in exactly the same form as the fluid motion relationship above. Thus the correspondence shown in Table I can be drawn.¹³

c) Ionospheric Currents

When the barium ion cloud is considered to be of finite extent parallel to \vec{B} , currents flowing in the ionosphere below the cloud are affected by the presence of the ion cloud and give rise to currents flowing parallel to the magnetic field.

TABLE I
DUALITY BETWEEN HELE-SHAW CELL AND SIMPLIFIED
TWO-DIMENSIONAL MODEL OF AN ION CLOUD

Fluid	Plasma [in drift frame ($E_\infty = 0$)]
$\hat{b} \nabla_\perp \cdot (\rho \nabla_\perp \xi) = \nabla \rho \times \frac{D^2 \vec{g}}{8\eta}$ $\vec{u} = -\nabla \times (\xi \hat{b})$	$\hat{b} \nabla_\perp \cdot (N \nabla_\perp \Phi) = \nabla_\perp N \times \vec{V}_n$ $\vec{u} = -\nabla \times (\Phi \hat{b})$
$\frac{\partial \rho}{\partial t} + \vec{u} \cdot \nabla_\perp \rho = 0$	$\frac{\partial N}{\partial t} + \vec{u} \cdot \nabla_\perp N = 0$
Boundary condition at ∞ $\vec{u} = 0; \xi = \text{constant}$	Boundary condition at ∞ $\vec{u} = 0; \Phi = \text{constant}$

Density (ρ)	Electron Column Density (N)
Fluid velocity (\vec{u})	Plasma velocity (\vec{u})
"Free-fall" velocity ($D^2 \vec{g}/8\eta$)	Neutral wind velocity in the drift frame (\vec{V}_n)
Stream function (ξ)	Electric potential Φ/B

In Fig. 8 we indicate qualitatively the effect that the presence of the highly conducting barium ion cloud has on the current flow pattern in the ionosphere. Figure 8a is a schematic diagram in the plane perpendicular to the magnetic field showing the distortion of the current flow due to the presence of the more conducting ion cloud. In a completely two-dimensional model this same current flow pattern would exist at every altitude parallel to the magnetic field and drift as a "current cell" with the $\vec{E} \times \vec{B}/B^2$ velocity. That situation is shown schematically in Fig. 8b which represents a cut in the yz plane through the center of the ion cloud. Note that the current density in the ion cloud is larger than in the less dense ionosphere. From Fig. 8a we see that this increase results from the concentration of the current in the ion cloud.

In Fig. 8c the horizontal currents are the ion Pedersen currents whereas the parallel currents are due to electrons flowing along the magnetic field. Figure 8d represents a generalization to a three-layered ionospheric model. The more conducting layer at the top of this figure represents a conjugate ionosphere which may be highly conducting and therefore can contribute a large perpendicular current density. Again the presence of a conducting ion cloud in the local ionosphere can effect the current flow in the conjugate ionosphere since electron currents flow freely along the magnetic field through the magnetosphere.

While it is recognized that the diagrams given in Fig. 8c and 8d are qualitatively correct insofar as they indicate current flow in different layers of the ionosphere, they are strictly correct only if (1) there is no

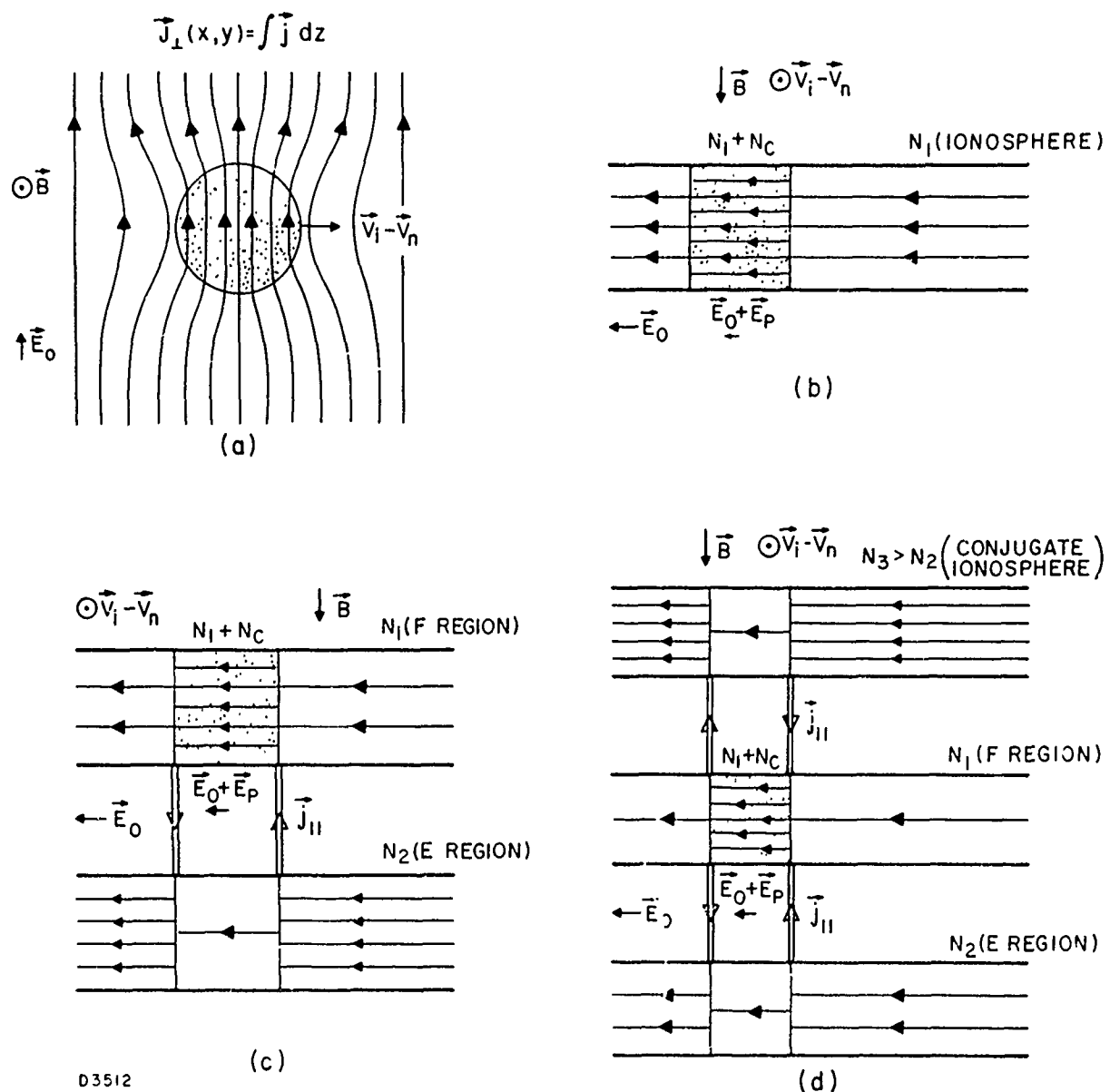


Fig. 8 Changes in the Ionospheric Current Flow Due to the Presence of a Highly Conducting Barium Ion Cloud; a) Height-Integrated Current Density Flowing Perpendicular to the Magnetic Field; This Same Pattern Results in the Cases of b) a One-Layered Ionosphere, c) a Two-Layered Ionosphere, and d) Local Plus Conjugate Ionosphere

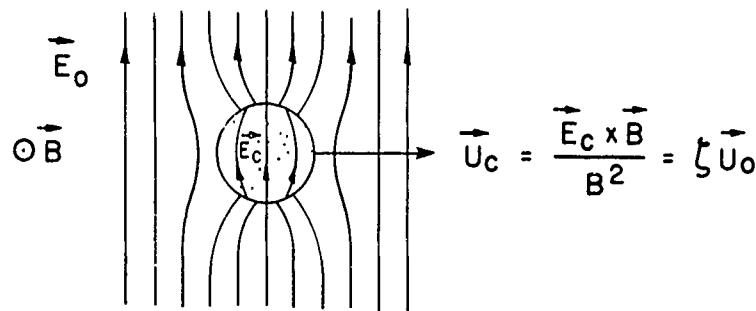
distinction between the barium ions and the ambient ionospheric ions; (2) if the neutral density is the same in all three layers; and (3) if the electric field which drives the currents is externally imposed on the complete system. The actual interaction of several different layers in the ionosphere with a barium ion cloud is only now beginning to be considered¹⁴ and is a very complex problem. It is clear that the plasma density will be increased where the electrons flow into the lower ionosphere and decreased where electrons leave to neutralize the charge accumulation in the cloud. Thus the ionosphere subtended by the cloud will be locally perturbed and this perturbation will move with the cloud.

We can see qualitatively that the effect of an ion cloud on the current flow pattern depends sensitively on the cloud conductivity compared to the conductivity of the ionosphere. The appropriate parameter that characterizes the cloud-ionosphere interaction is the ratio of the height-integrated Pedersen conductivity of the barium ion cloud to the height-integrated Pedersen conductivity of the ambient ionosphere.

D. LARGE SCALE BEHAVIOR

1. Motion of Ion Clouds

Equation (29) indicates that at any instant in time the electric field depends on the distribution of ionization in the ion cloud. In particular the polarization electric field due to the presence of the ion cloud reduces the total field at the center of the cloud as indicated at the top of Fig. 9. As a result, the center of the ion cloud moves with a slower velocity with respect to the neutrals than does a background ion that is flowing with the



$$\nabla \cdot \vec{N} \vec{E} = 0 ; \quad \vec{E} = \vec{E}_0 + \vec{E}_p \implies \nabla \cdot \vec{E}_p = -\vec{E} \cdot \nabla \ln [1 + N_c(r)/N_0]$$



$$U_c = \frac{E_0 / B}{1 + \frac{a}{a+b} \frac{N_c}{N_0}}$$

$a \gg b$

$$U_c = \frac{E_0 / B}{1 + \frac{N_c}{N_0}}$$

$$U_c = \frac{E_0 / B}{1 + \frac{1}{2} \frac{N_c}{N_0}}$$

$a = b$

$$U_c = \zeta E_0 / B$$

$$\zeta \sim \begin{cases} 1 - \frac{1}{2} \frac{N_c}{N_0} ; & N_c \ll N_0 \\ \sqrt{3} (N_c / N_0)^{-3/4} ; & N_c \gg N_0 \end{cases}$$

C8769

Fig. 9 Effect of Polarization Field Induced by the Ion Cloud

velocity \vec{U}_o . The value of the electric field at the center of the ion cloud depends on the ratio of the height-integrated Pedersen conductivity of the ion cloud, Σ_p^c , to the height-integrated Pedersen conductivity of the background ionosphere, Σ_p^a , as well as on the distribution of ionization in the ion cloud. For a uniform ionosphere and a constant neutral density, Σ_p^c/Σ_p^a can also be expressed as the ratio of height-integrated cloud to ambient density, N_c/N_o . The electric field at the center of the ion cloud, and thus its motion, can be expressed in terms of a coupling parameter, ζ , defined as the ratio of the electric field at the center of the ion cloud (in the frame of the ambient neutrals) to the external electric field,

$$\vec{E}_c = \vec{E}_o + \vec{E}_{pc} = \zeta \vec{E}_o, \quad (31)$$

where the subscript c represents the value at the center of the ion cloud. Since the difference in velocity between the ion cloud and the neutral wind is frame independent and equal to $\vec{E}_c \times \vec{B}/B^2$, Eq. (31) implies

$$\vec{V}_i - \vec{V}_n = \vec{U}_c = \zeta \left(\frac{\vec{E}_a \times \vec{B}}{B^2} - \vec{V}_n \right) = \zeta \vec{U}_o. \quad (32)$$

This equation also defines the frame invariant velocity of the ion cloud, \vec{U}_c . It follows that ζ ranges between one and zero for very small and very large ion clouds respectively;

$$\begin{aligned} \zeta \rightarrow 1, \quad & \vec{V}_i \rightarrow \frac{\vec{E}_a \times \vec{B}}{B^2}, \quad (N_c \ll N_o); \\ \zeta \rightarrow 0, \quad & \vec{V}_i \rightarrow \vec{V}_n, \quad (N_c \gg N_o). \end{aligned} \quad (33)$$

Very small clouds or low density perturbations provide a direct measure of the ambient electric field, $\vec{E}_a = -\vec{V}_i \times \vec{B}$, while very large clouds are completely tied to the neutral wind.

Theoretical models have been explored that give analytic expressions for the dependence of ζ on N_c/N_o .¹¹ A well-known example corresponds to a cloud of constant density N_c with an ellipsoidal cross section as illustrated in Fig. 9. Two interesting limits, a circular cloud with $a = b$ and an elongated cloud with $b \ll a$ are also shown. The former is the shape used by Haerendal, Lüst, and Reiger¹⁵ in deriving their now classic equation for determining the ambient electric field from the motion of barium ion clouds. In the high altitude limit ($\kappa_i \gg 1$), their equation can be brought into the form of Eq. (32) if the identification $\zeta = 2/(1 + \lambda^*)$ is made where $\lambda^* = (N_o + N_c)/N_o$. The elongated shape is most tied to the neutral wind and its motion corresponds to that of a field-aligned sheet of ionization. The degree of coupling also depends on the density profile of the ionization for large density clouds. A cylindrically symmetric cloud with a density profile $N \propto (1 + r^2)^{-4/3}$ is less coupled to the neutral wind for the same value of peak column concentration as indicated on the right-hand side of Fig. 9.

Figure 10 is a plot of the coupling parameter as a function of the ratio of cloud conductivity to ionospheric conductivity for several of the Secede releases. The estimated uncertainties in the values for ζ are indicated by the vertical error bars, and the horizontal error bars indicate a factor of two uncertainty in the estimates for the ratio of integrated conductivities. The two curves illustrate the two extremes in coupling¹¹ that depend on the

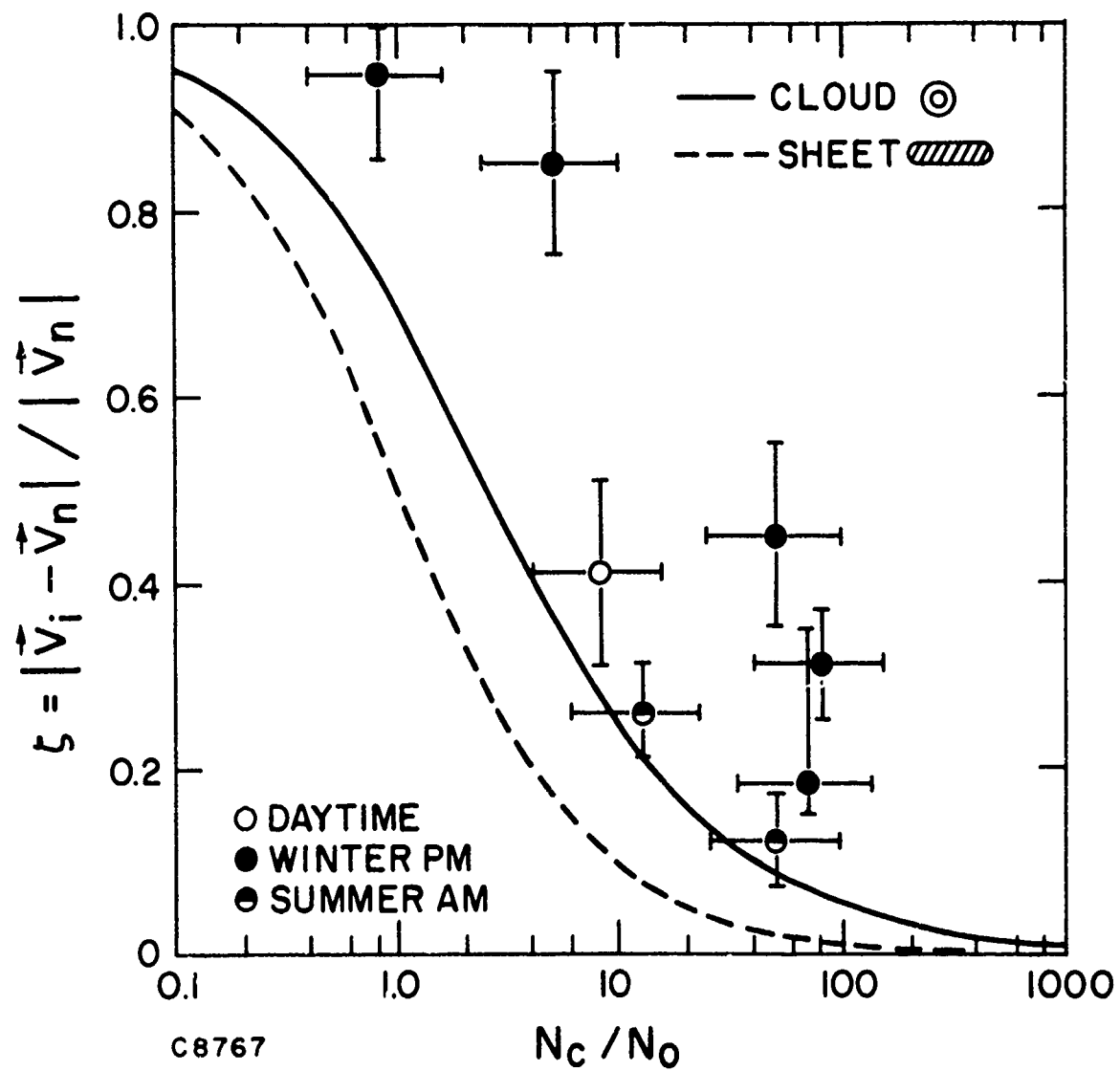


Fig. 10 Coupling Neglecting the Influence of the Conjugate Ionosphere. The open circle is event Quince while the half-filled circles are events Apple and Dogwood. In order from largest coupling parameter to smallest, the solid dots are the Plum Puff, Redwood, Plum, Spruce, and Nutmeg clouds respectively.

configuration of the ionization. The sheet-like shape is strongly coupled to the neutral wind, whereas the least coupled is the cylindrically symmetric cloud with a monotonic, radial density profile. A first glance at the data would suggest that the simple theory is inadequate to describe the degree of coupling of ion clouds to the neutral wind. We see that only the Quince, Apple, and Dogwood releases come near to agreeing with the theory. Note the large disagreement for the Secede II evening releases since the scale on the bottom is logarithmic and covers several decades. Thus the ion clouds are observed to separate from the corresponding neutral clouds much faster than the simple theory would allow. They behave as though the background ionosphere were far more conducting than the measurements of the ambient ionosphere indicate.

The observation that the winter evening (Secede II) releases are those that are in most serious disagreement with the theory led to the suggestion that the conjugate ionosphere in the southern hemisphere was contributing to the background ionospheric conductivity. This suggestion seemed plausible because the ionosphere conjugate to Eglin (at 54° S, 103° W) is further west and was experiencing summer and hence was sunlit. On the other hand, the ionosphere conjugate to the Secede I morning releases (at 49° S, 66° W) was experiencing winter and thus was still in darkness. More quantitatively, when the sun was 9° below the horizon after sunset at Eglin in the last half of January, 1971, and 9° below the horizon before sunrise at Puerto Rico in the first half of May, 1969, the sun was 26° above the horizon and 23° below the horizon, respectively, at the corresponding conjugate ionospheres. Hence it is reasonable to assume that the height-integrated Pedersen conductivity of the conjugate ionosphere for Secede II had a typical daytime value

of 5.0 mho. By adding these conductivities to the local values, we obtain new estimates for the ratio of cloud to ionospheric conductivity.

Figure 11 is a replotting of the data assuming that the conjugate ionosphere does contribute to the background ionospheric conductivity. By making this assumption we see that there is no longer any disagreement between the simple theory and the data. It is clear that these clouds do not move as though they were shaped like sheets. However, the data do not clearly distinguish between the two other cylindrical models whose theoretical curves are shown. Zabusky, Perkins, and Doles¹² have solved Eqs. (28) through (30) by finite difference techniques for a cloud with a cylindrically symmetric initial density distribution, $N = N_0 [1 + 4(1 - r^2/4)^4]$ for $r < 2$. The velocity of the peak density in the $\vec{E} \times \vec{B}$ frame is $0.63 \vec{V}_n$. The corresponding value for the coupling parameter, ζ , is 0.37. This value for $N_c/N_0 = 4$ is shown as a solid square in Fig. 11. We note that this point is in excellent agreement with the analytical models, lying closer to the curve with a density profile (which should provide an upper limit) than to the curve for a cylinder with constant density.

We note that the agreement with the theoretical model includes data in which the ratio of conductivities ranges over two and one-half orders of magnitude. This agreement is highly suggestive that the conjugate ionosphere must participate in the dynamics of the motion of barium ion clouds. We estimate that an Alfvén wave (the propagation velocity of an electromagnetic disturbance) can travel from the northern to the southern hemisphere and back in half a minute, so there is sufficient time to communicate the polarization electric fields between the two hemispheres. The most sensitive test of the theory would be to make an Apple size release (12kg) at dawn and

COUPLING INCLUDING CONJUGATE IONOSPHERE

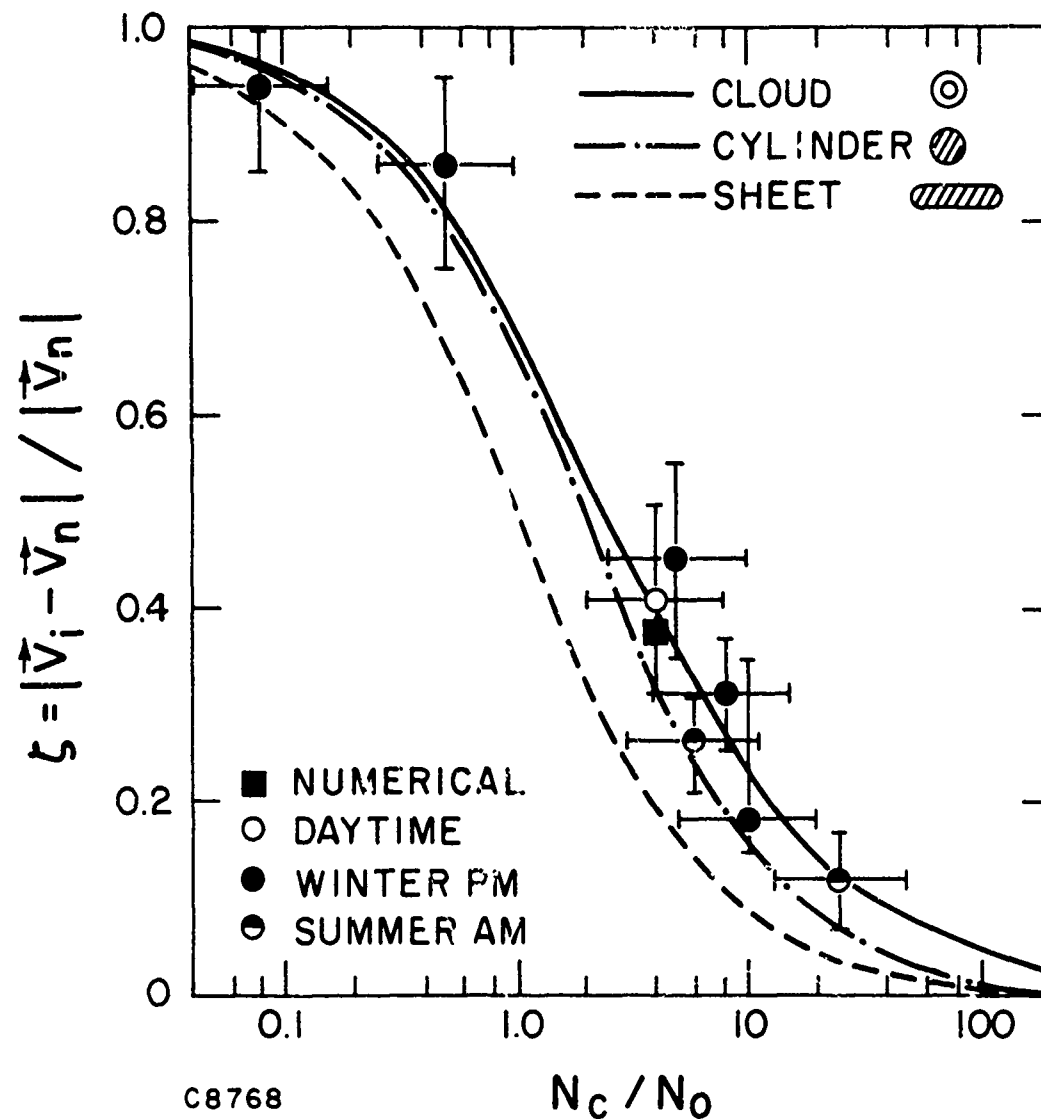


Fig. 11 Coupling Including the Influence of the Conjugate Ionosphere. The dots represent the same clouds shown in the preceding figure. The solid square represents the point obtained from numerical modeling.

dusk. The degree of coupling with the neutral wind should change from about 65% ($\zeta = 0.35$) to about 30% ($\zeta = 0.7$) for the assumed change of a factor of five in the ratio of conductivities.

There are two other possible explanations for the lack of agreement between data and theory shown in Fig. 10; either the data are plotted incorrectly, or the theoretical treatment is wrong. The largest uncertainty in the velocities listed is the ambient ionospheric velocity, $\vec{E}_a \times \vec{B}/B^2$, which has been assumed to be less than 20 m/s where better estimates were not available. The electric field probe indicates that this velocity may be as much as 60 ± 20 m/s westward during Spruce. Granting a velocity of this magnitude, the effect on the data points shown in Fig. 10 would be to reduce ζ by a factor of two. It is easy to see by inspection that the data points would still be in disagreement with theory. It is unlikely that this large a discrepancy in $\vec{E}_a \times \vec{B}/B^2$ will allow a reconciliation with theory.

The remaining possibility is that the theory does not correctly describe the coupling of the barium cloud to the rest of the ionosphere. It is true that the complications of this interaction are hidden by ascribing to the ionosphere a height-integrated conductivity, a procedure that would be strictly valid only if the value of $(\Omega\tau)_i$ outside the cloud were constant and the same as for barium. There is no assessment yet as to the effect to be expected from a more rigorous treatment of the dynamics of the rest of the ionosphere. On the other hand, the assumption that the reconciliation between data and theory is achieved by including the effect of the conjugate ionosphere is a simple and plausible one.

There are several important implications that follow from assuming that the conjugate ionosphere plays a role in the ion cloud dynamics. First

is that the cloud-produced polarization electric fields must project into the southern hemisphere which suggests that the assumption that the earth's magnetic field lines are equipotentials for a large distance is reasonable. A second conclusion is that there must be magnetic-field-aligned currents in the magnetosphere, and a third conclusion is that the presence of the ion cloud and its resulting motion in the northern hemisphere must cause a disturbance in the ion density in the conjugate ionosphere in the southern hemisphere. An independent verification of any of these effects would be very valuable.

Let us adopt a simplified model of an ion cloud in the ionospheric-magnetospheric system as shown in Fig. 12 in order to make a quantitative estimate of some of these effects. We find that the magnetic field lines are highly conducting so that the electric fields do not suffer any appreciable resistive losses in being projected into the conjugate ionosphere.¹¹ The most important effect is the disturbance in electron density that the current flow in the background ionosphere is likely to make. The parallel currents must be closed by Pedersen currents which are due to the flow of the background ions. This ion flow will lead to significant changes in the local ionospheric density.¹⁴ These changes should be observable by ionosondes. In particular, for the Secede II releases, the motion of the ion clouds should have produced large changes in electron density in the conjugate ionosphere in the southern hemisphere. These changes should have been detectable had ionosondes been deployed there.

2. Deformations of Large Ion Clouds

The electric field varies over the distribution of density in the ion cloud as discussed above and as shown schematically in Fig. 9. Since

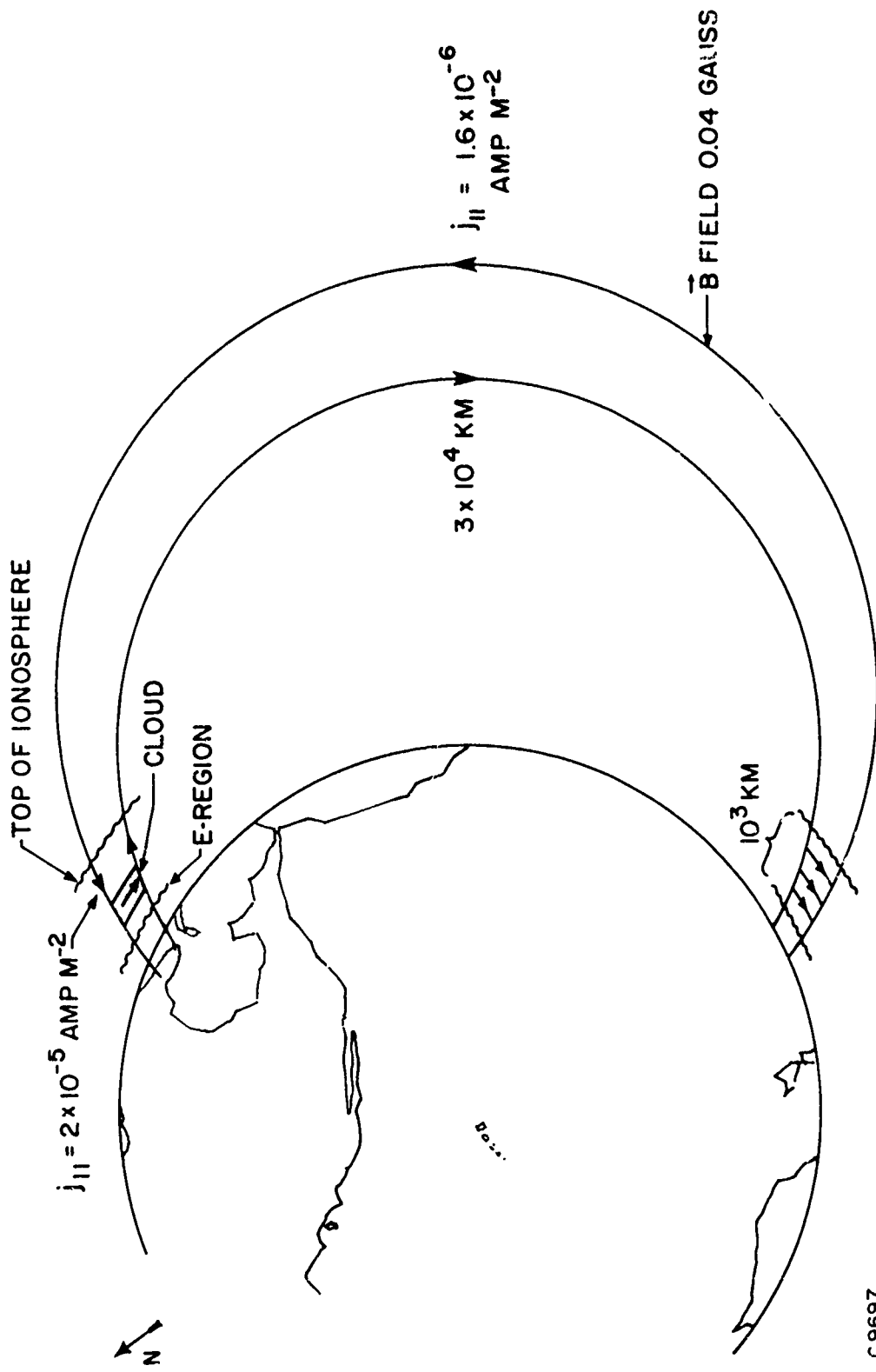


Fig. 12 Sketch of Magnetospheric Current Flows which Couple the Conjugate Ionosphere and the Barium Cloud

the ionization moves with the local $\vec{E} \times \vec{B}/B^2$ velocity, different parts of the ion cloud move with different velocities. Thus, as the ion cloud moves, its shape distorts. Linson¹⁰ has analytically investigated the changes in shape of equal density contours by expanding the solution of the nonlinear equations for the equipotentials (streamlines) as a power series in time. If only the first, time-independent term is retained, then the deformation of an initially cylindrically symmetric concentration is shown in Fig. 13a. However, the streamlines are not time-independent. By retaining the next time-dependent term, there is a qualitative difference in the distortion of the equal density contours as shown in Fig. 13b. Note that the contours are convex outward on the righthand or front side of the barium ion cloud when the more accurate expression is used. We also note that the backside has become steeper during the same time interval.

Equations (29) and (30) have also been solved by a finite difference technique on a digital computer¹² for the case of an initially cylindrically symmetric ion cloud with a maximum ratio of integrated-conductivity $N_c/N_o = 4$ as shown in Fig. 14. The steepening of the backside--that is, the side on the left where the neutral cloud would be -- is prominent. The steepening shown in this and the preceding figure provides an explanation of the fact that the trailing edge of ion clouds develop a large density gradient when seen from a variety of views. We also note that the ion cloud elongates in the direction of its motion. Since the flow as described by Eqs. (29) and (30) is incompressible, the area enclosed in each equal density contour remains constant.

Analytical models yield an estimate of a steepening time. However, such estimates are sensitively dependent upon both the assumed density

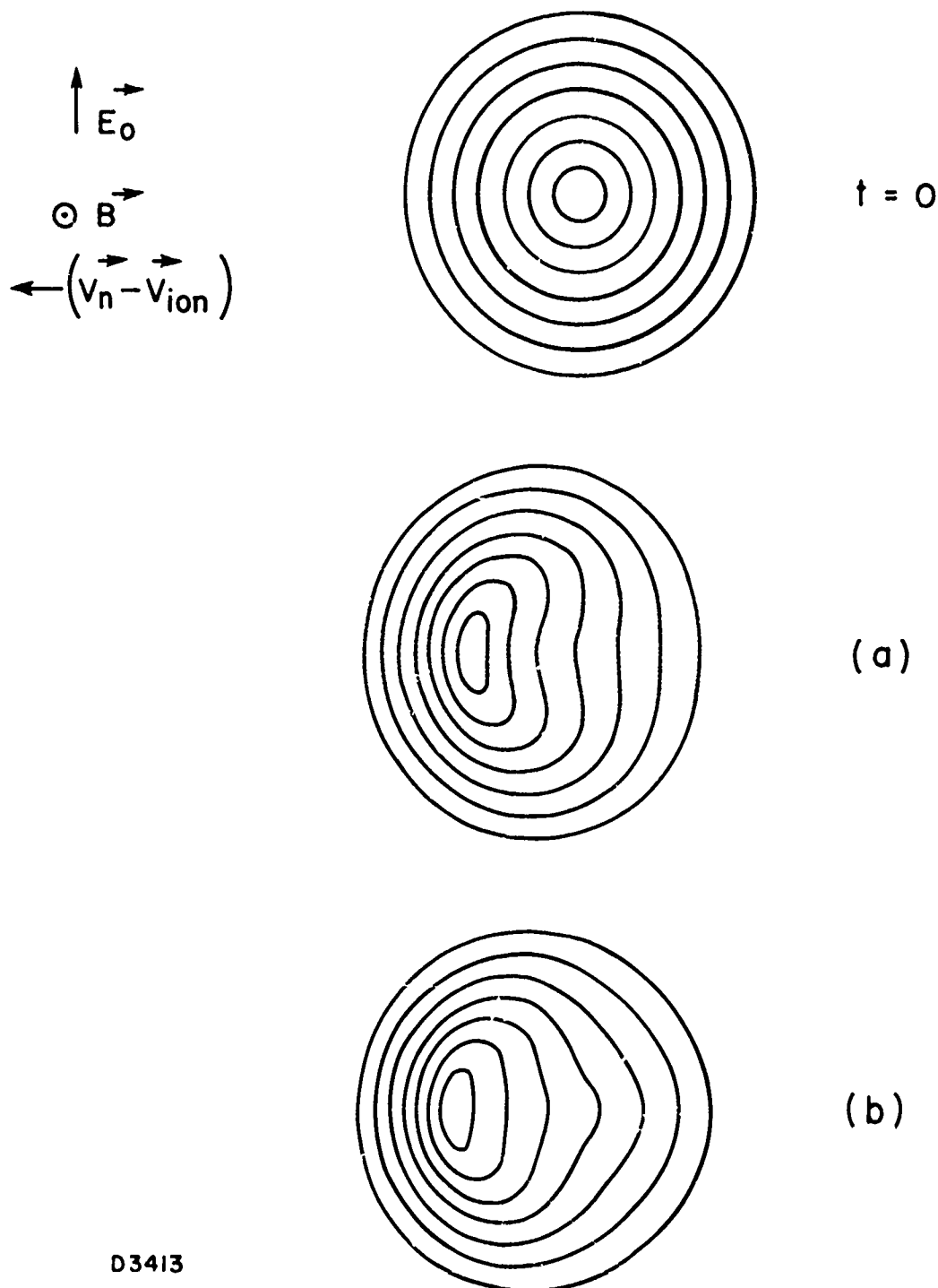
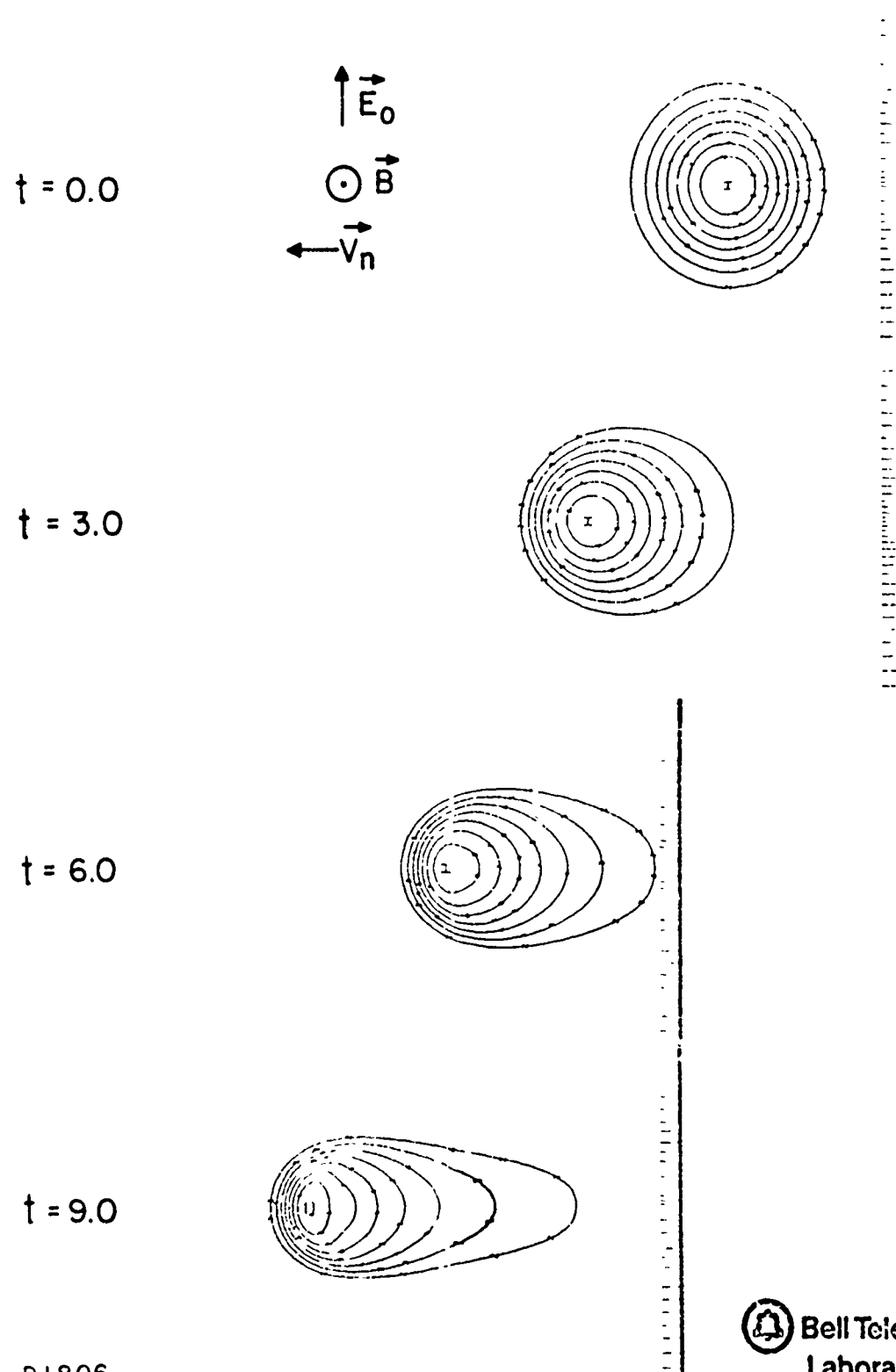


Fig. 13 Deformations of Contours Resulting from Power Series Expansion of the Streamlines in Time; a) Zeroth Order Term; b) Zeroth Order Plus First Order Term

COMPUTER SOLUTION SHOWING STEEPENING



D1806

 Bell Telephone
Laboratories

Fig. 14 Deformations of Isodensity Contours for an Initially Circular Plasma Cloud with No Initial Perturbation (Bell Telephone Laboratories)

profile in the ion cloud and the definition of steepening. Figure 15 shows steepening times normalized by the ion cloud radius at half-maximum density and the velocity \vec{U}_0 as obtained from two different models. The curve (a) results from a model¹⁰ in which the ion cloud density has a slowly decreasing profile varying like $N \propto (1 + r^2)^{-4/3}$. The steepening time in this case is defined in terms of the time for the peak density to move a typical distance over which the streamlines vary significantly. On the other hand, the curve (b) represents the relative motion of a cylindrical ion cloud with constant density and a sheet-like configuration with the same density. We see that for ion clouds with low conductivity the steepening time varies inversely with cloud conductivity. We also see that for ion clouds with large conductivity the steepening is very model dependent.

An estimate of the steepening time has also been obtained from the numerical solution shown in Fig. 14. The gradient in density between the third and fifth density contours from the center increase linearly with time up to $t = 6.0$, apparently doubling at $t \approx 4.5$. If we take this time as the steepening time, and normalize it with respect to the half-density radius, $a = 0.8$, we find $\tau_s = 5.63 a/U_0$ which is shown as a black square in Fig. 15, in reasonable agreement with the analytical models. An analytic calculation corresponding to Event Holly¹⁶ (a 2.4 kg release at 194 km altitude) is given in Ref. 10 and is shown in Fig. 15 as a black dot.

Zabusky, Perkins, and Doles⁵ have presented a simple elongated model of an ion cloud that is useful not only for showing steepening, but also for illustrating the narrowing of the middle portion of an ion cloud after it has become elongated. Assume a cloud elongated in the direction of its motion (the x-direction) such that $\partial N/\partial y \gg \partial N/\partial x$.

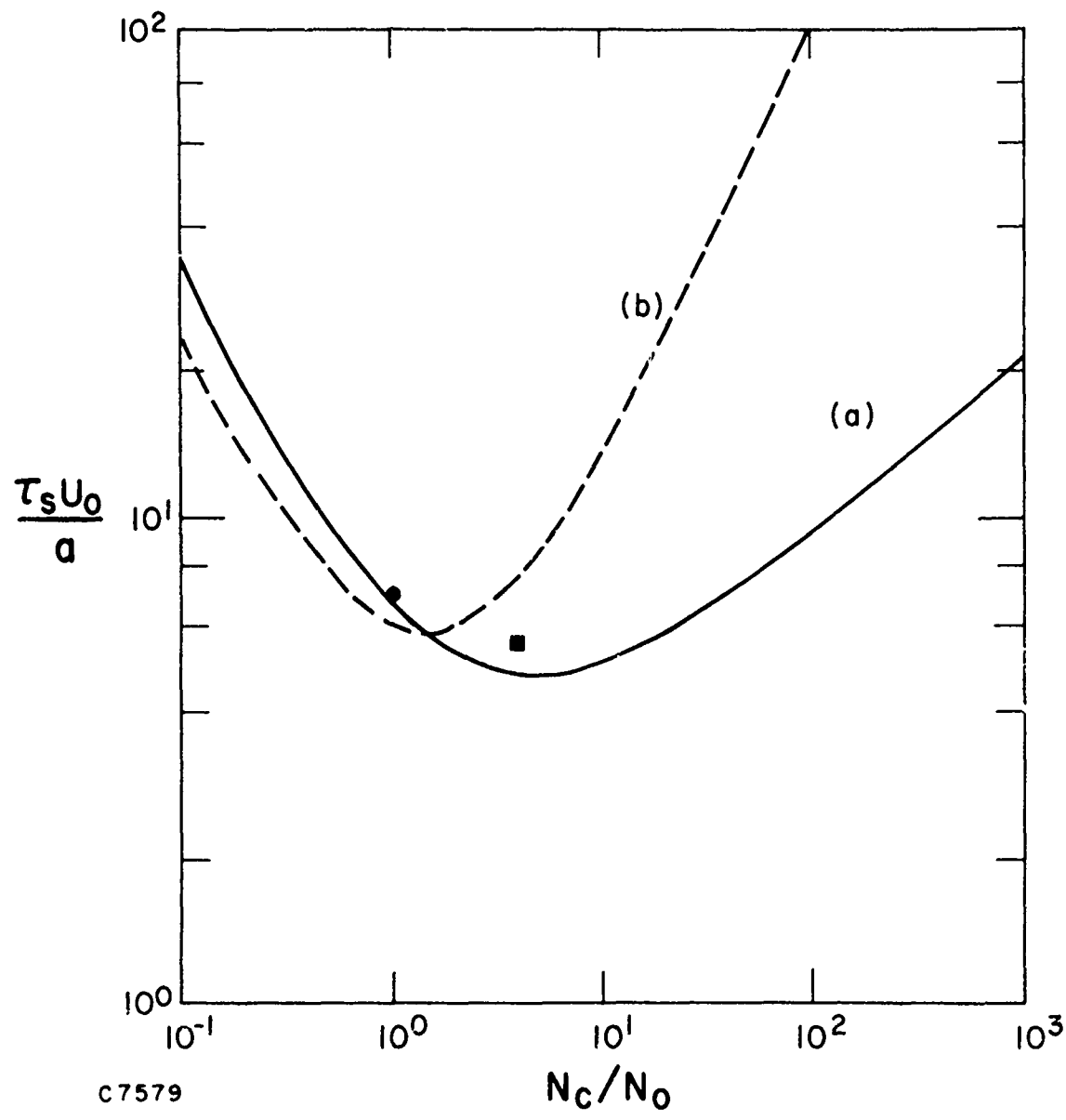


Fig. 15 Steepening Time According to Two Different Models; a) Broad Density Profile; b) Constant Density within a Cylinder. The filled square represents a point obtained from numerical modeling. The filled circle represents the steepening time for Event Holly.

The y-component of the electric field as determined by Eq. (29) is given roughly by

$$E_y \approx -\frac{N_o}{N} E_o$$

and the equation $\nabla \times \vec{E} = 0$ gives

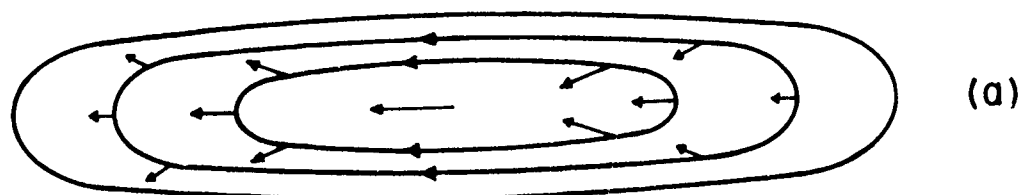
$$E_x \approx -y \frac{N_o}{N^2} \frac{\partial N}{\partial x} E_o.$$

Hence, the velocity components in the drift frame (which best shows the cloud distortions) are

$$v_x = -\left(1 - \frac{N_o}{N}\right) \frac{E_o}{B}; \quad v_y = y \frac{N_o}{N^2} \frac{\partial N}{\partial x} \frac{E_o}{B}$$

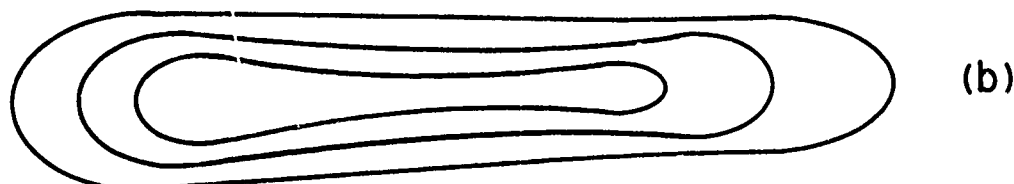
and are illustrated in Fig. 16a. The isodensity contours then deform into a "dumbbell" shape narrowing significantly in the middle as illustrated in Fig. 16b.

These distortion features are evident in the many optical observations of barium ion clouds. For instance, the Olive ion cloud shown in Fig. 17 at 17 minutes after release has elongated approximately 55 km in the direction of its motion and its midpoint had narrowed to a dimension of the order of 1 km transverse to the direction of its motion. By the same time, the ion cloud had diffused parallel to the magnetic field, resulting in an extension of over 60 km in the direction of the magnetic field. This configuration is best described as a sheet, and it is important to take this configuration of ionization into account when attempting to describe radar effects. The regions of highest densities do not occur in this thin sheet region but are confined towards the back edge of the cloud which becomes unstable and breaks up into a number of sheets and rods as we shall discuss below.



$\leftarrow \vec{v}_n$ $\uparrow \vec{E}_0$ $\odot \vec{B}$

(a)



D 3513

Fig. 16 Narrowing of an Elongated Ion Cloud

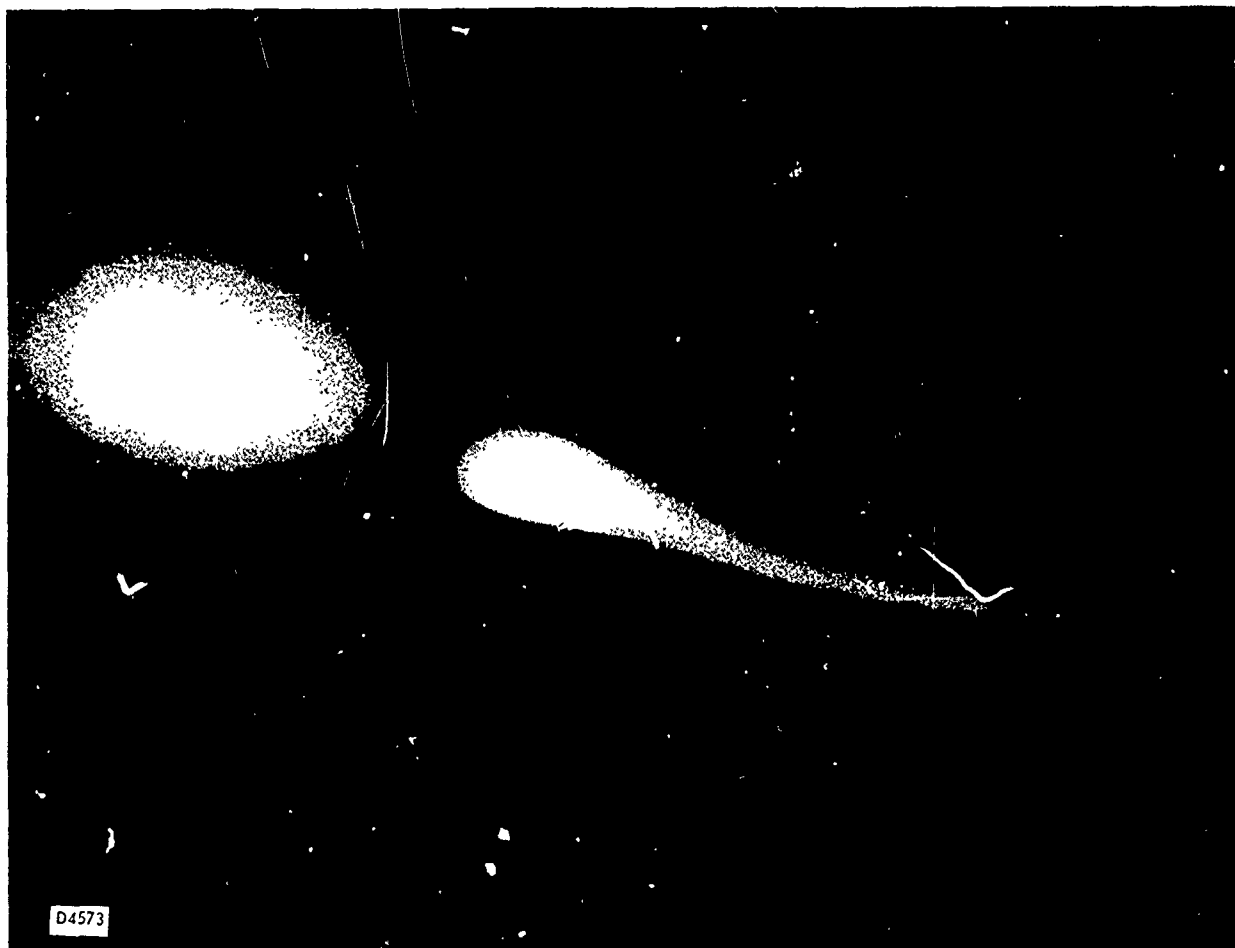


Fig. 17 Elongated Olive Cloud Stretched into a Thin Sheet (Technology International Corporation)

Figure 18 is a photograph of the Spruce ion cloud from Site C-6 looking nearly up the magnetic field line. The features described above are evident in this photograph. The ion cloud is highly elongated in the direction of the neutral wind. The middle portion of the ionization is very thin.

We conclude this section by summarizing the principal features of the large scale behavior of barium ion clouds. The ion cloud lengthens in the direction of the magnetic field in accordance with ambipolar diffusion theory and distorts into a thin flat sheet of ionization with the highest density portion developing into smaller sheets of ionization. On the scale of the whole cloud, there is negligible diffusion of ionization across the magnetic field in the time scale of 1/2 hour. The electron density decreases as $t^{-1/2}$ in accordance with one dimensional diffusion in a uniform medium. At late times this decrease slows as the ion cloud achieves diffusive equilibrium in the variable scale height neutral atmosphere as discussed in Chapter 1. The dependence of the ion cloud motion on the ambient electric field, \vec{E}_a , the neutral wind velocity, \vec{V}_n , and the ratio of height-integrated Pedersen conductivity of the cloud to the ambient ionosphere, N_c/N_o , is well understood. An important point is that the conjugate ionosphere participates in the dynamics of barium ion clouds.

E. STRIATIONS

One of the most interesting features of barium ion clouds is their tendency to break up into magnetic-field-aligned structures that have the appearance of striations. The process that leads to the formation of these striations is the gradient-drift instability.³ This structuring occurs as a result of the tendency of the peak densities in the ion cloud to move more with the



Fig. 18 The Spruce Ion Cloud Showing Elongation in the Direction of the Neutral Wind and Narrowing in the Middle (Technology Internati Corporation)

neutral wind velocity. Thus the peak electron densities that originally are created near the center of barium ion clouds eventually end up in the fine scale striations at late times. This behavior has been shown with the use of numerical simulations¹². A great deal has been learned about the detailed development of structure in the ion cloud by using the fluid-dynamic analog or Hele-Shaw cell.¹⁷ The behavior exhibited by this experiment is believed to be relevant to the high-altitude barium cloud case not only because the dynamics in the appropriate limits are described by equivalent sets of equations but also because we are fortunate to have observations of barium ion clouds as they passed through the magnetic zenith as seen from Site C-6 at a time when they were fully striated. These unique observations of three different barium clouds allow us to confirm that many of the structures seen in the Hele-Shaw cell also occur in barium ion clouds which suggests that the simple set of equations (28) through (30) adequately describe the features that develop in high altitude barium ion clouds. Before proceeding with some of the quantitative results obtained from the theory, let us first give an overall description of striation morphology.

Figure 19 is a schematic drawing of the several stages of development of striations that form on the backside of ion clouds. Initially, a broad spectrum of density perturbations can grow. There does tend to be a preferred scale size evident in photographs of barium ion clouds. The perturbations grow into magnetic-field-aligned sheets of ionization. In the third stage, these sheets undergo a series of complex evolutions that include pinching of sheets to form rods and bifurcations of the sheets. At late times the ionization pinches off forming a series of a large number of rods. Small

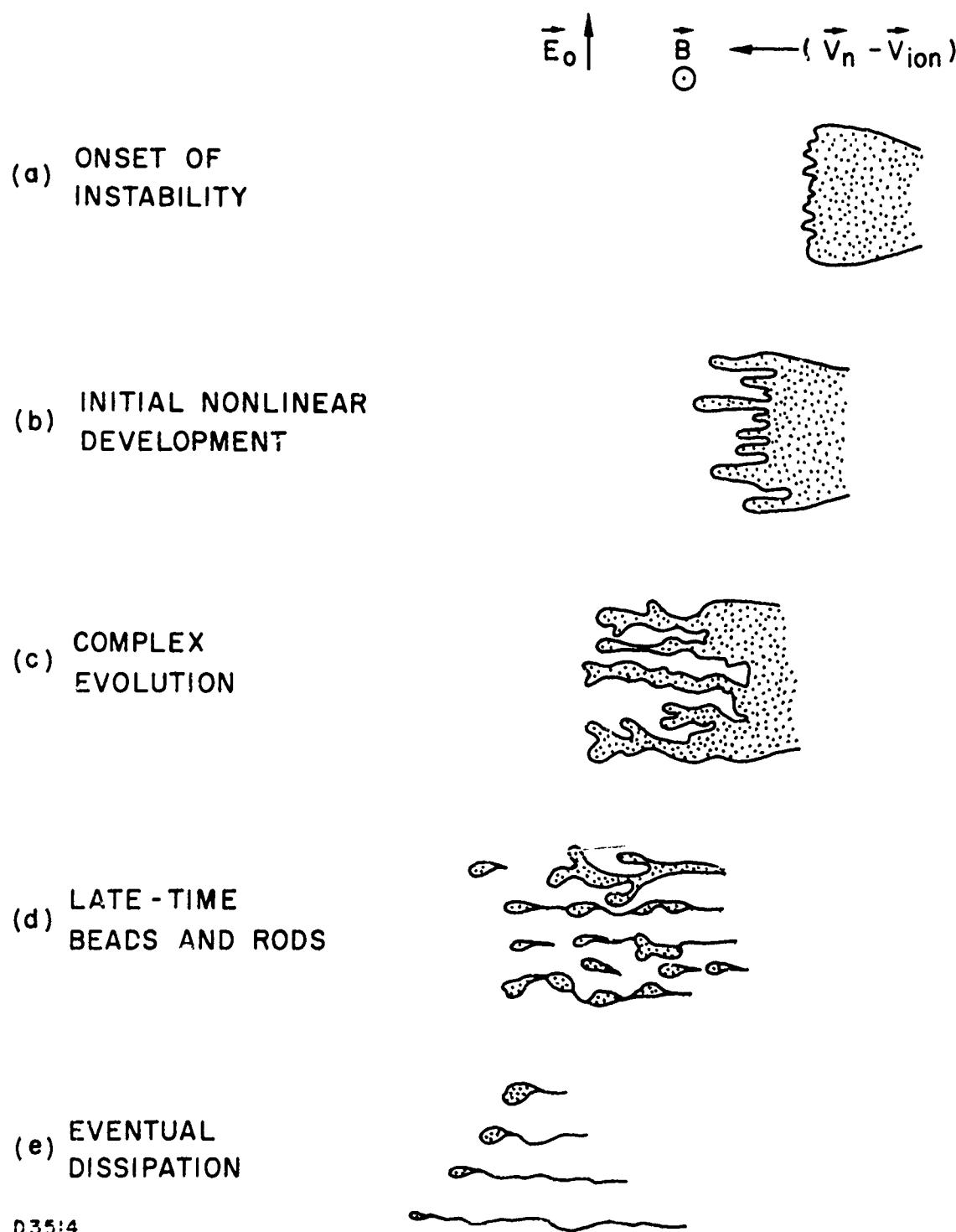


Fig. 19 Morphology of Nonlinear Striations Deduced from Photographs, Simulations, and Theory

rods are seen to slowly fade away apparently into very thin sheets. The fact that small scale sizes in the rods and sheets and large density gradients exist over times of minutes indicates that the diffusion of ionization transverse to the magnetic field in these large density ion clouds is controlled by electron collisions.

1. Onset Time

Barium ion clouds, while elongating, appear to remain rather regularly shaped for significant periods of time before finer scale structure is seen. There apparently is a delay between the formation of the ion cloud and the time at which structure is first seen. The ability to understand and predict this onset time of striations is very important. The parameters discussed in the previous section contain only two independent units of time. They are the ion-neutral collision time, τ , and the time proportional to the reciprocal of the background electric field measured in the frame of the neutrals, U_0^{-1} . Effects associated with the first time scale lead to diffusion which does not generate structure. The ambient electric field, on the other hand, is the mechanism that drives the gradient-drift instability. It is reasonable to expect that the onset time of striations should vary inversely as U_0 , all other conditions remaining constant.

In the Secede II test series, both the 1 kg clouds and the 48 kg Spruce and Plum clouds were released approximately at the same altitude. Figure 20 shows a plot of the onset time of these clouds as a function of the estimated U_0^{-1} for each of these releases. The large horizontal error bars represent the present uncertainty in the value of the ambient electric field. We see that there is agreement with the expected behavior indicated by the solid lines. We should point out that the neutral wind can affect the

peak electron density produced due to the finite time needed to ionize barium atoms. As a result, the Plum cloud did not perturb the conductivity of the ambient ionosphere to the same extent that the Spruce cloud did and hence they were not identical clouds. Figure 20 can be used for making predictions as to the onset time of striations for 48 kg releases at 185 km altitude at Eglin AFB during the winter evening once the values of the neutral wind and the ambient electric field have been given. All of these caveats have been made because, although the linear relationship between onset time and U_o^{-1} can be expected, the value of the slope does depend on the altitude, yield, release location on the earth, the time of day (morning dawn or evening dusk) and the season of the year. Our theoretical understanding combined with empirical scaling of the Secede data would allow us to make fairly reliable estimates of what the slope should be once the future test location and time have been specified.

Figure 21 is a purely empirical scaling of the onset time of striations, normalized to $U_o = 75$ m/s, as a function of altitude between 150 and 250 km for 48 kg payloads released at midlatitude regions. While there is no theoretical basis for the curve drawn in Fig. 21, it should provide the basis for an accurate prediction of onset time once the appropriate value of $U_o = \left| \vec{V}_n + \vec{E}_a \times \vec{B}/B^2 \right|$ is known.

Figure 22 is a comparison of the normalized observed onset time of striations as a function of the estimated ratio of height-integrated cloud conductivity to the height-integrated background ionospheric conductivity with a theoretical curve. The scale to which the onset times are normalized is a/U_o , the time for the background ionization to flow a distance equal to

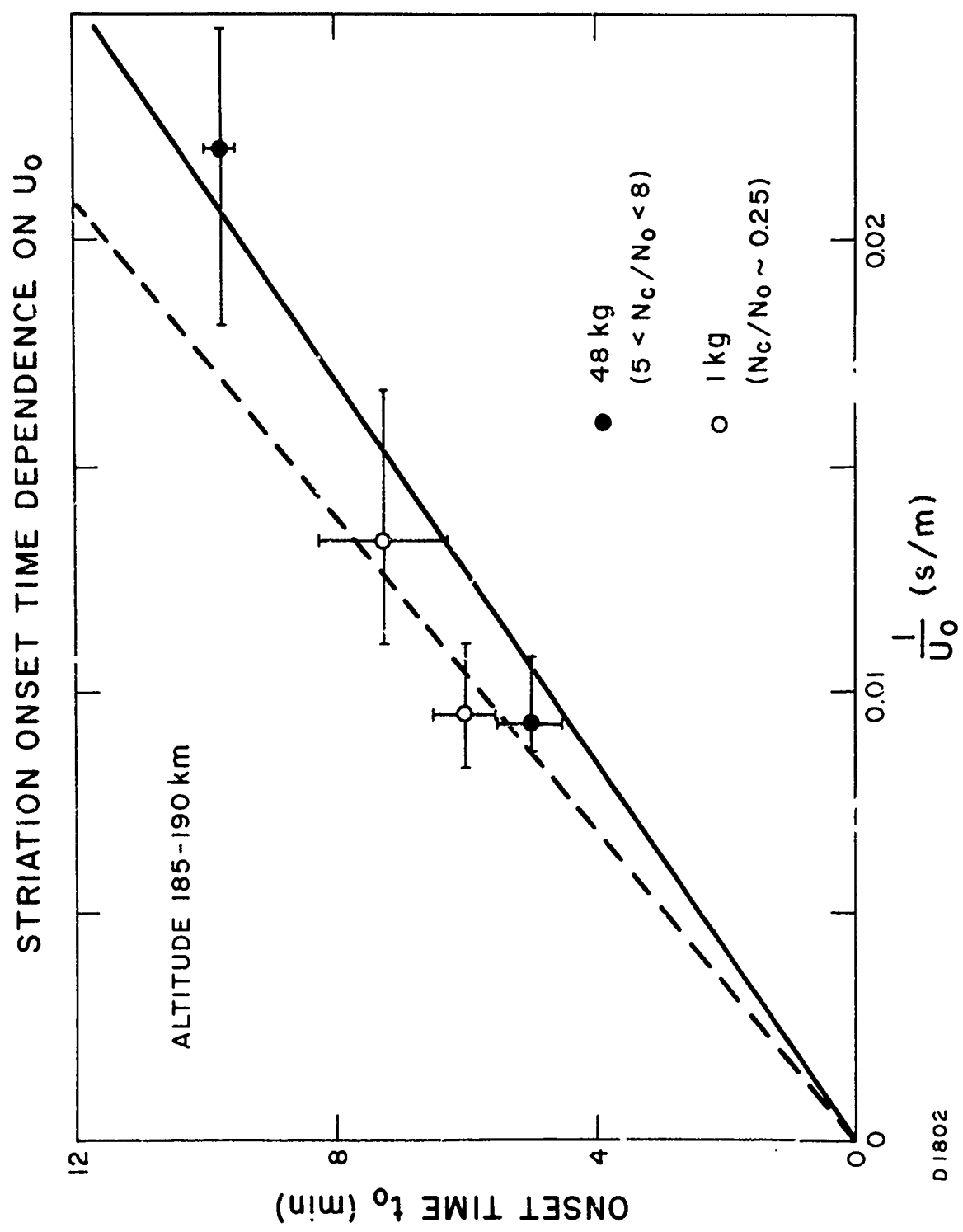


Fig. 20 Onset Time as a Function of U_0^{-1}

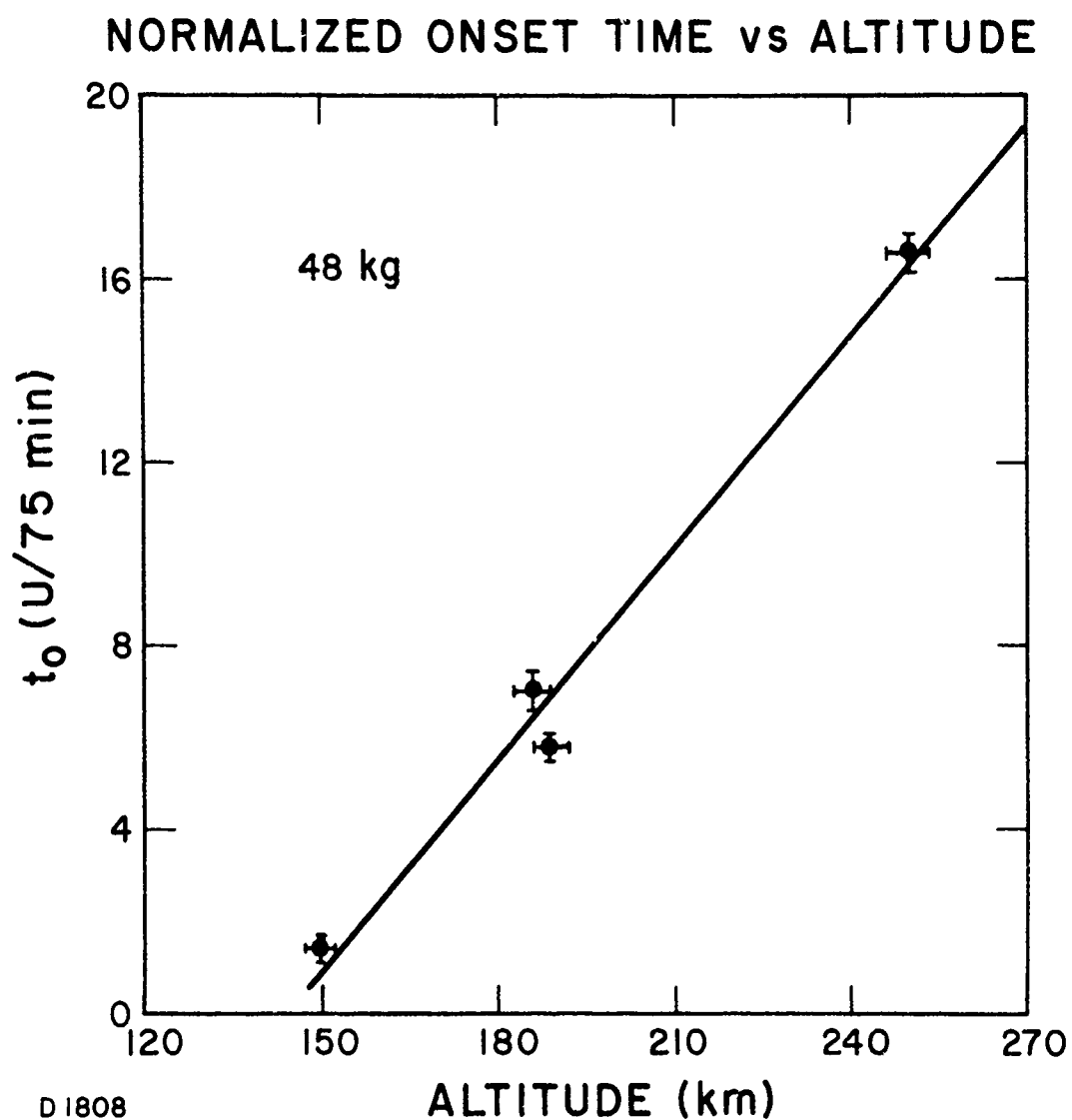


Fig. 21 Onset Time (Normalized to $U_0 = 75 \text{ m/s}$) Dependence on Altitude at Constant Payload

the estimated initial radius at half-maximum density of the ion cloud. The error bars represent the uncertainty in the estimate of the data. The primary uncertainty lies in the value of the ambient electric field, \vec{E}_a , and in the ratio of conductivities, N_c/N_o . The theoretical curve represents a steepening time, that is the time it takes a sheet-like configuration of ionization to move a distance equal to the initial cloud radius at half-maximum density relative to the motion of the center of the ion cloud. The solid curve results from a constant density, cylindrical cloud; by using the expressions given in Fig. 9, we obtain

$$\frac{\tau_s U_o}{a} = \frac{U_o}{\Delta U} = 2 \frac{N_o}{N_c} + 3 + \frac{N_c}{N_o} . \quad (34)$$

The shaded area is an indication of the variation that results from using different initial density models. The similarity in the shape of the theoretical curve and the distribution of the data points is striking. The agreement in magnitude is fortuitous because there is no reason why the numerical coefficient relating the onset time to the dimensional time, $a/\Delta U$, should have been one in this nonlinear problem. It appears that a numerical coefficient a little greater than one would give even better agreement. Note that the data extend over two orders of magnitude in the ratio of cloud to ionospheric conductivity.

The data plotted in Fig. 22 include all of the variations in yield and altitude. It should further be emphasized that the estimates for the height-integrated background conductivity were based on inclusion of estimated effect of the conjugate ionosphere as was done in Fig. 11. If only the local ionospheric conductivity had been included, all of the Secede II

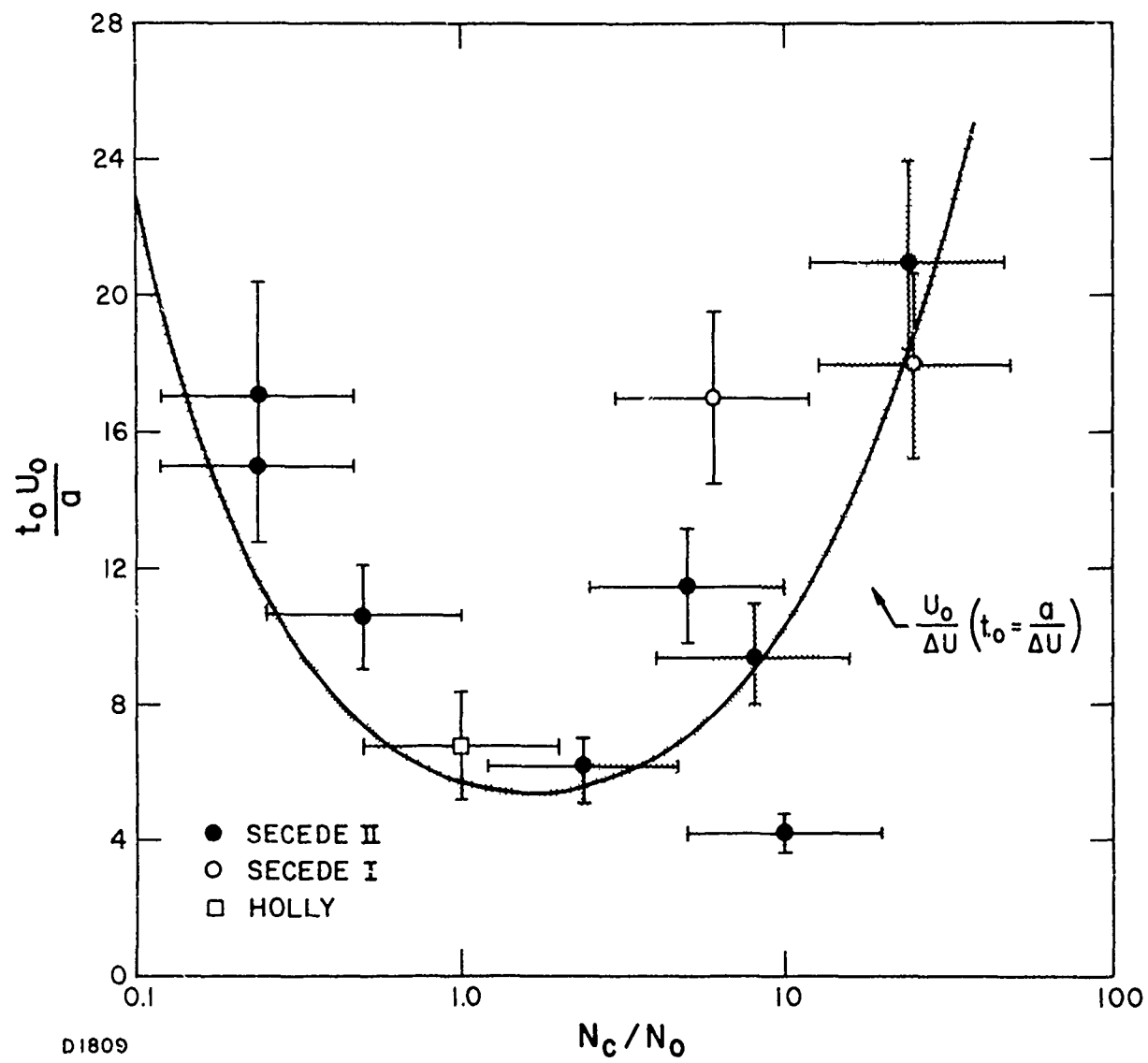


Fig. 22 Normalized Onset Time as a Function of Cloud to Background Height-Integrated Pedersen Conductivity

data points shown by the solid circles would have been displaced an order of magnitude to the right. This agreement of the observed onset times of these barium ion clouds with the theoretical curves is an independent indication that the conjugate ionosphere participates in the dynamics of barium ion clouds. We do note that there are two data points that do not agree with the theoretical curve. The Apple ion cloud striated later than it should have while the Nutmeg ion cloud produced striations much more rapidly than expected. At present there is no definite explanation for this discrepancy. Perhaps the error bars on Apple should be larger; perhaps the lower altitude Nutmeg cloud had large initial perturbations.

In general, we would conclude that we have a solid basis for making predictions of the onset time of striations both empirically by using the data base and by a theoretical model that can be used to obtain predictions under a wide variety of conditions.

2. Scale Size of Striations

We now turn our attention to the question of the scale size of the striations. Much of our information has been obtained from photographs that were taken looking directly up the magnetic field line into the highly striated portions of the Redwood, Spruce, and Nutmeg ion clouds as shown in Figs. 23, 24, and 25 respectively. We note that there is a wide variety of scale sizes evident in the sheet and rod-like structures shown. We shall examine some of the details of the fine scale structures below. We do note that in spite of the variety of detailed structure present, there is an overall sheet-like appearance, particularly in the Redwood and Spruce ion clouds. We conclude that there is apparently a predominant overall wavelength.



Fig. 23 Redwood Striations Viewed Directly Up the Magnetic Field Line (Technology International Corporation)



Fig. 24 Spruce Striations Viewed Directly Up the Magnetic Field Line
(Technology International Corporation)

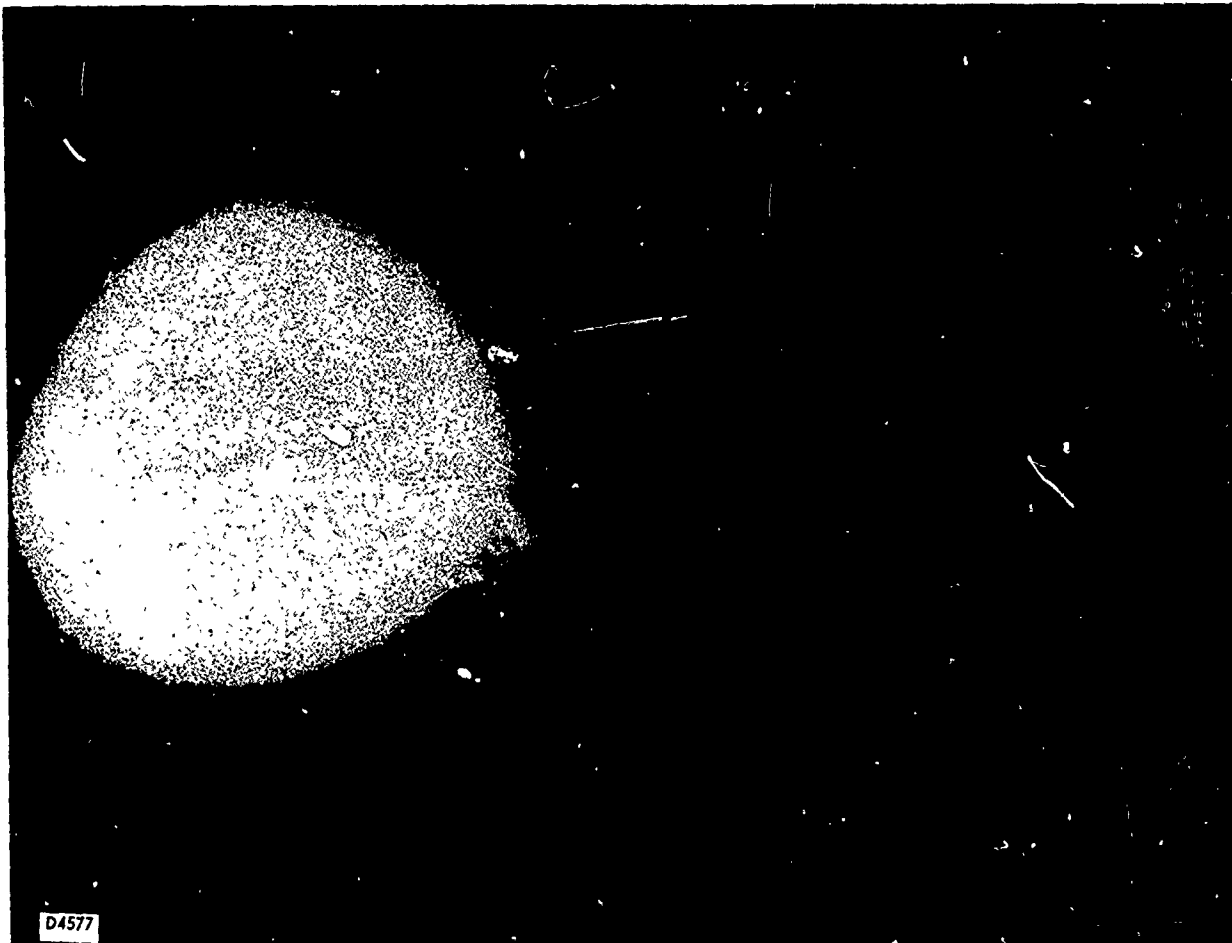


Fig. 25 Nutmeg Looking Directly Up the Magnetic Field Line
(Technology International Corporation)

We now point out the overall similarity between the photographs of the barium ion cloud taken up the magnetic field line and the hydrodynamic analog experiments conducted in a Hele-Shaw cell by Thomson.¹⁷ In Fig. 26 we see overall sheet-like structures in addition to finer structures that we shall describe below. The fluid motion exhibited in Fig. 26 is described by a set of equations identical to Eqs. (28) through (30) that apply to high altitude barium ion clouds as discussed in Section C. The structures seen in the Hele-Shaw cell are identical in many respects to those that can be seen in barium ion clouds. The Hele-Shaw cell has the advantage that one can follow the nonlinear evolution of a given sheet or striation without becoming confused by its changing aspect. When viewing a barium cloud striation, it is located near the magnetic zenith only for a short time, and as it moves out of the region close to the zenith its appearance changes as more of its extension parallel to the magnetic field can be seen projected into the field of view.

In looking at the detailed evolution of these sheets, it is seen that typically a large sheet grows and then bifurcates, breaking up into two smaller sheets. Figures 27 and 28 are tracings of the characteristic shapes that evolve at the tip of sheets in the Hele-Shaw experiment. Figure 27 shows a typical bifurcation process in both a symmetric and asymmetric form. Figure 28 shows a more complex evolution into three structures on the left-hand side; the right-hand side represents the growth of a sheet of less dense ionization into denser ionization. It seems apparent that this process of a sheet growing and then breaking up into smaller structures that develop into larger sheets keeps repeating. This process appears to continue until a sheet becomes pinched off at some location. The isolated

RUN 36P
CELL GAP .06"
" DIM 18X24
CLEAR GLYCER
LIQD WATER
COLOR SALT H₂O
LIQD &
GLYCER
TILT 90
CIRC DIA 1/2
FILM PLUS X
CAMERA 35 MM
DISTANCE 6
FIG
1/30

D4587

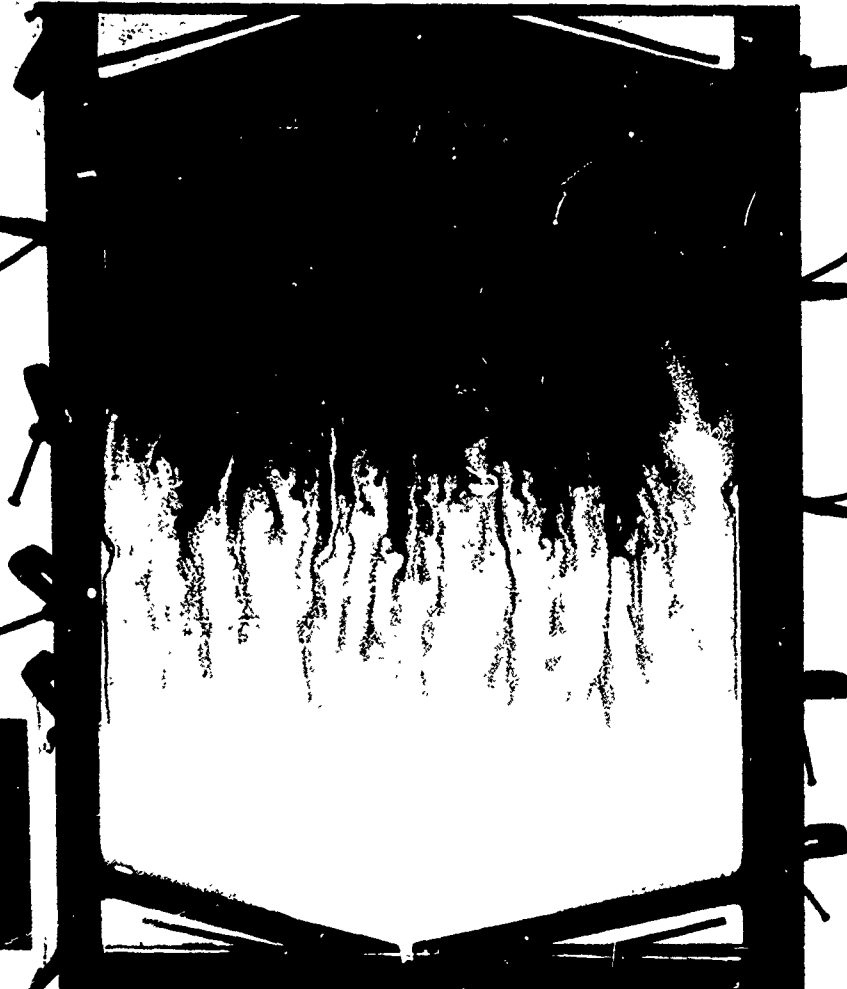


Fig. 26 Striation Development in the Hele-Shaw Cell (Physical Dynamics, Incorporated)

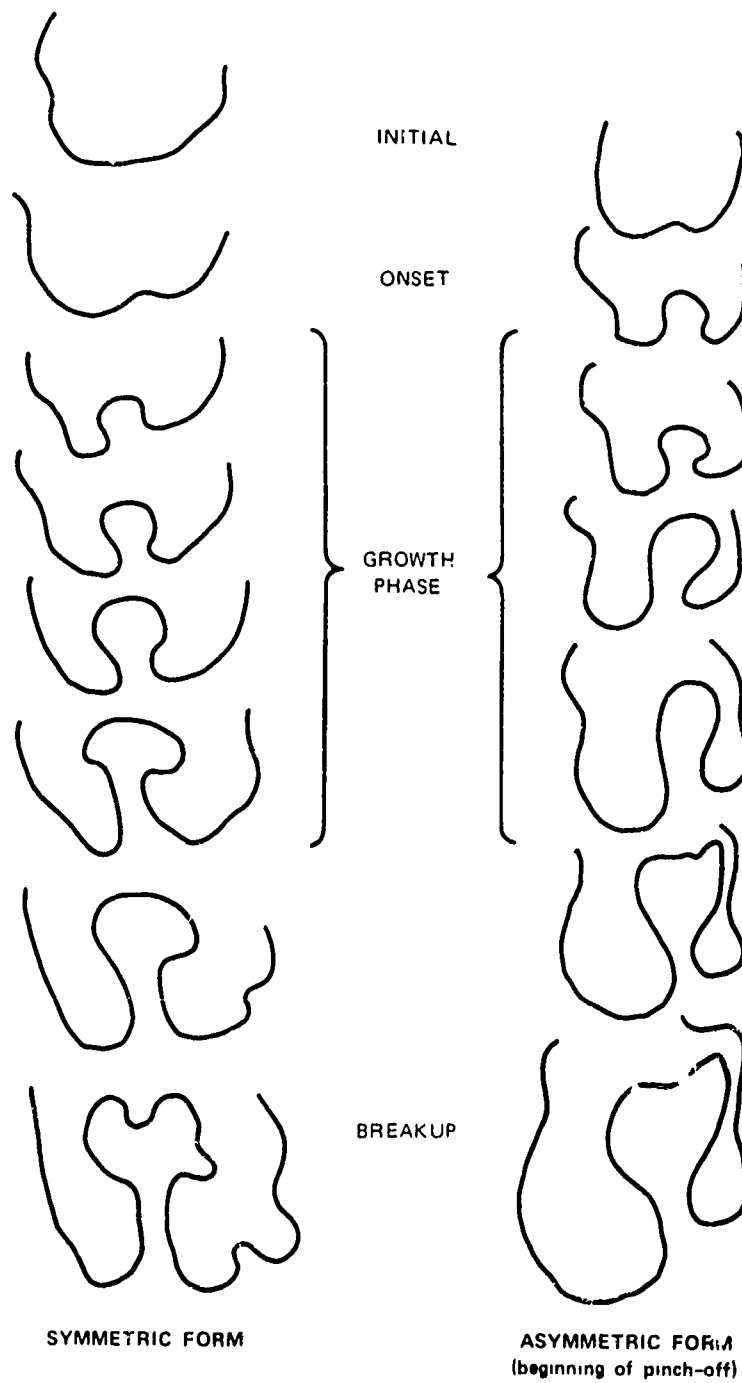


Fig. 27 Bifurcation for a Typical Sheet (Physical Dynamics, Inc.)

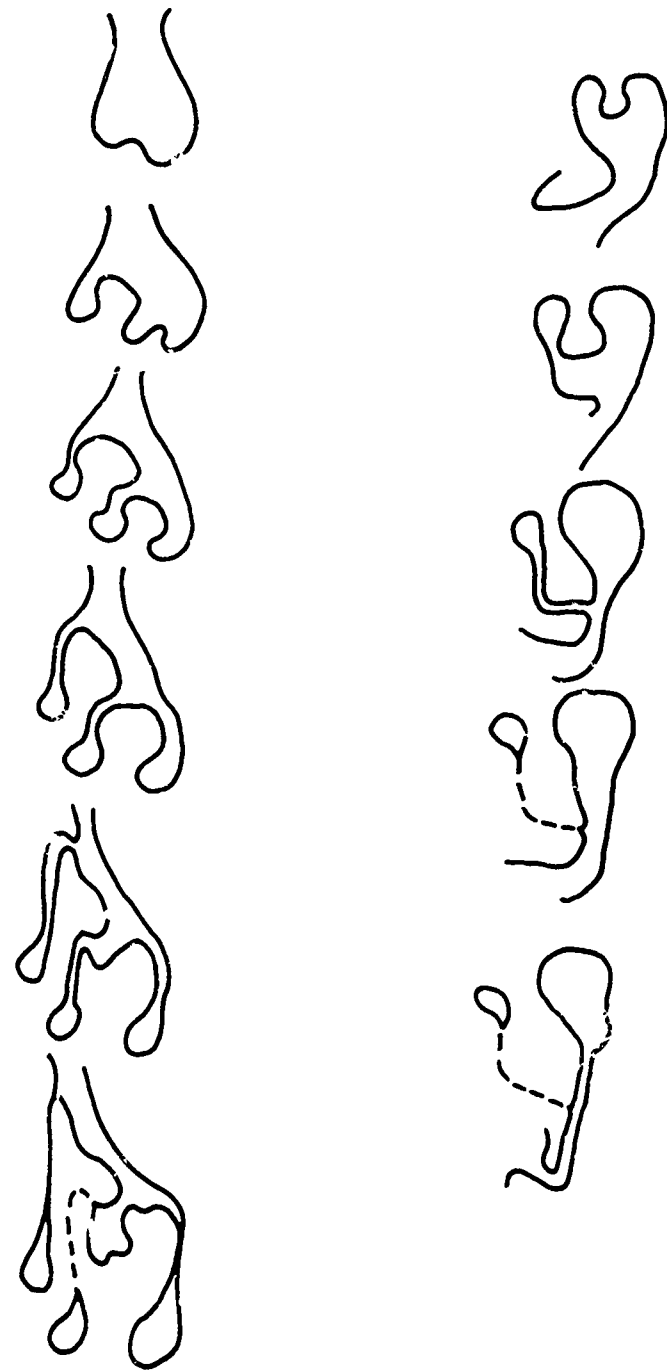


Fig. 28 Pinch-Off and Formation of Isolated Rods (Physical Dynamics, Incorporated)

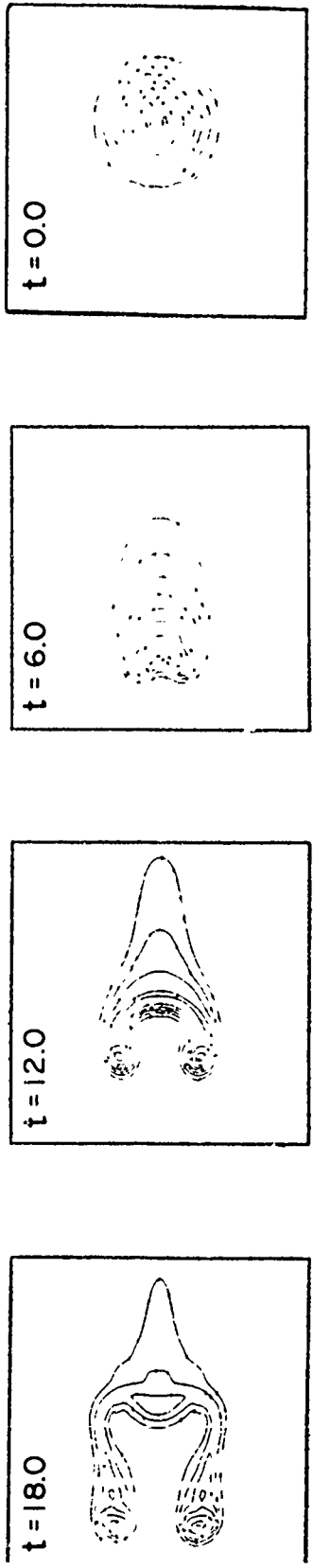
piece of ionization continues to split and elongate until it reaches what is apparently a stable size.

Thomson¹⁸ has carried out a detailed study of the evolution of the tips of sheets as illustrated by the symmetric shapes shown in Fig. 27. It was concluded that the tips grow in size linearly with time. When a characteristic size is reached, the tip bifurcates again. There seems to be a factor of three between the maximum stable size and the smallest new size that is formed. The time scale for a tip to bifurcate also appears to scale with the size of the tip.

Figure 29 shows a computer simulation of this bifurcation process. In order to get the initially cylindrically symmetric rod or ion cloud to bifurcate, an artificial density perturbation had to be introduced at $t = 0$. We note that the scale length of the nonlinear sheets far exceeds the scale associated with the original perturbation. We also see that the peak electron density at late times is at the very tip of the developing sheets. The sheets have begun to pinch off at $t = 18$ due to the artificial diffusion included in the computer routine. Note also that by $t = 18$ the background ionization between the two sheets has also bifurcated.

Figures 30 through 34 show a sequence of views of the Spruce ion cloud taken up the magnetic field line. The magnetic zenith is easily identifiable in these photographs as the point of convergence of the rayed structures. In Figs. 30, 32, and 33 we see evidence of bifurcated sheets. In Figs. 30, 32, and 34 we see structures quite similar to the tracings taken from the Hele-Shaw cell shown in Fig. 28. The similarity in appearance of these phenomena indicates that the Hele-Shaw cell is a useful simulation of the nonlinear sheet development process.

COMPUTER SIMULATION OF BIFURCATION



1. INITIAL PERTURBATION NEEDED
2. MAXIMUM DENSITY IS AT TIP OF SHEET
3. PINCHING IS EVIDENT
4. NOTE THAT INDENTATION BIFURCATES

D1807



Fig. 29 Deformation of Isodensity Contours for an Initially Circular Plasma Cloud with a 5% Initial Perturbation Showing a Simulation of Bifurcation (Bell Telephone Laboratories)



Fig. 30 Spruce From C-6 at R + 22:25 (Technology International Corp.)



Fig. 31 Spruce From C-6 at R + 22:59 (Technology International Corp.)



Fig. 32 Spruce From C-6 at R + 24:05 (Technology International Corp.)



Fig. 33 Spruce From C-6 at R + 26:22 (Technology International Corp.)



Fig. 34 Spruce From C-6 at R + 27:08 (Technology International Corp.)

Some of the scale sizes evident in this series of photographs can be estimated by noting that the separation between the pair of bright stars near the bottom of Fig. 31 corresponds to approximately 5 km at an altitude of 185 km, the height of the middle of the rod along the magnetic field line. In Fig. 32 note the very thin sheet that is attached to the newly formed rod near the magnetic zenith. This sheet appears to be approximately 30 m thick in the original photographs. Other thin sheets can be identified throughout Figs. 31 through 34. We will discuss the lifetime of these fine structures below.

We call the readers attention to a small-, medium-, and large-size rod in this series of Spruce photographs. A small 60 m wide rod can be seen in the original of Fig. 30 on the southernmost edge of the Spruce ion cloud. This rod is not evident in Fig. 31 and appears to have faded away. Note the pair of bifurcating sheets seen in Fig. 30. In Fig. 31 the newly formed sheets have pinched off to form rods. The smallest of these appears to be about 120 m in width. It can still be identified faintly in Fig. 34, indicating a lifetime of at least 4 minutes. Directly below the pair of bifurcating sheets seen in Fig. 30 is a larger rod that has a well-developed sheet attached to it. This rod can still be clearly seen in Fig. 34 and appears to be approximately the largest-sized rod that does not bifurcate.

Now let us see what theoretical investigations have to say about the question of scale size. The linearized stability analysis applied to the backside of a barium ion cloud³ has been extended in several ways, primarily by taking into account the finite size of the ion cloud and the finite ratio of the ion cloud conductivity to the background conductivity.

The stability of a slab with a density profile

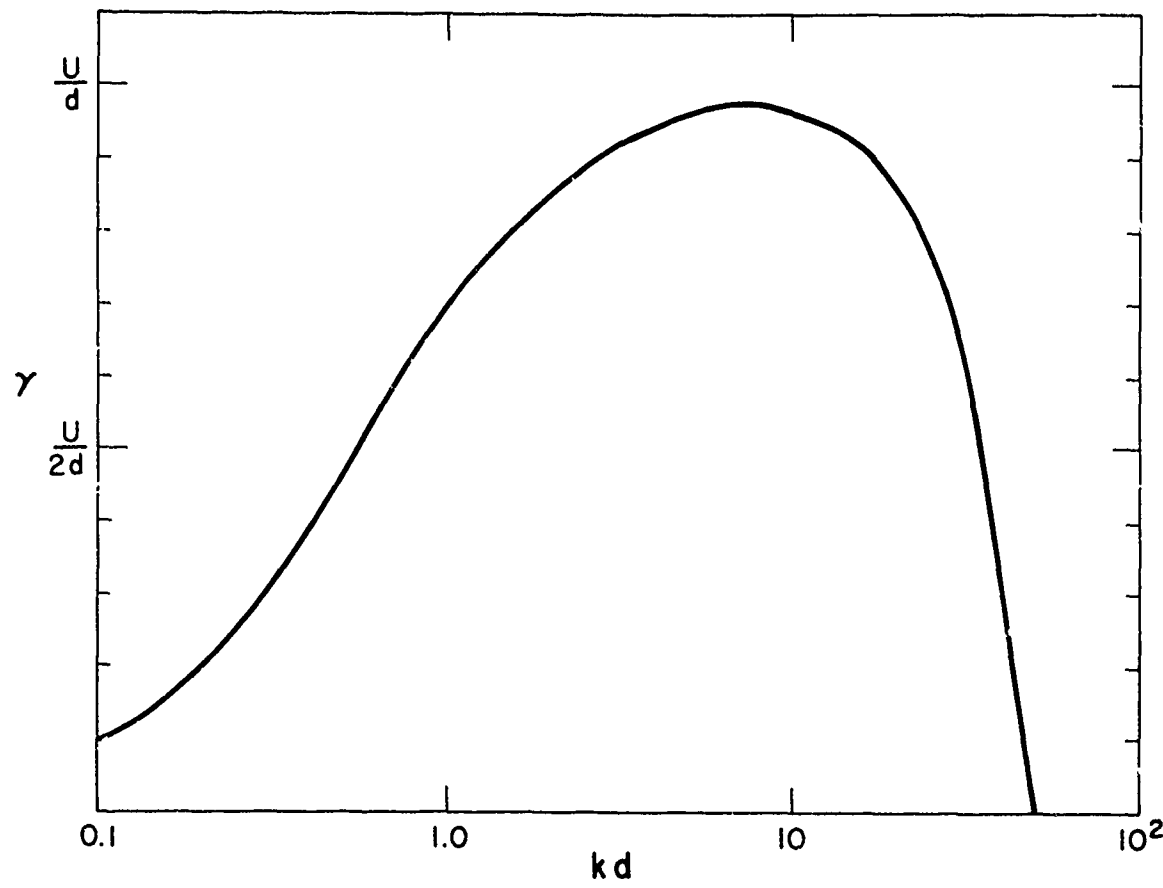
$$N = \begin{cases} N_o & x < 0 \\ N_o e^{x/d} & 0 < x < x_o = d \ln (1 + N_c/N_o) \\ N_o + N_c & x_o < x \end{cases} \quad (35)$$

has been analyzed using the two-dimensional equations including electron-controlled diffusion perpendicular to the magnetic field. In the respective limits the growth rate assumes the form

$$\gamma = \begin{cases} kU \tan k \frac{a}{2} - k^2 D_{\perp}; & kd \ll 1 \\ \frac{U}{a} \left[1 - \frac{1 + \pi^2/a^2}{4(kd)^2} \right] - k^2 D_{\perp}; & kd \gg 1 \end{cases} \quad (36)$$

where $k = 2\pi/\lambda$ is the wavenumber of the perturbation in the y -direction and $a = N_c/N_o$. U represents the relative velocity between the back edge of an ion cloud and the velocity of the neutral atmosphere.

A typical linear-wave spectrum is shown in Fig. 35. There is a wavelength for maximum growth, but it should be pointed out that the wavenumber scale is logarithmic and there is a significant growth rate for a wide range of different scale sizes. It is reasonable to expect a variety of wavelengths attempting to grow initially. It should be emphasized that the value of the wavelength for maximum growth depends sensitively on the parameter $d = |\nabla \ln N|^{-1}$ which so far can only be estimated for large density barium ion clouds that have steepened. When striations have formed, they exhibit very large gradients in density corresponding to small values for d . Hence, the striations themselves should be unstable to very small wavelengths as we shall see below.



$$d = |\nabla \ln N|^{-1} ; \quad U = f \left(\frac{\Sigma_p^c}{\Sigma_p^a} \right) \frac{E_0}{B}$$

$$\chi = \left(\frac{Ud}{4D_L} \right)^{1/2} \gg 1 ; \quad \lambda_{MIN} = \frac{\pi d}{\chi}$$

DIBOI

$$\lambda_{PEAK} = \frac{2\pi d}{\sqrt{\chi}}$$

Fig. 35 Linear Wave Spectrum

Table 2 summarizes a preliminary estimate of some of the scale sizes identified in photographs of the three events Redwood, Spruce, and Nutmeg. The dominant width tabulated represents the overall sheet size when the ionization is fully striated. It is basically estimated by dividing the distance between the two outermost sheets by one less than the number of sheets that can be counted. This distance is compared in the table with the peak wavelength given by the linear wave spectrum in Fig. 35. The appropriate values for U and D_{\perp} were used for each event. We see that the uniform assumption that $d = 500$ m does not give good agreement with the observed dominant wavelength. However, if $d = 500$ m is assumed appropriate for Spruce and d is scaled to the initial transverse width of each of the other two clouds, then the wavelength for peak growth gives excellent agreement with the observed dominant widths. It is not clear why the smaller size sheets that form larger sheets are never smaller than 100 to 150 m in full width. If one applies the two-dimensional linear stability analysis to the tip of a sheet, one calculates that perturbations on a wavelength scale of meters should be unstable. Hence, the fact that a sheet or rod with a transverse width of 500 m does not appear to bifurcate suggests that the two-dimensional model may not be appropriate for these small scale lengths.

Zabusky, Perkins, and Doles⁵ have pointed out that the finite resistivity parallel to the magnetic field in the ambient ionosphere due to electron collisions has a significant effect on the minimum unstable wavelength. The finite resistivity means that magnetic field lines are no longer equipotentials and electrons can cross field lines. Thus they no longer prevent ions from crossing field lines and the minimum scale length becomes controlled by

TABLE 2
COMPARISON OF SCALE SIZE ($\lambda/2 = 2a$)

Scale Size	Event and Altitude	REDWOOD 250 km	SPRUCE 185 km	NUTMEG 150 km
Maximum stable (m)		500	500	?
Minimum developed (m)		150 ?	150	100 ?
Thinnest sheets (m)		<50	<60	<50
Dominant Width				
Observed (m)		300-500	400	250
Theory				
$d = 500$ (m)		170	400	500
$d \propto a$ (m)		340	400	300

ion diffusion in the ambient ionosphere. Although they have not solved a dispersion relation, they did obtain an estimate of the minimum unstable wavelength by using quadratic forms;

$$\lambda_{\min} = 2\pi d \left(\frac{N_c}{N_o} \frac{2T}{eEd} \frac{L^2}{d^2} \frac{1}{\kappa_{eA}} \frac{1}{\kappa_i^2} \right)^{1/4} \sim 0.8 \text{ km.} \quad (37)$$

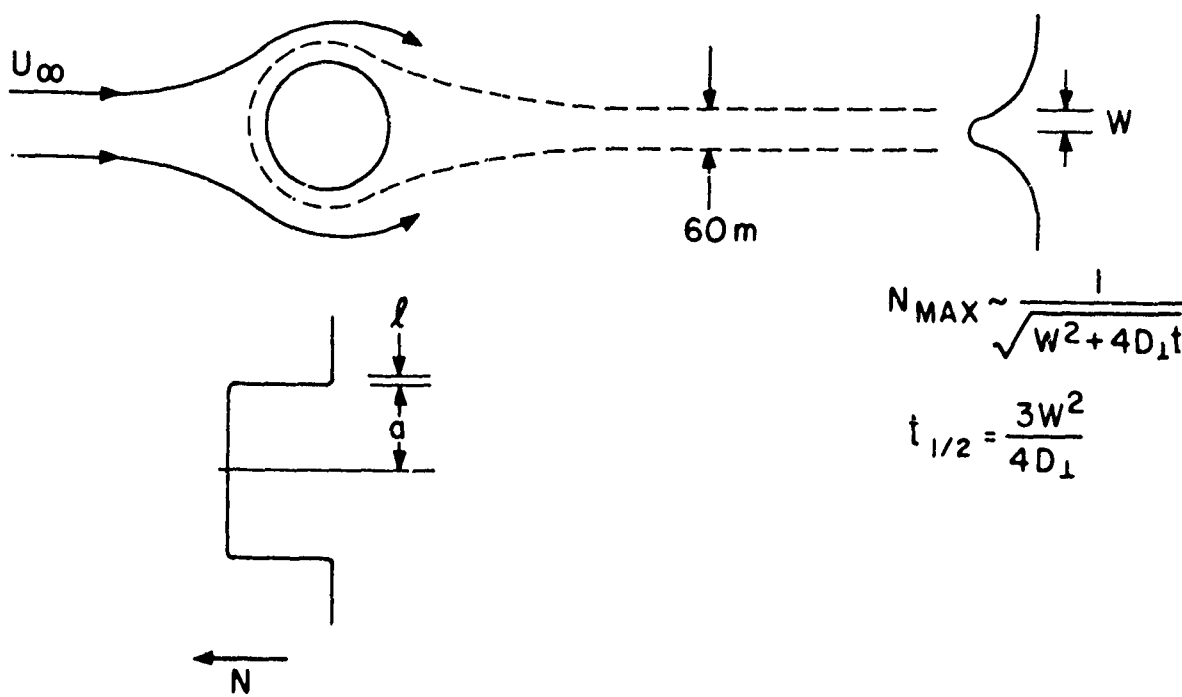
Here N_c/N_o is the ratio of cloud to ambient electron content and L is the length in the ionosphere indicated in Fig. 3. The above estimate is arrived at by taking $d = 1 \text{ km}$, $N_c/N_o = 2$, $T/eEd \approx 0.05$, $L/d \approx 10^2$, $\kappa_{eA} = 1.3 \times 10^4$ and $\kappa_i = 25$. We note that this estimate suggests that striations with a width of order 400 m or less should be stable in agreement with the observations.

It seems apparent that sheets exist that are as thin as can be resolved. Since the barium ion has a gyroradius of approximately 8 m, one might conclude that 16 m is the minimum size sheet that can exist. As a final comment, the density gradient lengths associated with rods can easily be 10 m or below. There is evidence from the short pulse radar that density gradients on this short a scale do exist.

3. Lifetime of Rods and Sheets

Now we turn our attention to a process that we suggest determines the lifetime of rods and sheets. Figure 36 shows a schematic of a rod with the ambient ionospheric flow around it. A barium ion that is transferred from the rod into the background ionosphere will immediately acquire the relative flow velocity labeled U_∞ . Diffusion transverse to the magnetic field is a process for taking ions from the rod and putting them into the region of the background flow. Rods are seen to have very well defined

DISSIPATION OF RODS



$$\text{FLOW TIME } \tau_f = \frac{a}{U_\infty}$$

$$\text{DIFFUSION LENGTH } l = \sqrt{D_1 \frac{a}{U_\infty}}$$

$$\text{LIFETIME } T = \frac{a}{l} \tau_f = \frac{a^{3/2}}{\sqrt{D_1 U_\infty}}$$

D1805

Fig. 36 Schematic of a Dissipation Mechanism for Rods

edges indicating very sharp density gradients. If we assume that their density distribution is flat with sharp sides as indicated schematically, the transverse diffusion across the magnetic field line would broaden the edge into a finite width, ℓ . This width is determined by the value of the perpendicular diffusion coefficient, D_{\perp} , and the value of the characteristic flow time of the ambient ionization around the rod, a/U_{∞} , where a is the half-width of the rod. The lifetime of the rod is then given by the number of flow times it takes to erode the whole rod by removing a layer of thickness ℓ each flow time as indicated by

$$T = \frac{a}{\ell} \frac{a}{U_{\infty}} = \frac{a^{3/2}}{\sqrt{D_{\perp} U_{\infty}}} . \quad (38)$$

The ionization that is carried by the ambient flow ends up in the sheet whose width, w , apparently can be from below 30 m up to 500 m. Due to the uniformity of the ionization in the direction of the flow, the lifetime of the sheet is significantly larger than that of the rod and is controlled by ordinary one-dimensional diffusion transverse to the direction of the sheet -- i.e., $N \sim (w^2 + 4D_{\perp}t)^{-1/2}$ -- which yields

$$t_{1/2} = \frac{3w^2}{D_{\perp}} \quad (39)$$

as an estimate for the time $t_{1/2}$ for the sheet density to decrease by a factor of 2.

Figure 37 shows a preliminary comparison of the lifetime for rods and sheets estimated by Eqs. (38) and (39) with some of the rods and sheets discussed in the Spruce photographs (Figs. 30 through 34). The agreement between the data and the theoretical curves is sufficiently good to encourage pursuing this idea further.

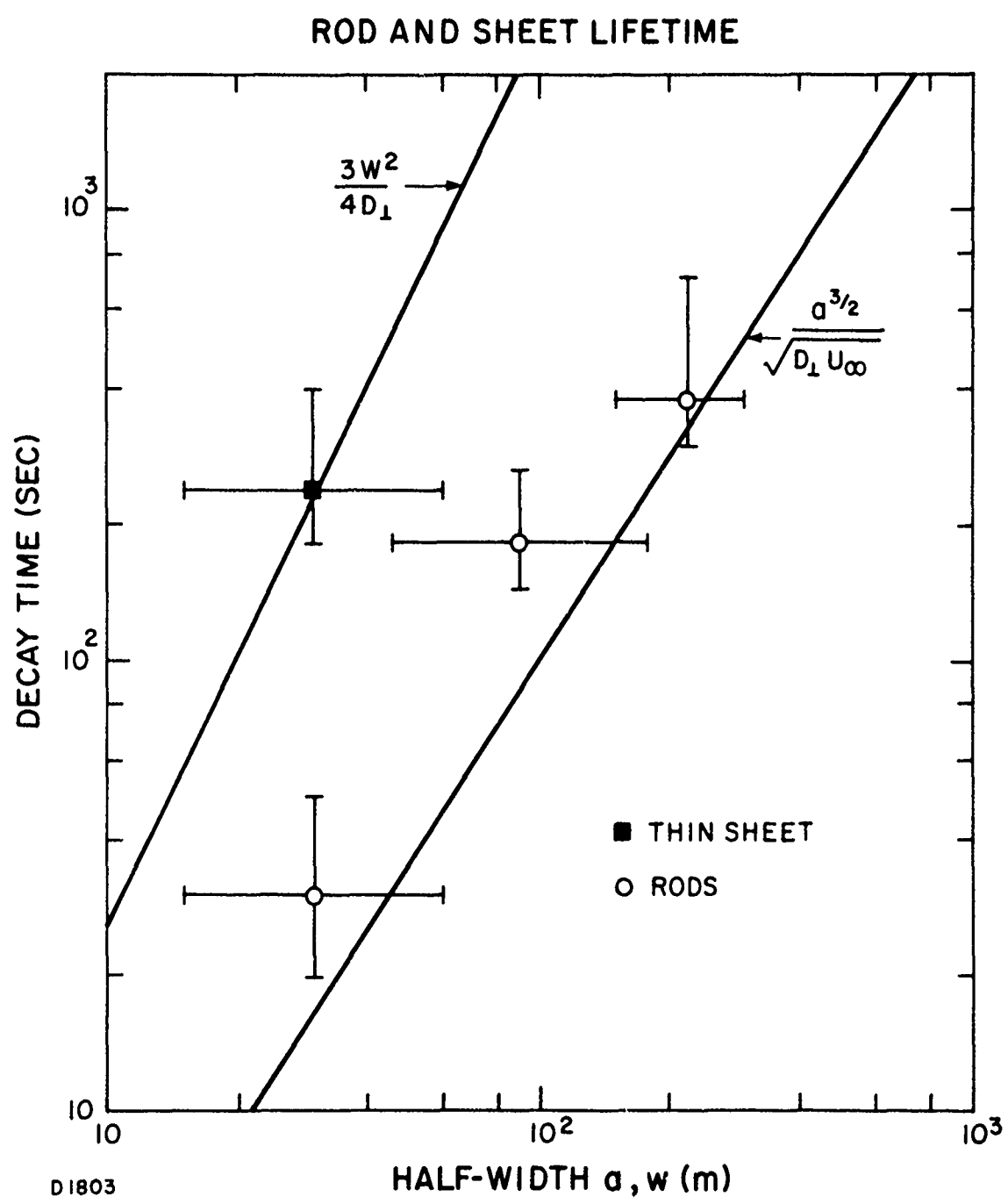


Fig. 37 Rod and Sheet Lifetime

F. SUMMARY

1. Conclusions

A solid theoretical basis has been established for understanding a number of the complex phenomena that occur when barium ion clouds are released into the upper ionosphere. We have indicated that a simple set of coupled nonlinear equations (see (28)-(30) are capable of describing a number of these phenomena. We know what governs the motion of barium ion clouds and their elongation transverse to the magnetic field in the direction of the neutral wind, and we know why they become unstable. This detailed understanding provides a basis for reliable predictions of barium ion cloud motion provided certain ambient parameters, primarily the ambient electric field, \vec{E}_a , the neutral wind velocity, \vec{V}_n , and the ionospheric conductivity are known at the location of the planned release. Analytic work, numerical solutions, and hydrodynamic simulation prove to be useful for understanding the kinds of motion and instabilities described by the nonlinear equations (28) through (30). In particular, analytic work has been successful in correlating the motion of ion clouds, the onset time of striations, the dominant striation wavelength, and the lifetime of rods with data corresponding to a wide range of ambient and cloud parameters.

A combination of empirical scaling of the Secede data base and our theoretical understanding also allows reliable predictions of the onset time of striations for barium ion clouds at midlatitudes and for ionization produced in other circumstances. A point that has not been brought out so far is the fact that now a configuration of ionization may be chosen that will striate quickly and yield high electron densities in the

striations, and permit a more reliable estimate of where the striations will occur (see Chapter 2 of Vol. II of this report).

It is important to recognize that in large high-density ion clouds the transport mechanism perpendicular to the magnetic field is controlled by electron collisions. This fact explains why small-scale structure can be observed for long times and why the ionization persists for hours in the ionosphere. We have also shown that the conjugate ionosphere, more than 30,000 km distant, apparently participates in the dynamics of barium ion clouds.

2. Future Work

There are important areas where additional theoretical work is necessary. The influence of the initial ion-deposition process on the later time behavior of the ion cloud is not well known. Since the neutral cloud is optically thick to the solar metastable exciting radiation, the barium ions are not created uniformly. They are created initially on the sunlit side of the neutral cloud and only later are created on the dark side after the metastable barium ions have been consumed by photoionization and oxidation. It is possible that this process leads to initial constant ion-density contours that are quite distorted from cylindrical symmetry. Once this distortion is known, an evaluation of the effect on the later time behavior of the ion cloud can be made.

The origin of the long delay time before striations occur in barium ion clouds is not completely understood. The theoretical modeling that seems to correlate quite well with the data suggests that the delay results from the competition between the tendency of barium ion clouds to steepen

on their backside and their tendency to striate. Both processes are a reflection of the tendency of the higher density portions of the ion cloud to remain more coupled with the neutral wind. The model giving the onset time shown in Fig. 22 suggests that as long as steepening can occur, the tendency to striate is quite reduced and the ion cloud only begins to develop structure after it has steepened considerably.

There are two other possible explanations for the long delay before striations appear. One possibility is that there are stabilizing effects that are operating at early times due to potential variations parallel to the magnetic field. A realistic model that shows such an effect has not yet been developed. However, mechanisms that can lead to the stabilization of striations at early times ought to be investigated. It would perhaps be logical to assume that the striations are driven unstable when the backside has steepened sufficiently so that linearized growth rate increases.

Another possibility is that the long delay time before striations occur is just a reflection of the extremely small initial amplitudes of perturbations which need to have many e-foldings before they can be seen. Indeed, Zabusky, Perkins, and Doles¹² are lead to this conclusion as a result of the numerical computations shown in Fig. 14. Their smooth cloud did not striate and in order to obtain the bifurcation shown in Fig. 29, they had to introduce an initial perturbation in the electron concentration. Two arguments against this as an explanation can be given. The first is that a linearized growth rate appears to be so large that the delay time corresponds to tens of striation growth times. It is unlikely that initial perturbations would need that many e-folding times to become apparent. A second argument derives from the observation that once striations begin to form, they

form rapidly. Their rate of formation is consistent with a linearized growth rate but not with the long delay before they appear.

There is a question as to what does determine the scale size of striations. The linearized analysis of the two-dimensional slab-like model presented earlier seems to give scale sizes in rough agreement with the overall size of the sheets that are formed. However, the same linear analysis predicts that the tips of the sheet should be subjected to the same instability, and should continue to break up into smaller striations down to scale lengths of the order of tens of meters. Thus the fact that a 300-500 meter diameter sheet or rod appears to be stable and does not bifurcate into smaller sheets is not explained by the linearized, two-dimensional analysis. Perkins, Zabusky and Doles⁵ have indicated that the large conductivity of electrons parallel to the magnetic field can allow diffusion by ions in the ambient ionosphere to control the minimum scale size of striations. The resulting estimate for the maximum stable scale size appears to be in agreement with the minimum unstable scale size. The range of applicability of each of these two linearized analyses ought to be investigated further. An indication that the striation scale size may be insensitive to the wavelength of a small initial perturbation is provided by the numerical computation shown in Fig. 29.

The possibility exists that the scale size of the striations is determined by the fact that there is a maximum size that does not feel the influence of the conjugate ionosphere. In support of this possibility is the observation by Chesnut¹⁹ that the motion of the striations after they have been formed in Event Spruce is not colinear with the motion of the neutral wind and the main barium ion cloud. Both the theory describing the motion of barium

ion clouds and the modeling of the onset time for striations indicate that the conjugate ionosphere participates in the dynamics of barium ion clouds. Estimates were presented that show that the typical voltage drop across a barium ion cloud is of order 12 volts whereas the finite resistivity of the local ionosphere parallel to the magnetic field would cause a much smaller voltage drop of order 1.4 volts. However, the voltage drop across a cloud of ionization is directly proportional to its transverse scale size. Hence once striations have been formed, they should be decoupled from the conjugate ionosphere.

Each of the above theoretical questions require further study. In addition, an investigation into the interaction of different ionospheric layers is needed. No work considering different winds at different altitudes has yet been attempted. Analytic work is also needed on the nonlinear effects exhibited by barium ion clouds, for example, the bifurcation and the pinching characteristics of sheets need to be more thoroughly studied as well as the distortions of barium ion clouds. Finally, there are a number of unresolved questions regarding the effect of ion cloud density distributions on HF radar scattering. A resolution of these questions would provide an additional diagnostic of striation characteristics.

REFERENCES

1. C. W. Clench and B. Kivel, "Data Report on Project Birdseed I," Research Note 866, Avco Everett Research Laboratory, Everett, Mass. (November 1970).
2. J. W. Dungey, Cosmic Electrodynamics, p. 161, (Cambridge University Press, 1958).
3. L. M. Linson and J. B. Workman, "Formation of Striations in Ionospheric Plasma Clouds," J. Geophys. Res., Vol. 75, p. 3211 (1970).
4. J. N. Shiao and A. Simon, "Generalized Slab Model and Finite Larmor Radius Effects", RADC TR-72-147, Univ. of Rochester (April 1972).
5. N. J. Zabusky, F. W. Perkins, and J. H. Doles, III, "Deformation and Striation of Plasma Clouds in the Ionosphere, I", in Proceedings of the 1971 Technical Planning Session, RADC TR-71-200, Vol. III, Theory, p. 127, Stanford Research Institute, Menlo Park, Calif. (September 1971) (to be published in J. Geophys. Res., 1972).
6. J. R. Bannister and H. L. Davis, "Descent of Particles and Molecules Through the Upper Atmosphere," Phys. Fluids, 5, 136 (1962).
7. B. Rao Pendyala, "A Comparison Between Thomson Scatter Radar Observations and a Diffusion Model," in Proceedings of the Secede II Final Data Review Meeting, RADC TR-72-153, Vol. II, pp. 129-141, Stanford Research Institute, Menlo Park, Calif. (May 1972).
8. J. H. Mitchell and K. E. W. Ridler, "The Speed of Positive Ions in Nitrogen," Proc. Roy. Soc., (London) A 146, 911 (1934).
9. A. Simon, "Growth and Stability of Artificial Ion Clouds in the Ionosphere," J. Geophys. Res., 75, 6287 (1970).
10. L. M. Linson, "Nonlinear Dynamics of Barium-Ion Clouds," in Analysis of Barium Clouds, Semi-Annual Technical Report, RADC TR-71-253, Vol. I, p. 39, Avco Everett Research Laboratory, Everett, Mass. (June 1971) -- also in Proceedings of the 1971 Technical Planning Session, RADC TR-71-200, Vol. III, Theory, p. 23, Stanford Research Institute, Menlo Park, Calif. (September 1971).

11. L. M. Linson, "Motion of Barium-Ion Clouds," in Analysis of Barium Clouds, Semi-Annual Technical Report, RADC TR-72-103, Vol. I, p. 39, Avco Everett Research Laboratory, Everett, Mass. (January 1972)-- also in Proceedings of the 1971 Technical Planning Session, RADC TR-71-200, Vol. III, Theory, p. 1, Stanford Research Institute, Menlo Park, Calif. (September 1971).
12. N. J. Zabusky, F. W. Perkins, and J. H. Doles, III, "Deformation and Striation of Plasma Clouds in the Ionosphere, II. Numerical Simulation of a Nonlinear Two-Dimensional Model," in Proceedings of the 1971 Technical Planning Session, RADC TR-71-200, Vol. III, Theory, p. 127, Stanford Research Institute, Menlo Park, Calif. (September 1971) (to be published in J. Geophy. Res., 1972).
13. J. A. Thomson, "An Equivalent Hydrodynamic Model," in 1970 Summer Study Proceedings, RADC TR-70-216, Vol. III, Theoretical Considerations, p. 117, Stanford Research Institute, Menlo Park, Calif. (September 1970).
14. S. B. Mende, "Generation of Secondary Irregularities by Motion of Ion Clouds," in Proceedings of the 1971 Technical Planning Session, RADC TR-71-200, Vol. III, Theory, p. 63, Stanford Research Institute, Menlo Park, Calif. (September 1971).
15. G. Haerendel, R. Lust, and E. Rieger, "Motion of Artificial Ion Clouds in the Upper Atmosphere," Planet. Space Sci., Vol. 15, 1 (1967).
16. N. W. Rosenberg, "Observations of Striation Formation in a Barium Ion Cloud," J. Geophys. Res., 76, 6856 (1971).
17. J. A. Thomson, "A Hydrodynamic Analog of Ionospheric Plasma Releases (U)," in Proceedings of the 1971 Technical Planning Session, RADC-TR-71-200 Supplement, p. 1, Stanford Research Institute, Menlo Park, Calif. (September 1971), SECRET.
18. J. A. Thomson, "Analysis of Structures in a Hele-Shaw Cell (U)," in Proceedings of the 1971 Technical Planning Session, RADC-TR-71-200 Supplement, p. 31, Stanford Research Institute, Menlo Park, Calif. (September 1971), SECRET.
19. W. G. Chesnut, "Discussion of Barium-Cloud Morphology as Revealed by Measurements from Photographs of Events Spruce and Redwood," in Preliminary Results of Test Series Secede II, RADC TR-71-72, p. 187, Stanford Research Institute, Menlo Park, Calif. (April 1971).
20. L. M. Linson and M. J. Baron, "Ion Cloud Parallel Diffusion -- Comparison of RF, Optical and Theoretical Results (U)," in Proceedings of the 1971 Technical Planning Session, RADC TR-71-200, Vol. I, p. 161, Stanford Research Institute, Menlo Park, Calif. (September 1971), SECRET.

UNCLASSIFIED

Security Classification

DOCUMENT CONTROL DATA - R & D

(Security classification of title, body of abstract and indexing annotation - not be entered when the overall report is classified)

1. ORIGINATING ACTIVITY (Corporate author) AVCO EVERETT RESEARCH LABORATORY 2385 REVERE BEACH PARKWAY EVERETT, MASSACHUSETTS	2a. REPORT SECURITY CLASSIFICATION UNCLASSIFIED
	2b. GROUP

3. REPORT TITLE

ANALYSIS OF BARIUM CLOUDS

4. DESCRIPTIVE NOTES (Type of report and inclusive dates)
Final Technical Report

5. AUTHOR(S) (First name, middle initial, last name)

Dr. B. Kivel, Dr. L. M. Linson and Dr. G. M. Weyl

6. REPORT DATE October 1972	7a. TOTAL NO OF PAGES 199	7b. NO OF REFS 47
--------------------------------	------------------------------	----------------------

8a. CONTRACT OR GRANT NO F30602-71-C-0067	8b. ORIGINATOR'S REPORT NUMBER(S)
b. PROJECT NO 10570203	
c. Program Code No.: 1E20	9b. OTHER REPORT NO(S) (Any other numbers that may be assigned this report)
d. ARPA Order No.: 1057	RADC-TR-72-336, Volume I

10. DISTRIBUTION STATEMENT Distribution limited to U. S. Government Agencies only, (Test and Evaluation); January 1973. Other requests for this document must be referred to RADC (OCSE), GAFB, N. Y. 13441
--

11. SUPPLEMENTARY NOTES Monitored by : Leonard Strauss, RADC/OCSE, Griffiss AFB. New York 13441 Tel. 315-330-3451	12. SPONSORING MILITARY ACTIVITY Defense Advanced Research Projects Agency, 1400 Wilson Boulevard Arlington, Virginia 22209
--	--

13. ABSTRACT Several aspects of the analysis of barium ion clouds are presented including ion cloud modeling, comparison of radar and optical data, and correlation of data with theory. A quantitative model has been developed from which various properties of barium ion clouds, primarily their size, time history of the peak electron concentration, and height-integrated conductivity can be estimated. These estimates are in excellent agreement with the observations of Secede ion clouds. The modeling of the radiation transport in the ion cloud has been confirmed by a Monte Carlo calculation. The optical analysis of Spruce at R + 14 min has been corrected for effects of cloud geometry and the results for ion density are found self-consistent and in agreement with radar measurements. A summary review is given of the values and limitations of photographic data. The current status of theoretical understanding of the dynamics of barium ion clouds is reviewed. Particular attention is given to their motion, deformation, and the properties of striations including onset time, scale size, and dissipation.
--

UNCLASSIFIED

Security Classification

KEY WORDS	LINK A		LINK B		LINK C	
	ROLE	WT	ROLE	WT	ROLE	WT
1. Barium Releases 2. SECEDE 3. Ion Cloud Dynamics 4. Ion Cloud Motion 5. Radiation Transport 6. Optical Radar Correlation 7. Photographic Data 8. Striations						

UNCLASSIFIED

Security Classification